

**Experiments for
p-process nucleosynthesis
with special focus on
the most abundant *p* nucleus ^{92}Mo**

Habilitationsschrift

angenommen vom Fachbereich Physik
der Johann Wolfgang Goethe-Universität
in Frankfurt am Main

von

Kerstin Sonnabend

aus Bensheim

Frankfurt am Main 2014

Dedicated to
my parents,
Doris and Karlheinz,
and
my family,
Jürgen, Lena, and Yasmin
for
their love
and
their patience

Summary

This thesis describes experimental investigations and astrophysical network calculations relevant for the nucleosynthesis of the p nuclei. These 35 proton-rich isotopes cannot be produced by neutron-capture reactions which is the general production mechanism for elements heavier than iron in the r and s processes. Therefore, other mechanisms like photo-disintegration reactions on heavy seed nuclei (γ process) or proton-capture reactions are taken into account.

The modelling of these processes relies on a huge amount of reactions which mostly occur for unstable isotopes. This demands, in combination with the contribution of excited states to the stellar rate, the prediction of the rates by a suited theoretical approach: the Hauser-Feshbach statistical model. To improve the reliability of the predictions, systematic experimental investigations are performed within this work for the nuclear input to the calculations. The study of charged-particle optical model potentials using the activation approach for the investigation of (α, n) and (p, n) reactions is described as well as the investigation of (γ, n) reactions in a broad mass range of $140 \leq A \leq 210$.

However, there are also key reactions which are of special interest for the nucleosynthesis of individual p nuclei. An impressive example is the puzzle about the production of the most abundant p nucleus ^{92}Mo . Within this work, the results of an experiment using high-resolution in-beam γ -spectroscopy for the study of the $^{90}\text{Zr}(p, \gamma)$ reaction are summarized. In addition, the efforts to investigate the $^{91}\text{Nb}(p, \gamma)$ reaction in standard kinematics by the production of target of the unstable isotope ^{91}Nb to be used with the high-intensity proton-beam provided by the accelerator of FRANZ, Frankfurt, are discussed.

Finally, the influence of experimental results in astrophysical network calculations is discussed using post-processing nucleosynthesis methods for the γ process in type II supernovae.

Zusammenfassung

Diese Arbeit beschreibt experimentelle Untersuchungen und astrophysikalische Netzwerkrechnungen, die dem Verständnis der Nukleosynthese der p -Kerne dienen. Diese 35 protonenreichen Isotope können nicht mittels Neutroneneinfangreaktionen produziert werden, die der generelle Mechanismus zur Erzeugung von Elementen schwerer als Eisen sind. Daher werden andere Mechanismen vorgeschlagen wie die Photodesintegration einer Verteilung schwerer Saatkerne (γ -Prozess) oder Protoneneinfangreaktionen.

Die Modellierung dieser Prozesse basiert auf der Kenntnis einer großen Anzahl von Reaktionen, die meistens an instabilen Kernen auftreten. Um außerdem die Beiträge angeregter Kernzustände zur stellaren Reaktionsrate zu bestimmen, ist deren Vorhersage mit einem geeigneten theoretischen Ansatz notwendig: dem Hauser-Feshbach Statistischen Modell. Um die Verlässlichkeit der Vorhersagen zu verbessern, sind systematische experimentelle Untersuchungen in dieser Arbeit durchgeführt worden. Optische Kernpotentiale für geladene Teilchen wurden durch Experimente mit der Aktivierungsmethode zu (α,n)- und (p,n)-Reaktionen bestimmt und in einem breiten Massenbereich von $140 \leq A \leq 210$ wurden (γ,n)-Reaktionen untersucht.

Allerdings gibt es auch Schlüsselreaktionen, die von besonderem Interesse für die Nukleosynthese einzelner p -Kerne sind. Ein beeindruckender Fall ist das Rätsel um die Produktion des häufigsten p -Kerns ^{92}Mo . In dieser Arbeit werden die Resultate eines Experiments mit hochauflösender γ -Spektroskopie zur Reaktion $^{90}\text{Zr}(p,\gamma)$ zusammengefasst. Außerdem werden die aufwändigen Schritte beschrieben, die notwendig sind, um die Reaktion $^{91}\text{Nb}(p,\gamma)$ in direkter Kinematik zu untersuchen: die Produktion eines Targets aus dem instabilen Isotop ^{91}Nb und sein Einsatz an der Hochstrom-Protonenquelle von FRANZ, Frankfurt.

Abschließend wird der Einfluss experimenteller Resultate in astrophysikalischen Netzwerkrechnungen diskutiert. Hierzu wurde der γ -Prozess in einer Typ II Supernova mit Methoden der „post-processing nucleosynthesis“ untersucht.

Contents

1	Introduction	1
2	Astrophysical basics	3
3	Nuclear physics basics	11
3.1	Calculation of reaction rates	15
4	Experimental methods	21
4.1	Activation approach	21
4.2	In-beam technique	23
4.3	Inverse kinematics	26
5	Experiments and analysis	29
5.1	Charged-particle induced reactions	29
5.1.1	Studies to improve optical potentials	31
5.1.2	Proton-capture reactions on light nuclei	41
5.2	Photon-induced reactions	57
5.2.1	Systematic studies with real photons	57
5.2.2	(γ, n) reactions with virtual photons	65
6	Consequences for p-process nucleosynthesis	75
6.1	General remarks	75
6.2	The production of ^{92}Mo	78
7	Summary and outlook	83
8	Zusammenfassung	87
	Bibliography	93

List of Figures

2.1	Solar abundance distribution	4
2.2	Shielding of p nuclei from r - and s -process paths	5
2.3	Isobaric abundances for p -, r -, and s -process nucleosynthesis	6
2.4	Reaction network of the γ process	8
2.5	Reaction network of the rp process	9
2.6	Overproduction factors of p nuclei in type II supernova	10
3.1	Maxwell-Boltzmann distribution for particles	12
3.2	Gamow window of charged-particle induced reactions	13
3.3	Planck distribution for photons	14
3.4	Gamow-like window of photon-induced reactions	15
3.5	Schematic view of compound-nucleus reaction	16
4.1	Influence of half-life on activity	22
5.1	Overview of experimentally investigated (p,γ) and (α,γ) reactions	30
5.2	Sensitivities of the cross section of the $^{168}\text{Yb}(\alpha,\gamma)$ reaction	32
5.3	Number of reaction products as function of time	34
5.4	Sensitivities of the cross sections of the $^{165}\text{Ho}(\alpha,x)$ and $^{166}\text{Er}(\alpha,x)$ reactions	35
5.5	Spectra after activation of holmium and erbium targets	37
5.6	Experimental S factors of $^{165}\text{Ho}(\alpha,n)$ and $^{166}\text{Er}(\alpha,n)$ compared to theory	39
5.7	Experimental S factors of $^{169}\text{Tm}(p,n)$ and $^{175}\text{Lu}(p,n)$ compared to theory	41
5.8	Radiative proton-capture reactions producing light p nuclei	42
5.9	HORUS target chamber for nuclear astrophysics experiments	43
5.10	Scheme of prompt γ transitions of the $^{90}\text{Zr}(p,\gamma)$ reaction	44
5.11	Spectrum of prompt γ transitions of the $^{90}\text{Zr}(p,\gamma)$ reaction	45
5.12	Efficiency-corrected events for measurements with HORUS	46
5.13	Angular distribution of cross section for one γ transition	47
5.14	Total cross section of the reaction $^{90}\text{Zr}(p,\gamma)$	48
5.15	Partial cross section of the reaction $^{90}\text{Zr}(p,\gamma)$	49
5.16	Production of target sample of ^{91}Nb	49
5.17	Spectra after activation of natMo with protons	51
5.18	Schematic layout of the FRANZ facility	52
5.19	Simulation of beam transport in HEBT section of FRANZ	53
5.20	Exemplary simulation of high-pressure water-flow cooling	54
5.21	Half-section of 4π BaF ₂ calorimeter with cone-shaped end of beam-line	56
5.22	Half-section of target chamber for 4π BaF ₂ calorimeter	56
5.23	Approximation of a Planck distribution by bremsstrahlung spectra.	58
5.24	Spectra after irradiation of $^{\text{nat}}\text{Yb}$, $^{\text{nat}}\text{Hg}$, and $^{\text{nat}}\text{Pb}$ with photons	60
5.25	Comparison of measured to predicted rates of (γ,n) reactions	61
5.26	Spectral composition of photon beams from different sources	62

List of Figures

5.27	Schematic view of a Coulomb Dissociation reaction	65
5.28	Virtual photon spectra for different multipolarities	66
5.29	Overview accelerator facility at GSI, Darmstadt, Germany	68
5.30	ALADiN-LAND experimental setup at GSI	69
5.31	Fundamental steps of analyzing CD at ALADiN-LAND setup	71
5.32	CD cross section based on data by Beil <i>et al.</i>	72
6.1	Production and destruction fluxes in type II supernova	79
6.2	Normalized time-integrated fluxes for different Hashimoto trajectories . .	81

List of Tables

2.1	Isobaric and isotopic abundances of the p nuclei	7
3.1	Standard nuclear inputs of Hauser-Feshbach codes	17
5.1	Characteristics of holmium and erbium targets	36
5.2	Cross sections of the reactions $^{166}\text{Er}(\alpha,n)$ and $^{165}\text{Ho}(\alpha,n)$	38
5.3	Characteristics of thulium and lutetium targets	40
5.4	Cross sections of the reactions $^{169}\text{Tm}(p,n)$ and $^{175}\text{Lu}(p,n)$	40
5.5	Characteristics of HEBT magnets at FRANZ	52
5.6	Experiments performed within systematic study of (γ,n) reactions at DHIPS	63
5.7	Experiments performed within systematic study of (γ,n) reactions (ctd.)	64
6.1	Most important reaction rates in the γ process	77

1

Introduction

Astronomical observations always fascinated mankind and found applications in daily life. The first ancient highly developed cultures in Mesopotamia and Egypt used the changes in the heavens to construct a calendar and predict the occurrence of periodic events such as, *e.g.*, the flooding of the Nile river, respectively. The Greeks already knew about the sphericity of earth, sun, and moon and developed first ideas to measure the distances between the three of them and to estimate their masses.

The great achievements of the Greek scientists found a lasting highlight in the Ptolemaic model which served as an explanation for astronomical observations for centuries. Astronomy, as based on these classical ideas, was taught as part of the quadrivium of the seven liberal arts which were rediscovered in Central Europe during the reign of Charlemagne (768 to 814) and were installed as educational standard at medieval European universities (*e.g.*, Bologna 1088, Paris around 1160, Oxford 1167). This geocentric model relied on a complicated application of epicycles to maintain the earth as orbital center of all celestial bodies.

As the Ptolemaic model supported the idea of mankind being the center of the Creation the heliocentric model was not established before the end of the fifteenth century when Nicolaus Copernicus (1473 to 1543) published his ideas in the book *De revolutionibus orbium coelestium*. Johannes Kepler (1571 to 1630) and Sir Isaac Newton (1642 to 1726/7) refined the model by postulating elliptical orbits instead of spherical ones and by applying the physical laws observed on earth to the motions of the celestial bodies, respectively.

The last century brought the combination of astronomy, astrophysics, and nuclear physics in the newly developed research field of nuclear astrophysics. The fusion of hydrogen to helium was recognized as the energy source for the long-lasting first evolution stage of stars. Nuclear reactions provided the opportunity to synthesize all known elements starting from protons and neutrons. In 1957, the quartet of E.M. Burbidge, G.R. Burbidge, W.A. Fowler, and F. Hoyle [1] as well as A.G.W. Cameron [2] independently published their ideas on the nucleosynthesis of the elements and founded the second pillar of nuclear astrophysics besides the explanation of stellar evolution.

In [1], eight processes are proposed to synthesize all known stable and long-lived unstable isotopes: hydrogen burning, helium burning, capture of α particles (α process), nuclear reactions in statistical equilibrium (e process), neutron-capture reactions at low and

high neutron densities (s and r processes), proton-capture reactions (p process) and the production of deuterium, lithium, beryllium, and boron (x process).

Not all proposed processes survived the last nearly 60 years of research without significant corrections. Today, the production of deuterium and lithium is mostly explained by primordial nucleosynthesis right after the Big Bang while the synthesis of beryllium and boron is thought to be based on the spallation of heavier elements. In contrast, the ideas developed for the synthesis of elements heavier than iron in the s and r processes are still the base of today's existing models. An interesting case is the p process being responsible for the production of the proton-rich isotopes which are shielded from the reaction fluxes of the s and r processes. The initial idea of proton-capture reactions still occurs in different processes, *e.g.*, the rp and νp processes but the bulk of the so-called p nuclei is produced by photo-disintegration reactions in the γ process.

This habilitation treatise deals with the different experimental approaches to provide the nuclear physics input for the simulation of the nucleosynthesis of p nuclei in various scenarios. Chapter 2 will introduce the astrophysical background and discuss the different sites and scenarios where p nuclei are thought to be produced. The nuclear physics basics including the calculation of reaction rates are described in Chap. 3 while the different experimental methods as applied within this treatise are summarized in Chap. 4. In Chap. 5, experiments on charged-particle induced reactions and on photon-induced reactions including their analysis are explained. The possible consequences for the nucleosynthesis of p nuclei derived from these experimental results are discussed in Chap. 6 before the treatise finishes with a summary and an outlook in Chap. 7.

2

Astrophysical basics

All elements around us are built in stars from the remainders of primordial nucleosynthesis – hydrogen and helium (see, *e.g.*, [3] and references therein). In nuclear fusion processes, the stars not only find a long-lasting source of energy to stabilize against gravitational pressure but also produce isotopes with increasing mass numbers and, thus, heavier elements (see, *e.g.*, [4] and references therein). Due to the maximum of the binding energy per nucleon reached in the iron-nickel region, the process stops here forcing heavy stars to finish their evolution in the bright event of a core-collapse supernova [5].

It is during such an event when elements beyond the iron-nickel region are created by a combination of radiative neutron-capture reactions and β decays. Since the neutron densities and temperatures are incredibly high, very exotic neutron-rich isotopes are produced in this rapid neutron-capture process (*r* process) [6]. After several milliseconds, the explosive event passes off and the unstable isotopes reach the valley of stability by a series of successive β decays. About half of the amount of heavy elements beyond the iron-nickel region are produced in that way while the other half stems from a more quiet scenario settled during late stages of stellar evolution.

The conditions during the slow neutron capture process (*s* process) force the reaction path to remain near the valley of stability [7]. The neutron-capture rates are low, therefore, β decay takes place when an unstable isotope is reached. Due to the overall long times of neutron exposure, all elements up to lead and bismuth are produced eventually. Two distinct scenarios are known today where these conditions are realized: Elements between iron and the Sr-Y region are synthesized in the *weak s*-process during carbon-shell and helium-core burning, respectively [8]. The *main s*-process occurs in thermally-pulsing asymptotic giant branch (TP-AGB) stars and produces elements from the Sr-Y region up to lead and bismuth [9].

The signatures of these different processes are clearly depicted in the solar abundance distribution if plotted as a function of mass number A (compare Fig. 2.1). By far, the dominating elements are hydrogen and helium followed by carbon, oxygen, and other so-called α elements produced in stellar burning phases. The peak in the iron-nickel region stems from nuclear statistical equilibrium – realized in thermonuclear supernovae [11] – which is only survived by the most tightly bound isotopes. Beyond this iron-peak region, the abundances decrease dramatically since neutron-capture processes are

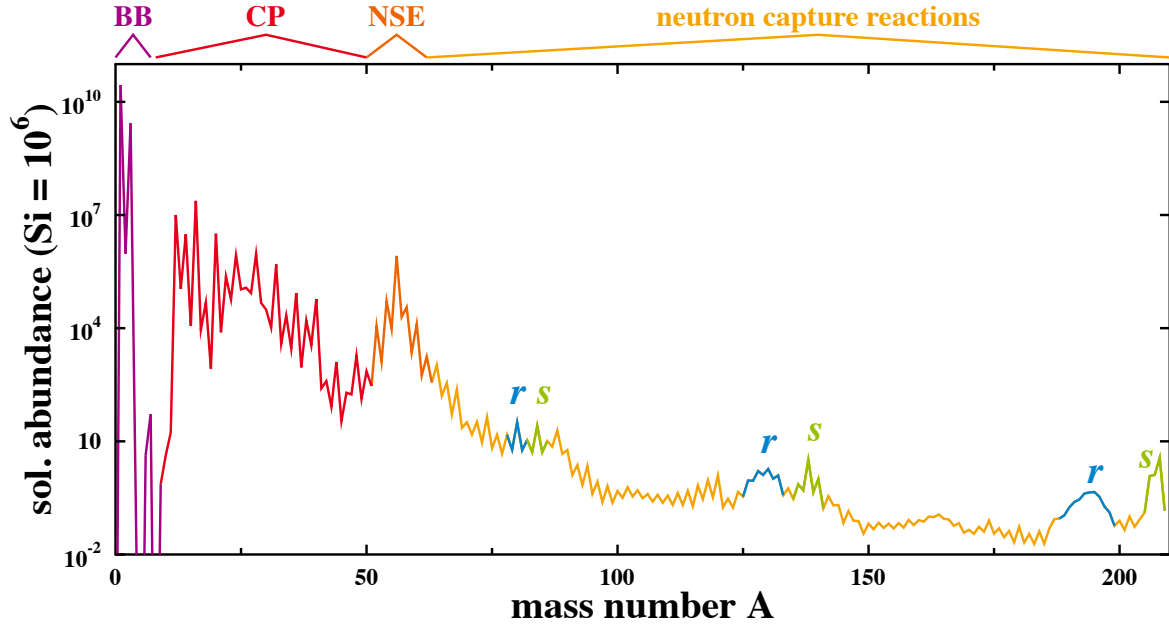


Figure 2.1:

The solar abundance distribution. The abundances in the solar systems basically derived from spectroscopy of the sun and the analysis of meteorites are plotted as a function of mass number A . The lightest elements, hydrogen and helium, are produced in primordial or Big Bang nucleosynthesis (BB). Charged-particle fusion reactions (CP) and reactions in nuclear statistical equilibrium (NSE) are responsible for the elements up to the iron-nickel region. Beyond that region, neutron-induced reactions and β decays synthesize all other known elements in the r and s process. For details, see text. Data taken from [10].

needed to produce these elements. The fingerprints of the r and s processes are the depicted double-peak structures being related to closed neutron shells reached for exotic neutron-rich isotopes and at the valley of stability, respectively.

Some major questions like, *e.g.*, the astrophysical site(s) of the r process, are yet to be answered. In addition, a closer inspection in terms of isotopic abundance ratios reveals some puzzles. Especially, there are about 35 proton-rich isotopes beyond iron which are passed by or shielded from the reaction flows of the r and s processes [12] and are usually referred to as p nuclei after the name of their production process in [1].

Characteristics of the p nuclei The p nuclei are found on the proton-rich side of the valley of stability for elements beyond iron with the lightest one being the isotope ^{74}Se and the heaviest one being the isotope ^{196}Hg . They are passed by the s process since their mass number A is smaller than the one of the most neutron-rich stable isotope of lighter elements and they are shielded from the β -decay chains after the r process by a

stable isobar with smaller proton number Z (compare Fig. 2.2).

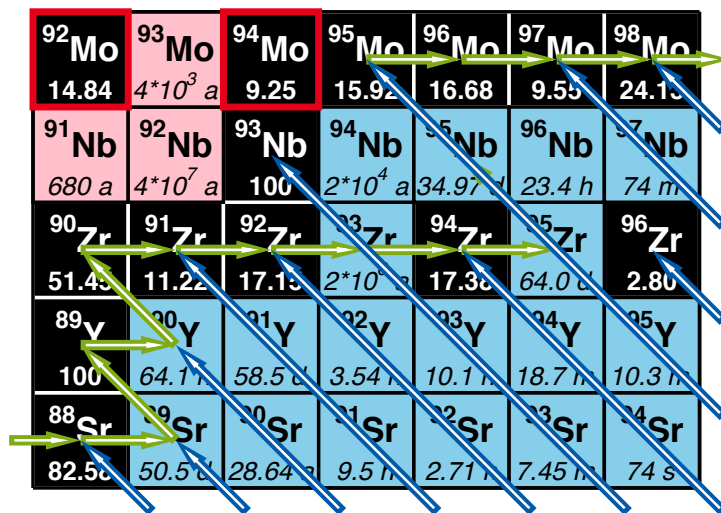


Figure 2.2:

Shielding of p nuclei from r - and s -process reaction paths. The reaction path of the s process (without branchings, green arrows) and the β -decay chains subsequent to r -process conditions (blue arrows) are shown in the mass region of strontium to molybdenum. The p nuclei ⁹²Mo and ⁹⁴Mo (red boxes) are shielded from the reaction paths.

Their isobaric abundance is usually smaller compared to isotopes originating from r - and/or s -process nucleosynthesis as illustrated in Fig. 2.3. *E.g.*, the heavier p nuclei are an order of magnitude less abundant compared to isotopes produced in the s -process. This low isobaric abundance is also reflected in their small isotopic abundance as listed in Tab. 2.1. Although also amounts in the percent range occur for, *e.g.*, ^{92,94}Mo and ^{96,98}Ru, their isotopic abundance is usually in the per-mill range or even below.

Whether their origin is of primary or secondary nature is still discussed as a number of different production scenarios is available including both primary and secondary sites. Due to their small isotopic abundances, it is very unlikely that they are directly observed in stellar spectra. Thus, an assignment by comparison to typically primary elements like, *e.g.*, xenon or typically secondary elements like, *e.g.*, barium is hindered.

Possible production processes The origin of the p nuclei is not completely understood and there is evidence that more than one process in more than one astrophysical scenario is relevant for their production [17]. The original suggestion in [1] – **proton-capture reactions** on stable seed isotopes in supernovae – failed as source of all p nuclei due to the high proton densities and high temperatures needed to overcome the Coulomb barriers in case of the heavy p nuclei [18]. However, the idea revived recently for the lightest

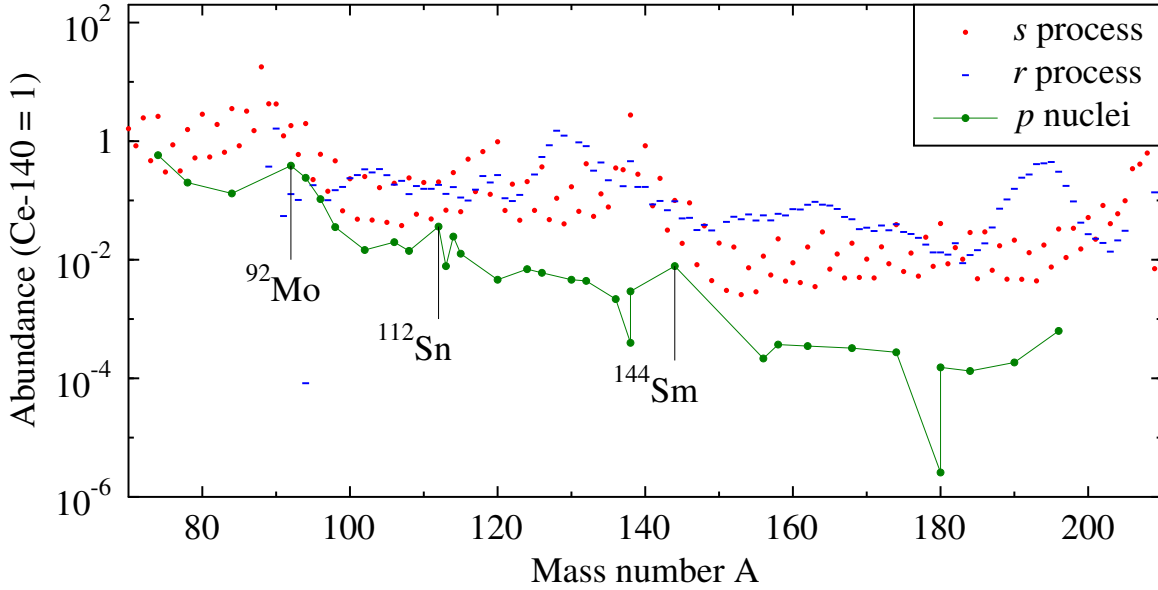


Figure 2.3:

Isobaric abundances synthesized in the p -, r -, and s -processes. The double-peak structures in the solar abundance distribution (compare Fig. 2.1) separately stem from the r and s process. The p nuclei exhibit significantly lower abundances. Data from [13, 14]. Taken from [15].

p nuclei when it was independently found by Kusakabe *et al.* [19] and Travaglio *et al.* [20] that there are significant contributions of proton-capture reactions in thermonuclear supernovae to the abundances of the lightest p nuclei up to ^{92}Mo and ^{94}Mo .

A currently accepted mechanism to explain the abundances of the majority of the p nuclei is the so-called γ process [21]. As explained later on in detail, there are several astrophysical sites where explosive conditions are realized in a way that a seed distribution stemming from r - and s -process nucleosynthesis encounters a series of photodisintegration reactions. At first, (γ, n) or photo-neutron reactions lead the abundances towards neutron-deficient isotopes. Thus, the neutron-separation energy becomes higher and, eventually, (γ, p) and/or (γ, α) reactions start to compete. The isotopes at which the reaction rates for the photon-induced emission of neutrons compared to charged particles, *i.e.*, protons and α particles, are of the same order of magnitude are referred to as branchings [22]. Here, the abundances reach lower charge numbers and are usually closer to stability due to the enhanced neutron-to-proton ratio. As shown in, *e.g.*, [22] and [23], (γ, p) reactions compete at lower masses while (γ, α) reactions are important for higher masses. This interplay continues as long as the temperature is high enough. Afterwards, residual unstable isotopes are converted to their nearby stable isobar in a chain of β^+ - and/or *e.c.*-decays. Fig. 2.4 displays the reaction flow in the mass region of zirconium to ruthenium for a typical temperature of 2.5 GK.

Table 2.1:

List of the 35 p nuclei as defined in [12]. The isotope are sorted by their charge number Z . Their isobaric abundances I_A as plotted in Fig. 2.3 and their isotopic abundances $I_\%$ [16] are listed.

isotope	$I_A / \%$	$I_\% / \%$	isotope	$I_A / \%$	$I_\% / \%$	isotope	$I_A / \%$	$I_\% / \%$
^{74}Se	1.322	0.89(2)	^{114}Sn	5.129	0.65(1)	^{156}Dy	0.317	0.06(1)
^{78}Kr	1.263	0.35(2)	^{115}Sn	6.814	0.34(1)	^{158}Dy	0.448	0.10(1)
^{84}Sr	0.417	0.56(1)	^{120}Te	0.377	0.096(2)	^{162}Er	0.354	0.14(1)
^{92}Mo	16.57	14.84(4)	^{124}Xe	1.525	0.10(1)	^{164}Er	3.636	1.61(2)
^{94}Mo	10.91	9.25(3)	^{126}Xe	0.655	0.09(1)	^{168}Yb	0.470	0.13(1)
^{96}Ru	12.30	5.52(6)	^{130}Ba	0.246	0.106(2)	^{174}Hf	0.347	0.162(3)
^{98}Ru	5.350	1.88(6)	^{132}Ba	0.309	0.101(2)	^{180}Ta	0.261	0.012(2)
^{102}Pd	4.808	1.02(1)	^{138}La	0.107	0.0902(2)	^{180}W		0.13(4)
^{106}Cd	4.808	1.25(4)	^{138}Ce		0.25(1)	^{184}Os	0.339	0.02(1)
^{108}Cd	3.578	0.89(2)	^{136}Ce	0.283	0.19(1)	^{190}Pt	0.104	0.01(1)
^{113}In	3.865	4.3(2)	^{144}Sm	3.775	3.1(1)	^{196}Hg	0.184	0.15(1)
^{112}Sn	8.667	0.97(1)	^{152}Gd	0.975	0.20(1)			

An alternative process leading from lower towards higher mass numbers is the **rp process** [24]. If a neutron star accretes matter from the hydrogen- and helium-rich envelope of a massive developed companion star in a binary system a thermonuclear runaway occurs after helium burning is ignited. Since the energy is mostly released in form of X-ray radiation the event is called an X-ray burst [25]. It is when the thermonuclear runaway starts with the triple- α reaction and, afterwards, the reaction $^{15}\text{O}(\alpha,\gamma)$ provides a break-out from the hot-CNO cycle that the rp process starts. Sequences of (p,γ) reactions and β decays lead to neutron-rich unstable isotopes close to the proton-dripline (see Fig. 2.5). There are several so-called waiting points on the reaction path which have to be passed by (α,γ) or (α,p) reactions as their half-lives are on the order of seconds and the cross sections for (p,γ) reactions are small. A natural termination might be the so-called SnSbTe cycle [26]. Although especially the light p nuclei are produced in the rp process, thus, their underproduction in the γ process being bridged, the question remains how the newly synthesized isotopes can escape the gravitational attraction of the neutron star and enrich the interstellar medium.

The **νp process** occurs in the innermost supernova ejecta made of proton-rich neutrino-heated matter [27]. During the cooling, mostly $N \approx Z$ are produced in an α -rich freeze-out while protons capture neutrinos and convert into neutrons and positrons. The reaction network looks very similar to the rp process besides the fact that (n,p) reactions pass by the waiting points. As the amount of neutrons available depends directly on the electron fraction Y_e , this stellar parameter strongly influences the abundances of the

⁹⁴ Ru 51.8 m	⁹⁵ Ru 1.65 h	⁹⁶ Ru 5.52	⁹⁷ Ru 2.9 d	⁹⁸ Ru 1.88	⁹⁹ Ru 12.7	¹⁰⁰ Ru 12.6
⁹³ Tc 2.7 h	⁹⁴ Tc 4.9 h	⁹⁵ Tc 20 h	⁹⁶ Tc 4.3 d	⁹⁷ Tc 4*10 ⁶ a	⁹⁸ Tc 4*10 ⁶ a	⁹⁹ Tc 2*10 ⁵ a
⁹² Mo 14.84	⁹³ Mo 4*10 ³ a	⁹⁴ Mo 9.25	⁹⁵ Mo 15.92	⁹⁶ Mo 16.68	⁹⁷ Mo 9.55	⁹⁸ Mo 24.13
⁹¹ Nb 680 a	⁹² Nb 4*10 ⁷ a	⁹³ Nb 100	⁹⁴ Nb 2*10 ⁴ a	⁹⁵ Nb 34.97 d	⁹⁶ Nb 23.4 h	⁹⁷ Nb 74 m
⁹⁰ Zr 51.45	⁹¹ Zr 11.22	⁹² Zr 17.15	⁹³ Zr 2*10 ⁶ a	⁹⁴ Zr 17.38	⁹⁵ Zr 64.0 d	⁹⁶ Zr 2.80

Figure 2.4:

Reaction network of the γ process in the mass region of zirconium to ruthenium. Photo-neutron reactions (green arrows) produce isotopes with lower N/Z ratios until (γ, p) and/or (γ, α) reactions start to compete. The situation is shown for a typical temperature of 2.5 GK as presented in [22]. For details, see text.

produced light p nuclei [28].

Besides these three production processes, the charged-particle (α -)process in the high-entropy wind scenario of type II supernovae [29] and a **pn process** [30] were discussed to contribute to the production of all p nuclei. In contrast, the **ν process** occurring in the inner layers of the ejecta of core-collapse supernovae contributes only significantly to the abundances of the extremely rare odd-odd p nuclei ¹³⁸La and ¹⁸⁰Ta due to the extremely low interaction probability of neutrinos for $(\nu, \nu'n)$ and (ν_e, e^-) reactions [31, 32].

Astrophysical sites of the γ process The nuclear reactions occurring in the γ process are mainly induced by photons in the MeV-energy range. According to the Planck distribution (see Eq. (3.6), temperatures of the order of several 10^9 K are required to provide a sufficient amount of these projectiles. Such temperatures are realized within explosive events like, *e.g.*, supernovae. Explosive events also provide the correct timescale of several seconds – if the photon intensity would last for longer times the seed distribution would completely convert to light isotopes without leaving p nuclei behind.

In an early work of Woosley and Howard [21], it was discovered that different conditions are required to produce the complete range of p nuclei from ⁷⁴Se up to ¹⁹⁶Hg. Therefore, different density and temperature profiles were dedicated to different layers of material of a core-collapse supernova. A typical range of peak temperatures is 2 GK

increasing mass number. This trend cannot be corrected by nuclear physics uncertainties as shown in [17] but is based on the model. *E.g.*, the heaviest p nuclei only survive in the outermost layers with the lowest peak temperatures (compare Chap. 6) – an effect which might be overestimated in the current models. Usually, the seed composition is a mixture of r - and s -process nucleosynthesis as found in the solar abundance distribution (compare Fig. 2.1). However, the total amount of p nuclei produced in one event and the expected rate of type II supernovae explosions do not match the absolute observed abundances.

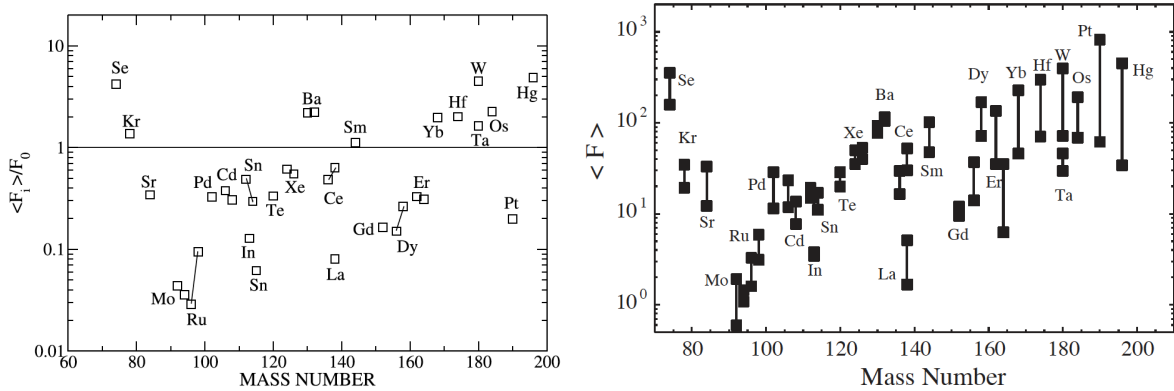


Figure 2.6:

Overproduction factors of p nuclei in type II supernova of $25 M_{\odot}$ star. *left*: The light p nuclei $^{92,94}\text{Mo}$ and ^{96}Ru are most strongly underproduced [23]. *right*: Nuclear uncertainties indicated by the vertical bars are not the only source for the observed trends [17]. For details, see text.

Therefore, type Ia supernovae were investigated as an additional site [36, 37]. In total, the same trend was observed as shown in Fig. 2.6 for type II supernovae. The underproduction of the molybdenum and ruthenium p nuclei was less pronounced may be due to the slightly higher temperatures. Although the total amount of p nuclei produced in one event is higher than for type II supernovae the less frequent occurrence of type Ia supernovae reduces their contribution to the observed abundances [38]. Two recent studies [19, 20] confirm these findings, although the underproduction of $^{92,94}\text{Mo}$ and $^{96,98}\text{Ru}$ is further decreased by an additional contribution to their abundances stemming from proton capture reactions.

Thus, a combination of both type Ia and type II supernovae is needed to match the absolute observed abundances. Their might be additional but small contributions from events occurring less frequently like, *e.g.*, sub-Chandrasekar mass supernovae [30] or pair-creation supernovae [39]. As for type Ia supernovae, processes besides the γ process also contribute at these more exotic sites.

3

Nuclear physics basics

This chapter will briefly summarize the nuclear physics properties and relations which are required to understand the later on described experimental setups, the analysis of the data, and the significance of the results. This includes the cross section σ , the S factor S , and the rate r of a nuclear reaction as well as the Maxwell-Boltzmann and Planck distribution for particles and photons, respectively. Furthermore, reactions mechanisms are discussed shortly.

The measure for the probability of a nuclear reaction to occur is its **cross section** σ defined as

$$\sigma = \frac{N_{\text{reaction}}}{N_{\text{projectile}} \cdot N_{\text{target}}}. \quad (3.1)$$

Usually, the unit of a cross section is an areal unit like cm^2 or $b = 10^{-24} \text{ cm}^2$, *i.e.*, the number of projectiles $N_{\text{projectile}}$ or the number of target nuclei N_{target} is expressed in units of cm^{-2} dependent on whether the beam diameter is smaller or bigger than the diameter of the target. In addition, the number of reactions N_{reaction} is measured per time intervall. Thus, the number of projectiles is expressed as a current for charged particles or as projectiles per time intervall in case of neutrons or photons. Typically, the cross section is dependent on the energy $E_{\text{c.m.}}$ available in the center-of-mass system of projectile and target nucleus.

In nuclear astrophysics, the **S factor** $S(E_{\text{c.m.}})$ was introduced for charged-particle induced reactions to get rid of all energy dependency of the cross section induced by Coulomb repulsion. The cross section $\sigma(E_{\text{c.m.}})$ can be rewritten as

$$\sigma(E_{\text{c.m.}}) = \frac{1}{E_{\text{c.m.}}} \exp(-2\pi\eta) S(E_{\text{c.m.}}) \quad (3.2)$$

with the Sommerfeld parameter η

$$\eta = 31.39 \cdot Z_{\text{projectile}} \cdot Z_{\text{target}} \cdot \left(\frac{\mu}{E_{\text{c.m.}}} \right)^{1/2} \quad (3.3)$$

where Z_i are the charge numbers of projectile and target isotope, respectively, μ is the reduced mass in units of amu, and the center-of-mass energy $E_{\text{c.m.}}$ is in units of MeV.

Then, the S factor is supposed to change only slightly with energy as long as nuclear resonances do not affect the reaction.

In a stellar environment, the particles follow a velocity or energy distribution $\Phi(T, E_{c.m.})$ determined by the temperature T . Due to the energy dependency of the cross section σ , the reaction probability is expressed as a **reaction rate** $r(T)$ convoluting both quantities and multiplying with the number densities N_i of projectiles and target nuclei:

$$r(T) = N_X N_Y \int_0^\infty \sqrt{E_{c.m.}} \cdot \sigma(E_{c.m.}) \cdot \Phi(T, E_{c.m.}) \cdot dE_{c.m.} \quad (3.4)$$

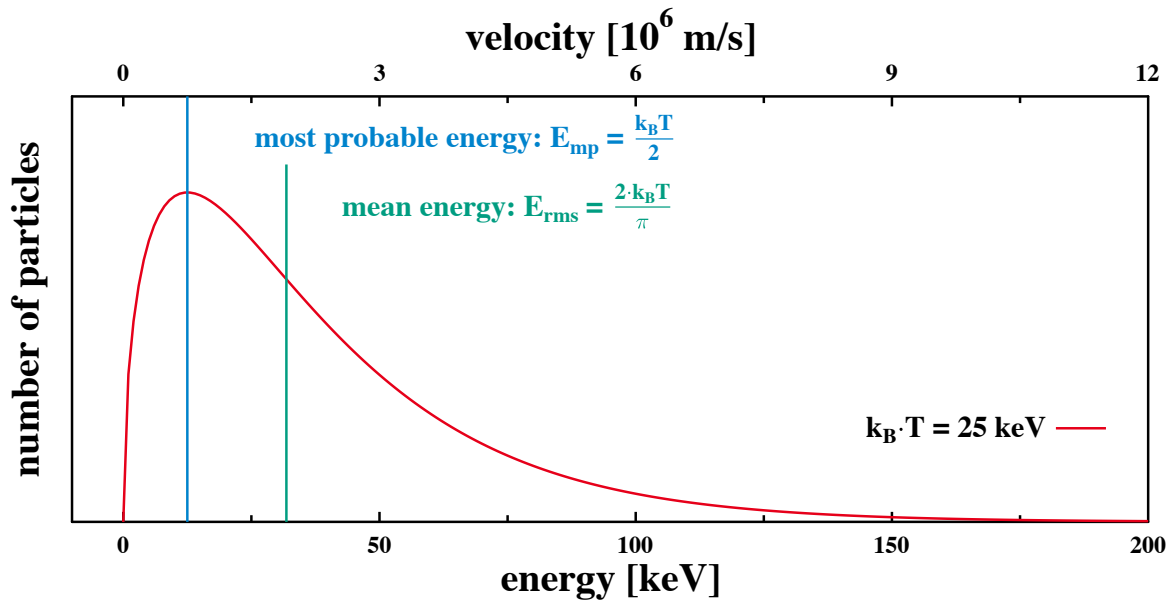


Figure 3.1:

Maxwell-Boltzmann distribution for particles in thermal equilibrium. The probability distribution described in Eq. (3.5) is shown for a temperature of $kT = 25 \text{ keV}$. The most probable energy $E_{mp} = k_B T / 2$ and the mean energy $E_{rms} = 2k_B T / \pi$ are indicated. For non-relativistic cases, the energy corresponds to the velocity according to $E = m/2 \cdot v^2$.

In case of thermal equilibrium, the **Maxwell-Boltzmann distribution** Φ_{MB} is applied if the reaction is induced by particles:

$$\Phi_{MB}(T, E_{c.m.}) \cdot dE_{c.m.} = \frac{2}{\sqrt{\pi}} \cdot \frac{1}{(kT)^{3/2}} \cdot \sqrt{E_{c.m.}} \cdot \exp\left(-\frac{E_{c.m.}}{kT}\right) \cdot dE_{c.m.} \quad (3.5)$$

An example is illustrated in Fig. 3.1. The convolution with the typical energy dependency of a charged-particle induced reaction being dominated by the tunnelling probability results in the implementation of the so-called Gamow window as shown in Fig. 3.2. As the reaction rate $r(T)$ is almost completely determined within the Gamow window,

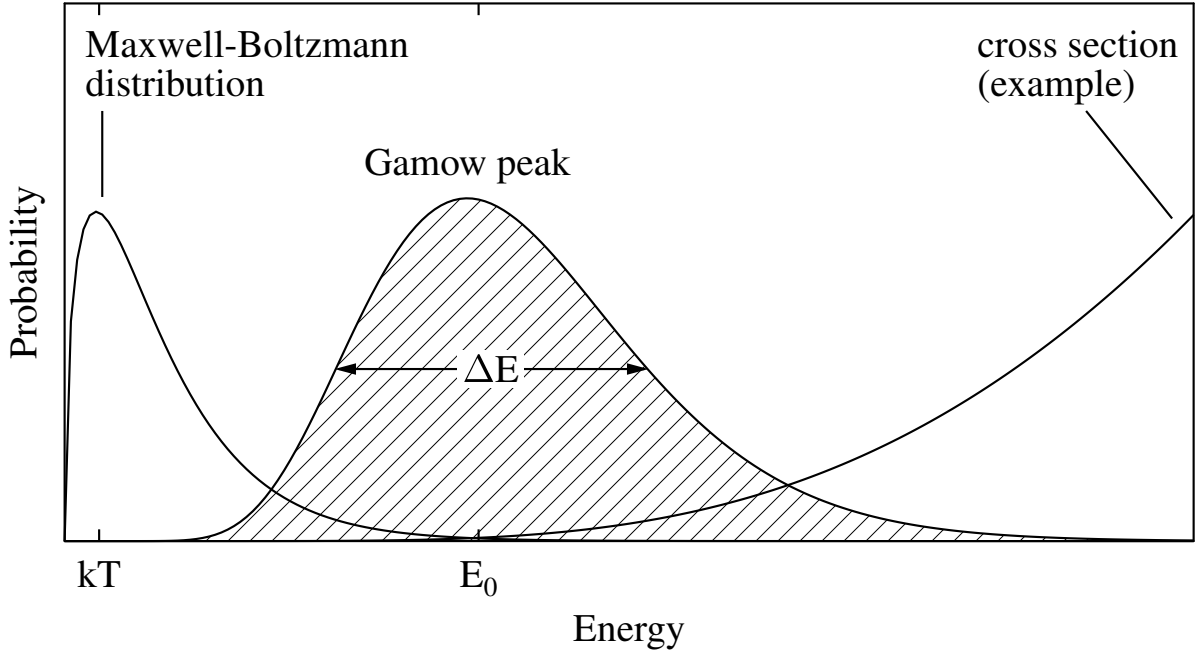


Figure 3.2:

Gamow window of charged-particle induced reactions. The reaction rate r is derived by a convolution of the Maxwell-Boltzmann distribution and the cross section dominated by the tunnelling probability. The integrand exhibits a peak-like structure which approximately follows a Gaussian distribution defined by the mean energy E_0 and the width ΔE .

the cross section $\sigma(E_{c.m.})$ should be investigated in this energy range, lateron also referred to as astrophysically relevant energy range.

If the nuclear reaction is induced by photons, the **Planck distribution** Φ_{Planck} determines the reaction rate $r(T)$:

$$\Phi_{\text{Planck}}(T)dE = \frac{1}{\pi^2(\hbar c)^3} \cdot \frac{E^2}{\exp(E/kT) - 1} \cdot dE. \quad (3.6)$$

An example is illustrated in Fig. 3.3. Usually, photon-induced reactions are endotherm, *i.e.*, the reaction only occurs if the photon energy E_γ enhances a certain threshold energy E_{thr} . *E.g.*, the threshold energy of a (γ, n) reaction is the neutron separation energy S_n of the target nucleus. If the reaction rate $r(T)$ is calculated according to Eq. (3.4) using the Planck distribution and a typical threshold behaviour for (γ, n) reactions, *i.e.*, $\sigma_{(\gamma, n)}(E_\gamma) \propto \sqrt{E_\gamma - S_n}$, the integrand has a maximum close to $E_\gamma = S_n + kT/2$. Thus, a Gamow-like window can also be determined for photon-induced reactions (compare Fig. 3.4).

A nuclear reaction can proceed via different **reaction mechanisms** which are not easily disentangled by experiments. However, for the theoretical prediction of the cross section

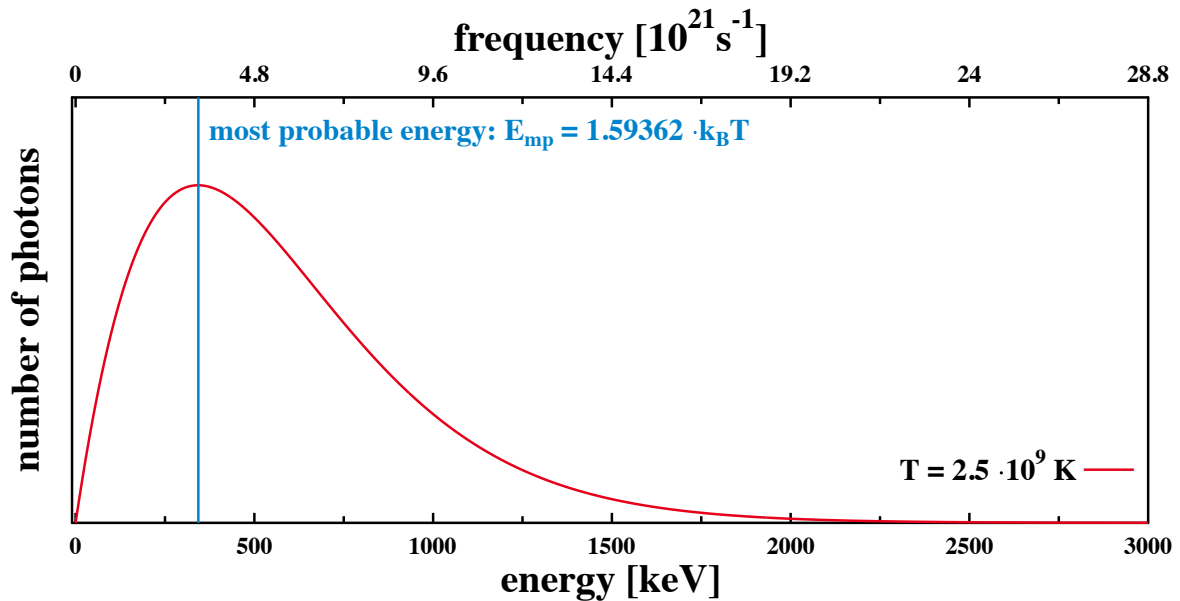


Figure 3.3:

Planck distribution for photons. The probability distribution described in Eq. (3.6) is shown for a temperature of $T = 2.5$ GK. The most probable energy is found by $E_{\text{mp}} \approx 1.6 \cdot k_B T$. The energy corresponds to the frequency ν and the wave length λ of the electro-magnetic wave representing the photon according to $E = h\nu = hc/\lambda$.

(or the reaction rate) it is mandatory to know the reaction mechanism to allow modelling the nuclear process correctly. In the energy range covered by nuclear astrophysics, two major categories occur: direct reactions and resonant reactions [40]. The former directly connects the initial and final states of target and product nucleus and is possible for all energies as spare energy is emitted as electromagnetic radiation. The later only takes place if the energy of projectile and target nucleus matches exactly a nuclear level in the compound nucleus (CN) to be formed. At these energies, the cross section of the reaction is increased significantly and exhibits a resonance-like behaviour. Therefore, a nuclear level is often referred to as resonance.

If the compound nucleus is produced at very high excitation energies as it is often the case in explosive astrophysical scenarios, the level density ρ can be so high that the average level spacing $\langle D \rangle = 1/\rho$ is smaller than the average resonance width $\langle \Gamma \rangle$, *i.e.*, the levels are largely overlapping. In that case, the reaction can be described by average resonance properties instead of taking into account the usually unknown properties of all individual resonances. This is realized by the **Statistical** or **Hauser-Feshbach Model** [41] which is broadly applied for the prediction of reaction rates in explosive astrophysical scenarios [42].

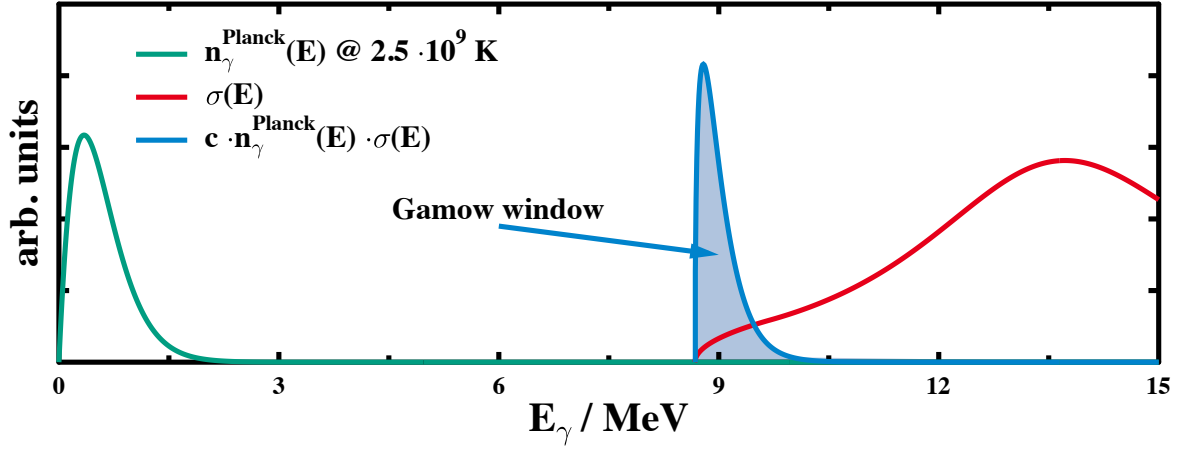


Figure 3.4:

Gamow-like window of photon-induced reactions. The reaction rate r is derived by a convolution of the Planck distribution and the cross section of a (γ, n) reaction dominated by the threshold behaviour. The integrand exhibits a peak-like structure close above the reaction threshold with a maximum located near $E_\gamma = S_n + kT/2$.

3.1 Calculation of reaction rates

In explosive astrophysical scenarios, the center-of-mass energy of projectile and target nucleus is below 20 MeV. Thus, the resonant reaction mechanism is dominating at usually high level densities. This compound-nucleus (CN) reaction is described within the Statistical Model as



with the target nucleus A in the initial state μ , the compound nucleus C in a high-energy excited state, and the product nucleus B in the final state ν . Projectile and Ejectile are denoted a and b , respectively. In case of a radiative capture reaction, the compound nucleus is already the product nucleus and only γ rays act as ejectiles.

The typical life-time of the compound nucleus is much longer than the transit time of the projectile across the target nucleus. Therefore, the energy available in the compound nucleus is equally distributed to all its constituents and the information about its formation is lost. According to the independence hypothesis by Niels Bohr [43], the formation and the decay of the compound nucleus are two distinct processes and can be described individually to derive the total cross section of the compound-nucleus reaction:

$$\sigma_{\text{CN}}^{A+a \rightarrow B+b} = \sigma_{\text{form}}^{A+a} \cdot \sigma_{\text{decay}}^{B+b}. \quad (3.8)$$

Both factors in Eq. (3.8) can be written as function of averaged resonance widths $\langle \Gamma \rangle$ or in terms of transmission coefficients T derived from the optical model [44]. The variables used in the following equations are explained in Fig. 3.5. If width fluctuations are not

corrected the cross section σ_{CN} is given by

$$\sigma_{\text{CN}}^{\mu} = \frac{\pi}{k_{\mu}^2} \frac{1 + \delta_{Aa}}{(2J_A^{\mu} + 1)(2J_a + 1)} \sum_{J, \pi} (2J + 1) \frac{T_A^{\mu} \cdot T_B^{\nu}}{T_{\text{tot}}} \quad (3.9)$$

with the wave number of the initial state k_{μ} , the transmission coefficient for the formation of the compound nucleus from the target nucleus A in state μ T_A^{μ} , the transmission coefficient for the decay of the compound nucleus to the state ν of the product nucleus B T_B^{ν} and the total transmission coefficient T_{tot} represented by the sum of all allowed decay channels to the same final state ν :

$$T_{\text{tot}} = \sum_{\text{chn}, \nu} T_{\text{chn}}^{\nu}. \quad (3.10)$$

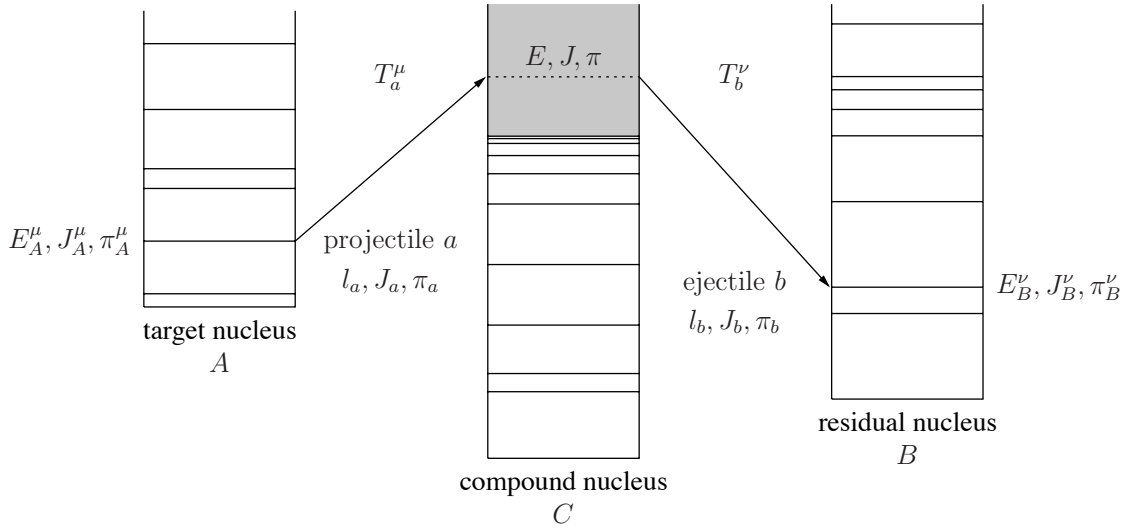


Figure 3.5:

Schematic view of a compound-nucleus reaction $A^{\mu}(a, b)B^{\nu}$. The reaction of target nucleus A^{μ} in state μ and projectile a forms the compound nucleus C in a highly excited state. The probability of this transition is described by the transmission coefficient T_A^{μ} . Similarly, the decay of the compound nucleus C in an energetically allowed channel composed of the product nucleus B^{ν} in state ν and the ejectile b is represented by the transmission coefficient T_B^{ν} . Both transmission coefficients depend on the energies $E_{i,f}$, spins $J_{i,f}$, and parities $\pi_{i,f}$ of the corresponding initial and final states i and j , respectively. The grey-shaded area mark exemplarily the energy range where a calculated level density ρ is used instead of information of discrete levels. Similar to [45].

The transmission coefficients for the formation and decay of the compound nucleus depend on energy E , spin J , and parity π of the target and product nuclei as well as of

the compound nucleus:

$$\begin{aligned} \text{formation : } T_A^\mu &= T_A^\mu(E_A^\mu, J_A^\mu, \pi_A^\mu, E, J, \pi) \\ \text{decay : } T_B^\nu &= T_B^\nu(E_B^\nu, J_B^\nu, \pi_B^\nu, E, J, \pi). \end{aligned} \quad (3.11)$$

If the calculated cross section is to be compared to the result of a measurement in which the populated states in the product nucleus are not distinguished the transmission coefficient for the decay of the compound nucleus T_B^ν must be replaced by the sum of all possible states ν :

$$T_B^{\text{total}} = \sum_{\nu} T_B^\nu. \quad (3.12)$$

The Hauser-Feshbach model is realized in a variety of codes like *e.g.*, SMARAGD [44] and TALYS [46]. While the implementation of the formalism described above is similar in each of the codes, numerics are treated differently. However, discrepancies between results derived with the different codes usually stem from different standard inputs for the nuclear physics like optical model potentials, the γ -ray strength function, nuclear level densities, and nuclear masses, respectively. Table 3.1 provides an overview for the mentioned codes.

Table 3.1:

Standard nuclear inputs of different implementations of the Hauser-Feshbach model. Usually, the nuclear physics input like optical model potentials (OMP), the γ -ray strength function (γ SF), nuclear level densities (NLD), and nuclear masses (NM) can be varied within the codes. The default settings for the codes SMARAGD [44] and TALYS [46] are listed.

	SMARAGD [44]	TALYS [46]
n-OMP	semi-microscopic [47, 48]	phenomenological [49]
p-OMP	semi-microscopic [47, 48]	phenomenological [49]
α -OMP	phenomenological [50]	folding potential [51]
γ SF	lorentzian with low-energy tail [42]	Brink-Axel lorentzian [52, 53]
NLD	updated parametrization [54] plus parity distribution [57]	generalized superfluid model [55, 56]
NM	microscopic [58, 59]	microscopic [60], experimental data [61]

The **Optical Model Potentials** (OMP) describe the average interaction between a particle and a nucleus without using a detailed internal nucleonic structure of both. They are generally described by complex functions $U(r)$ taking into account the absorption of the projectile described by the imaginary part of the strong interaction $W(r)$, the scattering of the projectile described by the real part of the strong interaction $V(r)$, and

the Coulomb interaction $V_C(r)$ for charged projectiles:

$$U(r) = V_C(r) + V(r) + iW(r). \quad (3.13)$$

The name stems from the analogue approach for the complex refraction index in optics. There are different approaches to construct such a potential. Phenomenological potentials are parameterizations which are based on and fitted to a selection of experimental data (*e.g.*, [62] for α particles) and usually provide reliable predictions only within the used data base. The parameters of typical nuclear potentials of Woods-Saxon, Gauß and Fourier-Bessel type, respectively, can be determined from elastic scattering only. However, these fits are not directly applicable to nuclear reactions because of continuous-like and discrete-like ambiguities. The former are due to correlations of the fit parameters like the depth and width of Woods-Saxon type potentials. The latter is referred to as family problem (see, *e.g.*, [63]) and relies on the wave function of the nuclear interior not affecting the cross section for elastic scattering.

In contrast, microscopic potentials are calculated using a certain nucleon-nucleon interaction and only an absolute adjustment is based on experimental data (*e.g.*, [47] for protons), thus, globally applicable potentials are aimed for. Combining both approaches yields a semi-microscopic approach where, *e.g.*, the real part of the nuclear potential stems from microscopic calculations and the imaginary part is adopted by a phenomenologically derived shape. The potential for α particles by [64] shows the success of this approach if the internal structure of the projectile cannot be neglected completely.

The **γ -ray Strength Function** (γ SF) describes the electro-magnetic interaction of photons and nuclei with the main contributions stemming from E1 and M1 transitions. Usually, the E1 transitions dominate the cross section, thus, M1 transitions are neglected [17]. However, it was recently found that this assumption might not be valid for the zirconium isotopes [65, 66]. As for optical model potentials, γ -ray strength functions can be either parameterized by Lorentzian functions [67] or calculated from microscopic approaches based on, *e.g.*, Quasiparticle Random-Phase-Approximation on top of Hartree-Fock calculations [68, 69].

The largest uncertainties for nuclear astrophysics applications stem from the unknown behaviour of the γ -ray strength function at very low energies. Based on experimental data, this behaviour is usually extrapolated and varies significantly [70] even though low-energy components like the pygmy dipole resonance [71] are taken into account. Therefore, new setups providing experimental access to this energy range were recently developed [72].

The **Nuclear Level Density** (NLD) as a function of the energy of excited states E_x as well as their spin J_x and parity π_x relates the averaged resonance widths $\langle\Gamma\rangle$ to the transmission coefficients T . For isotopes at or close to the valley of stability, the properties of excited states are known experimentally. However, a complete list of discrete levels is needed for the calculation of a cross section. Therefore, codes like TALYS or

SMARAGD apply a cut-off energy as soon as one of the properties is not known without ambiguities and use descriptions of the nuclear level densities for higher energies.

Phenomenological models include the Backshifted Fermi Gas Model (see, *e.g.*, [54]), the Constant Temperature Model [73], and the Generalized Superfluid Model [55] being a combination of the former ones. Microscopic and pairing corrections are crucial and extracted from mass models [42]. Completely microscopic models are available based on Hartree-Fock calculations [74] and on the Shell Model Monte-Carlo method [75] and provide similar precision.

The **Nuclear Masses** (NM) are used to calculate the particle separation energies or the Q value of a nuclear reaction and, thus, determine the excitation energy available in the compound nucleus. If different nuclear masses are used a variation in open reaction channels and allowed transitions is expected. In addition, the reciprocity relation of reaction rates is strongly influenced by the Q value of the reaction [44].

Most mass models describe known masses with roughly the same accuracy but differ significantly for extrapolated values [76, 61]. Although phenomenological approaches are available (*e.g.*, [77]), nuclear masses are usually determined from microscopic calculations. The Finite Range Droplet Model (FRDM) is used with shell-model corrections by Duflo and Zuker [78] and in a semi-microscopic approach by Moller *et al.* [58]. Another example is the Extended Thomas Fermi Theory with Strutinski Integral (ETFSI-Q) [79, 59].

4

Experimental methods

A variety of reactions is of interest for the modelling of the nucleosynthesis of the p nuclei. The experimental investigation of these reactions relies on a number of different experimental methods. The general features of the activation approach, the in-beam technique, and the usage of inverse kinematics as used within this work are explained. As a guideline for the applicability of the three methods, a table summarizes their special characteristics, advantages, and limitations. Details of the realization of experiments related to p -process nucleosynthesis will be presented in Chap. 5.

4.1 Activation approach

The most widely used method in recent studies related to p -process nucleosynthesis is the activation approach (see, *e.g.*, [80, 81, 82, 83, 84, 85, 86, 87] and references therein). This is on account of the low isotopic abundances of the p nuclei preventing the availability of large amounts of highly enriched target material. Thus, the activation approach is often the only method with sufficient sensitivity and selectivity to yield in an analyzable signal-to-background ratio.

An experiment using the activation approach is realized in two separated steps. At first, the target is irradiated at an accelerator facility with the projectiles of interest. Afterwards, the number of reactions is determined in an environment optimized regarding the signal-to-background ratio. Since, on the one hand, no limitations of choosing a measuring method occur due to the decoupling from the irradiation site and, on the other hand, shielding against natural background combined with an ideal geometry are possible, lowest activities become detectable. Therefore, the restricting combination of low amount of target material and small cross sections can be overcome.

However, there has to be a fingerprint of the reaction which is detectable after the reaction occurred. In general, radioactive decay provides such a signature if the half-life is in an appropriate time range that the induced activity is detectable. The γ rays emitted after α or β decay show a unique energy and branching pattern to be used as signal of the reaction. High-resolution γ spectroscopy with high purity Germanium (HPGe) detectors is widely used to measure the decay spectra of the reaction products. The high resolution can be used to separate the peaks at energies of interest into contributions of signal and background. Furthermore, the usage of naturally composed targets

is possible if the decay patterns of isotopes produced by different reactions do not overlap completely which is only the case if different reactions lead to the same radioactive isotope. If the energies of the γ transitions are alike by chance different half-lives of the decaying isotopes allow disentangling the single contributions by observing the activity for a sufficient amount of time (see Fig. 4.1). If naturally composed material is used several reactions can be investigated with one activation experiment. Thus, the method is perfectly suited to perform systematic studies for an isotopic chain [88] or investigate different reactions induced by the chosen projectile simultaneously [89].

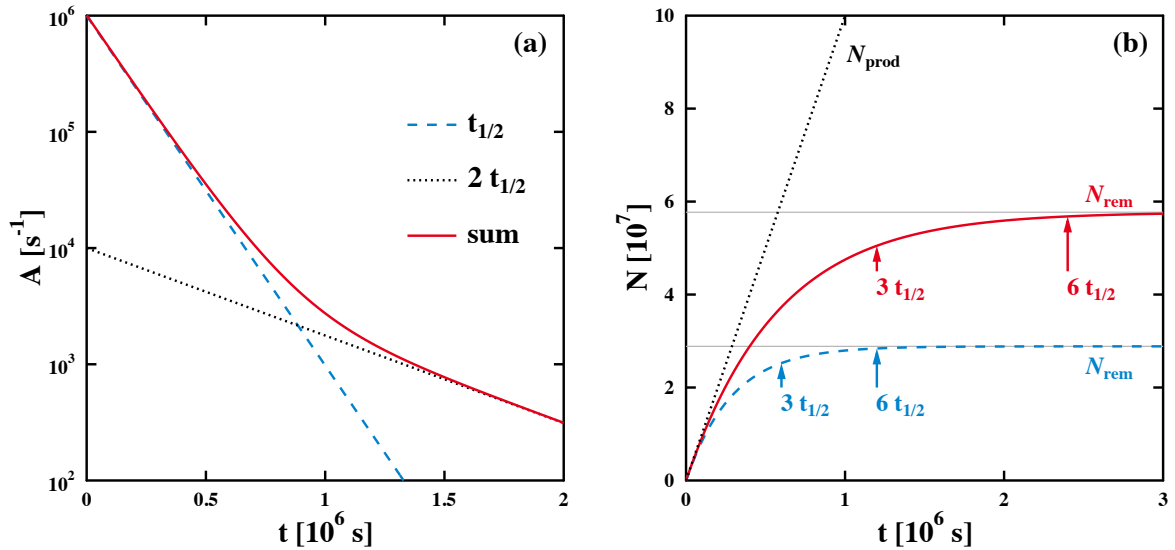


Figure 4.1:

Influence of half-life on activity. (a) Disentanglement of decays with different half-lives. If the activity in a given energy range of the spectrum stems from more than one decay the different contributions can be determined by observing the activity as a function of time. (b) Limitation of remaining activity. Due to the radioactive decay of the produced isotopes, there is a maximum amount of activity producible for a given production rate β . For more details, see text.

The half-life of the reaction product significantly influences the applicability of the activation approach. Certainly, reactions with stable product isotopes are excluded. Very long half-lives might reduce the activity below the detection limit of γ spectroscopy but other methods like, *e.g.*, accelerator mass spectrometry (AMS) might be used instead [90]. In contrast, a half-life being too short can prevent from the production of sufficient remaining nuclei at all. The maximum amount of remaining radioactive nuclei, the saturation limit N_{max} , is given by

$$N_{\text{max}} = \frac{\beta}{\lambda} \quad (4.1)$$

with the production rate β and the decay constant λ of the reaction product. Generally, $0.875 N_{\text{max}}$ and $0.984 N_{\text{max}}$ are reached after three and six half-lives $t_{1/2}$, respectively

(compare Fig. 4.1). If saturation is reached, a further activation is not desirable. The production rate β is limited by the reaction cross section σ and characteristics of the beam Φ and the number of target nuclei N_{target} , respectively:

$$\beta = N_{\text{target}} \cdot \sigma \cdot \Phi. \quad (4.2)$$

For charged-particle induced reactions, the beam is characterized by its current in units of s^{-1} and the amount of target nuclei is given as an areal density in units of cm^{-2} derived from the mass, thickness, and density of the target material. While the current can be measured very precisely and also accurately if an electron suppression potential is applied, the determination of the areal density with small uncertainties is difficult. Average values are derived measuring the target mass and area. In contrast, Rutherford Back-Scattering yields the thicknesses of the irradiated spots at the target's surface. Usually, a combination of both methods is applied as the former one yields smaller uncertainties but the assumption of homogeneity needs verification with the latter one. For photon-induced reactions, the beam is characterized by its intensity in units of $\text{s}^{-1}\text{cm}^{-2}$ and the amount of target nuclei is given as a unitless number proportional to the target's mass. Since all sources of high-energy photons with adjustable energy deliver a spectrum of different energies the distribution must be derived and normalized in the experiment. In case of bremsstrahlung photons, the spectral distribution is simulated using the Monte-Carlo technique as provided by, *e.g.*, the simulation toolkit **Geant4** [91]. Then, the absolute value is determined, *e.g.*, from a measurement relative to a standard reaction with well-known cross section. Usually, the determination of the intensity yields rather high uncertainties up to 10%.

Furthermore, the analysis of data derived from the activation approach relies on a precise knowledge of characteristics of the observed decay, such as the half-life $t_{1/2}$ and the emission probability of the detected γ transitions I_γ (for derivation, see Subsec. 5.1.1). Using an activated target, these properties can be determined with the needed accuracy. In contrast, the determination of the absolute detection efficiency ε with a small uncertainty is a very challenging task. Again, simulations are combined with measurements using appropriate calibration sources. In case of complicated decay patterns, summing effects are usually determined with an activated target.

Although the experimental setup needed for the activation approach is in some degree basic compared to the setups needed for the techniques described in the following sections, the precise and accurate knowledge of the parameters of the analysis request a very detailed and sophisticated scheduling of the experiment and does not allow post-experimental adjustments.

4.2 In-beam technique

The term in-beam technique is used for a large variety of experimental methods with the common feature of determining the number of occurred reactions during the irradiation

of the target. Thus, the major advantage of the in-beam technique compared to the activation approach is its general applicability since the reaction products need not be measurable off-line. Possible realizations are manifold and optimized to the investigated reaction. In the following, calorimetric and spectroscopic measurements of charged-particle induced radiative capture reactions are taken into account.

In standard kinematics, the product nuclei of a radiative capture reaction usually do not yield a sufficient amount of energy to escape from the target. Therefore, the prompt γ rays emitted during the instantaneous de-excitation of the product nuclei are detected as signature of the nuclear reaction. Basically, two approaches can be distinguished. If the Q value of the reaction serves as its fingerprint the complete emitted energy must be detected. This approach yields information about the total cross section and is called calorimetric. In contrast, a spectroscopic measurement observes the energies of the individual γ transitions of the de-excitation. The analysis of the data is more complex and relies to some extent on the knowledge of the level scheme of the product nucleus. In exchange, a lot of additional information is included in the data. *E.g.*, partial cross sections, *i.e.*, the probability for the population of a certain excited state in the nuclear reaction, can be extracted from the data.

In **calorimetric measurements**, the efficiency to detect all emitted γ rays is to be optimized. Therefore, the detector materials should provide a high intrinsic efficiency for γ rays in the energy range of about 100 keV to several MeV are chosen. The energy resolution of the material is of less importance. This results in the application of anorganic scintillator detectors like, *e.g.*, NaI(Tl) [92, 93] or BaF₂ [94, 95]. As the γ rays are emitted in the full solid angle, the detector material should completely surround the target in a 4π geometry.

One possible realization is a monocrystal with a borehole for the beam-line with the target at the end [92]. The resulting spectra ideally contain a single peak, the so-called sum peak, with the energy of the Q value of the observed reaction. The area of the peak yields the total cross section even though the multiplicities of the events, *i.e.*, how many γ transitions occurred, is unknown. The volume of the monocrystal can be read-out by several photomultipliers in addition to the core signal similar to so-called polarimeters [96]. Then, the multiplicities can be determined and used to derive the corresponding efficiencies of the sum peak by means of Monte-Carlo simulations. This is important to identify background contributions in the sum peak.

The second realization is to surround the target by a so-called detector array, *i.e.*, individual detector modules are read-out in coincidence to collect the complete emitted energy in one spectrum [93, 94]. In that case, the multiplicities can be extracted from the number of detector modules measuring a signal. Background events are excluded by unlikely multiplicities and by the trigger conditions of the coincidence. If the detector becomes highly segmented [95], higher detection rates can be measured. However, the detector response of an individual module influences the relation between the multiplicity of the event and the number of detector modules measuring a signal. In any case, Monte-

Carlo simulations are mandatory to derive the detection efficiency of the system.

In **spectroscopic measurements**, detectors with a high energy resolution are needed as the different γ transitions must be distinguishable in the measured spectra. Therefore, HPGe detectors are usually applied [97, 98]. It is important to cover different angles with the detectors with respect to the incoming beam as the the measured yield of a certain γ transition exhibits an angular correlation. This aim is reached with one detector per angle and successive measurements [97] or with a detector array [98]. In both cases, the energy and time information of the signals are detected and analyzed. The singles spectra of the different detectors can be added or analyzed in coincidence mode to suppress background. If needed, the statistics in the full-energy peaks can be enhanced by an addback algorithm to adjust for the detector response.

As explained in detail in Subsec. 5.1.2, the analysis of the data depends on the knowledge of the level scheme of the product nuclei. Usually, the level schemes are not completely known up to the energies of the populated entry states. Therefore, the total cross section derived from the analysis of a spectroscopic measurement is always a lower limit of the actual one. The lower the energy of the entry state, *i.e.*, the lower the energy of the projectiles, the less influence is expected. Thus, the method is well-suited to study cross sections in the astrophysically relevant energy range.

The complex data provides more information than the total cross section. *E.g.*, partial cross sections are determined if the transitions depopulating the entry state are analyzed. As shown in [99], partial cross sections allow testing the reliability of Hauser-Feshbach predictions in more detail and, sometimes, yield valuable information on nuclear structure features like the observation of doublet states.

No matter which one of the described methods for the detection of the prompt γ rays is used, a major task using the in-beam technique is the **reduction of background** in the measured spectra. The background consists of components stemming from the beam and the target. Natural sources can usually be neglected. Beam-induced background stems from the beam reacting with, *e.g.*, residual gas in the beam-pipe or other material in the vicinity of the target. The contribution to the measured spectra is sometimes overwhelming despite the cross sections of the corresponding reactions being orders of magnitude lower than for the reaction of interest as the amount of corresponding target nuclei is enlarged in the same degree. An improvement is possible by a minimization of background-inducing target material with, *e.g.*, special coatings of target chambers [98]. In general, the application of inverse kinematics can significantly reduce beam-induced background due to further reduced cross sections (compare Sec. 4.3).

Target-induced background has to be divided in two different contributions. In general, the signals expected of the observed reaction can overlap with reactions induced on other isotopes available in the target material. Therefore, the usage of highly-enriched target material is usually mandatory. If the enrichment is not sufficient due to the very low natural abundance of the p nuclei the contributions of other reactions to the spectra

have to be subtracted and introduce an additional uncertainty (see, *e.g.*, [66]).

The second contribution stems from the target material itself either if other reactions such as scattering occur or if other reaction channels are open. Here, the background signals usually differ from the ones expected for the reaction of interest or only influence part of the signals [100]. However, the additional amount of data can significantly enlarge the dead-time of the detection systems and render the measurement impossible.

In case of photon-induced reactions, the in-beam technique provides an additional advantage compared to the activation approach. As mentioned in Sec. 4.1, high-energy photons are not available as adjustable monochromatic projectiles. Therefore, the activation approach always yields an energy-integrated cross section (compare Subsec. 5.2.1). In an in-beam experiment, high-energy photons can be tagged, *i.e.*, their energy is assigned by the measurement of the energy loss of the electron which produced the photon by bremsstrahlung [101]. If the signature of the reaction is detected in coincidence, the cross section $\sigma(E)$ is determined without the application of a deconvolution procedure [102]. A similar rationale is valid for neutrons as projectiles if their time-of-flight for a given distance is used to determine their energy [103].

4.3 Inverse kinematics

A nuclear reaction is generally described with a reaction equation analogue to chemistry:



where A and B are the heavy target and product nuclei and a and b denote the light projectile and ejectile, respectively. In a fixed target experiment or in standard kinematics, the projectiles a are usually accelerated up to the desired energy and hit the target nuclei A . However, at energies relevant in nuclear astrophysics, this can result in huge contributions to the background by the interaction of the projectiles with, *e.g.*, rest gas atoms in the beam-pipe close to the target. Since the Coulomb barrier is higher for the heavier target nuclei A this contribution can be suppressed by performing the experiment in inverse kinematics where the role of target nucleus and projectile is exchanged [104]. Therefore, the reaction equation reads:



Another application of inverse kinematics is the usage of a so-called recoil mass separator experiment [105]. In standard kinematics, the heavy product nuclei do not have sufficient energy to escape from the target. Now, the heavy projectiles A hit the lighter target nuclei a usually provided as a gas target. Due to the kinematics, the reaction products B are boosted towards the same direction as the projectiles A . The challenge of a recoil mass separator consisting of several stages of momentum, velocity, and mass dependent

filters is to distinguish between projectiles A and reaction products B with the former ones exceeding the amount of the latter ones by many orders of magnitude [106].

Nowadays, the a popular application of inverse kinematics is in combination with radioactive or rare ion beams (RIB). Although a number of long-lived radioactive isotopes can be produced and prepared as a target (compare Subsec. 5.1.2) it is generally not possible the study reactions with radioactive target nuclei A in direct kinematics as described by Eq. (4.3). It is still challenging to produce a RIB either by the ISOL or the in-flight method. However, the range of nuclei accessible with sufficient intensity to perform reaction studies is further growing with new facilities like, *e.g.*, RIKEN (Japan), FRIB (U.S.A.), SPIRAL-2 (France), and FAIR (Germany).

If the energies of the RIBs are in the energy range of astrophysical interest they can be used in inverse kinematics with the same techniques as used for stable beams. *E.g.*, the recoil mass separator DRAGON [107] was successfully used to measure several reaction cross sections relevant for novae explosions. The ISOL facility ISAC at TRIUMF provides also RIBs with higher mass numbers. In future, DRAGON might also be used to measure reaction cross sections relevant for p -process nucleosynthesis. The suitability of DRAGON's magnets was already proven with stable beams [105]. The $^{74}\text{Se}(\alpha,\gamma)$ reaction was recently studied in the low-energy range of the Gamow window applying for p process nucleosynthesis [108].

A possibility to use RIBs efficiently and, in addition, provide them with the low energies of only several MeV per nucleon as needed for studies related to p -process nucleosynthesis is their feeding in a storage ring like, *e.g.*, the Experimental Storage Ring (ESR) at the GSI Helmholtzzentrum für Schwerionenforschung (GSI), Darmstadt, Germany. The stored ions hit a gas jet target consisting of hydrogen or helium to study proton- or α -induced reactions, respectively. In that way, the reactions $^{96}\text{Ru}(p,\gamma)$ and $^{124}\text{Xe}(p,\gamma)$ were investigated as first test cases [109].

If photon-induced reactions are to be studied the construction of a photon target is a further challenge. At GSI, relativistic radioactive ion beams are used to study Coulomb dissociation in inverse kinematics [110]. The extraction of a cross section relies on the invariant mass method, thus, the detection setup must provide the possibility to study the complete kinematics of the reaction. An application for the rp process investigated resonances in the cross section of the $^{30}\text{S}(p,\gamma)$ reaction [111]. A specially designed low-energy neutron-detector array LENA [112] allows extracting information about the electron capture decay of excited states by the study of (p,n) reactions [113]. The application of the method for the investigation of the cross section of the $^{100}\text{Mo}(\gamma,n)$ is described in detail in Sec. 5.2.2.

5

Experiments and analysis

The previous chapter gave a short summary about the characteristics of different experimental approaches used within this work. The realization of experiments performed to understand p -process nucleosynthesis is discussed in the following sections. The two parts deal with charged-particle induced reactions and photon-induced reactions. Both can be used to perform systematic studies related to a better knowledge about the nuclear physics input for the prediction of reaction rates within the Statistical model (compare Sec. 3.1). Each of the sections starts with the description of a systematic study performed within this work. Afterwards, the experimental study of reactions with particular influence for the production of the p nucleus ^{92}Mo is explained in detail, *e.g.*, the $^{90}\text{Zr}(p,\gamma)$ and $^{91}\text{Nb}(p,\gamma)$ reactions are discussed in the first section.

5.1 Charged-particle induced reactions

Although charged-particle induced reactions – such as (p,γ) or (α,γ) reactions – are implemented in the network codes to simulate p -process nucleosynthesis in the γ process they are usually not very important for the reaction flow since the Coulomb barrier permits the corresponding reaction rates to become sufficiently large. An exception are radiative proton-capture reactions in the case of light p nuclei as explained in Subsec. 5.1.2.

However, the study of (p,γ) and (α,γ) reactions is of importance since the principle of detailed balance provides the possibility to calculate the reaction rates of the corresponding inverse (γ,p) and (γ,α) reactions, respectively. In fact, the theoretical prediction of the stellar reaction rate, *i.e.*, contributions of excited states are taken into account, is better based on data of the inverse reaction [42]. Detailed knowledge about (γ,p) and (γ,α) reactions in the stellar environment is important to understand where their competition with (γ,n) reactions leads to a bending of the reaction flow towards elements with lower charge number Z . The location of these so-called branchings of the γ process are important for the final abundance distribution (compare Sec. 6.1). Figure 5.1 indicates the (α,γ) and (p,γ) reactions for which published data is available close to the Gamow window.

A famous example is the study of the $^{144}\text{Sm}(\alpha,\gamma)^{148}\text{Gd}$ reaction by E. Somorjai and co-workers [115]. They used the activation method to investigate the cross section in an

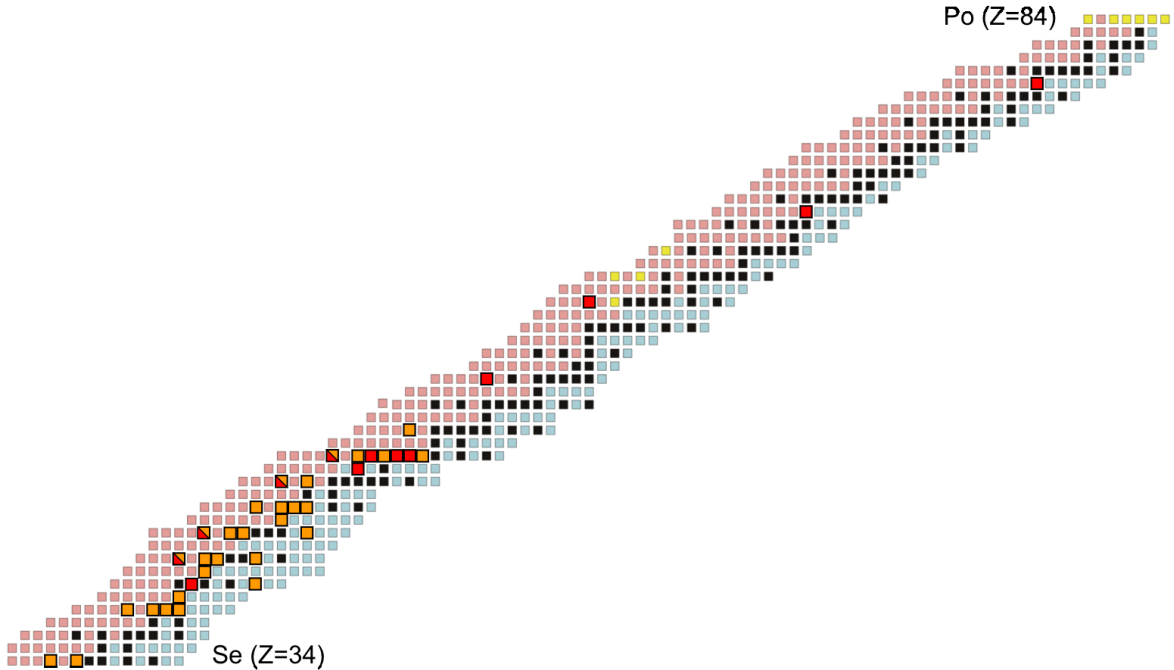


Figure 5.1:

Overview of experimentally investigated (p,γ) and (α,γ) reactions. In this part of the nuclidic chart, isotopes are highlighted if the (p,γ) reaction (orange) and/or the (α,γ) reaction (red) are experimentally investigated in the energy range relevant for the nucleosynthesis of the p nuclei in the γ process. Data from [114].

energy range of 10.5 MeV to 13.4 MeV, thus, well-covering the complete Gamow window. The extracted reaction rate of the inverse $^{148}\text{Gd}(\gamma,\alpha)^{144}\text{Sm}$ reaction was a factor of ten to six smaller than the one predicted within the Statistical model at that time. This allowed the discussion of the possibility of a late contamination of the solar system by one or several core-collapse supernovae by the examination of the $^{146}\text{Sm}/^{144}\text{Sm}$ ratio in the solar abundance distribution.

Since the investigation of the inverse reaction in direct kinematics relies on the fact that the product nucleus is stable the majority of the predicted key reactions is not accessible in this way (compare Tab. 6.1). Therefore, it is mandatory to provide reliable predictions of these reaction rates. As described in Sec. 3.1, this task is usually performed within the framework of the Statistical model and it is necessary to provide approved nuclear physics input such as optical model potentials (OMP). The following Subsec. 5.1.1 summarizes the efforts towards globally applicable particle-nucleus OMPs and highlights recent results using (α,n) and (p,n) reactions, respectively.

5.1.1 Studies to improve optical potentials

Optical model potentials (OMP) are used in the framework of the Statistical model to derive the transmission coefficients if particles interact with the nucleus (compare Sec. 3.1). There are different ways to test the reliability or derive a parameterized description of an OMP. All of them rely on the comparison of experimental data and the corresponding predicted values. In case of the derivation, the parameters are determined by a fit to the experimental data. All relevant data should be used for the fit simultaneously to ensure a global applicability as needed for p -process nucleosynthesis.

Once the parameterization is available its reliability can be tested applying it to further reactions or new data. Here, one has to distinguish between the description of the energy dependence of the data and the prediction of the absolute values. Therefore, the agreement between prediction and data cannot be measured by a single value. *E.g.*, a χ^2 test provides a measure for the agreement on an absolute scale but neglects whether the energy dependence is correctly described.

The selection of the data sets included to the fitting procedure and the adjustment of the theoretical prediction based on its comparison to experimental data, respectively, rely on the sensitivity of the chosen reaction to the nuclear physics input of the prediction. A measure for the sensitivity S is described in [44]:

$$S = \begin{cases} \frac{f_\sigma - 1}{f_T - 1} & , \text{if } f_\sigma < 0, f_T < 0 \text{ or } f_\sigma > 0, f_T > 0 \\ \frac{1 - f_\sigma}{(f_T - 1)f_\sigma} & , \text{if } f_\sigma < 0, f_T > 0 \text{ or } f_\sigma > 0, f_T < 0 \end{cases} \quad (5.1)$$

Here, f_T is the ratio of the modified transmission coefficient T' and the original transmission coefficient T : $f_T = T'/T$. Accordingly, f_σ describes the ratio of the corresponding cross sections: $f_\sigma = \sigma'/\sigma$. The sensitivity S ranges from $S = 0$ to $S = 1$ with $S = 0$ indicating that a change of the transmission coefficient T has no influence on the cross section σ and $S = 1$ showing that the cross section σ changes by the same factor as the transmission coefficient T .

To derive a parameterization of the OMP at astrophysically relevant energies, only those reactions should be taken into account for which the sensitivities on all nuclear physics inputs are similar in the energy region accessible by experiment. The easiest way to achieve this situation is to investigate a reaction for which only one OMP enters the calculation as in the case of elastic scattering. However, there are two drawbacks for this approach. Firstly, the scattering cross sections have to be determined from spectra that are vastly dominated by Rutherford scattering (see, *e.g.*, [116, 117, 118, 119]). Thus, a very high angular resolution is mandatory. Secondly, the fit of an OMP to scattering data is not unambiguous since the same behaviour can be achieved by the variation of different parameters (compare Sec. 3.1). This is known as the family problem and was discussed in [63]. Furthermore, the OMPs derived using elastic scattering data like the widely used McFadden& Satchler OMP [50] overestimate the cross sections in the low-energy region (see, *e.g.*, [119] and references therein). As discussed in [115], this

might stem from the fact that elastic scattering probes the interaction with the surface of a nucleus while nuclear reactions include all nucleons.

Now, one might think that radiative-capture reactions are a good choice to determine the parameterization for an OMP as their study was so useful if information about the inverse reaction was needed for p -process nucleosynthesis (see Sec. 5.1). But the investigation of this type of reactions is limited in energy range due to the enormously fast decreasing cross sections once the energy is below the Coulomb barrier. Unfortunately, the sensitivity of the cross section to the different transition coefficients is generally different in the energy range which is accessible to experiments compared to the Gamow window for p -process nucleosynthesis. An example for the reaction $^{168}\text{Yb}(\alpha,\gamma)$ is shown in Fig. 5.2 where the dominating sensitivity in the Gamow window stems from the α width, *i.e.*, the transmission coefficient calculated from the α -nucleus OMP, while the neutron width as well as the γ width significantly contribute in the measured energy range. Thus, an adjustment using a combination of the three widths leads to a good description of the measured results. However, this combination is not necessarily unique and, in addition, the optimized α -nucleus OMP is not necessarily a good description in the Gamow window [82].

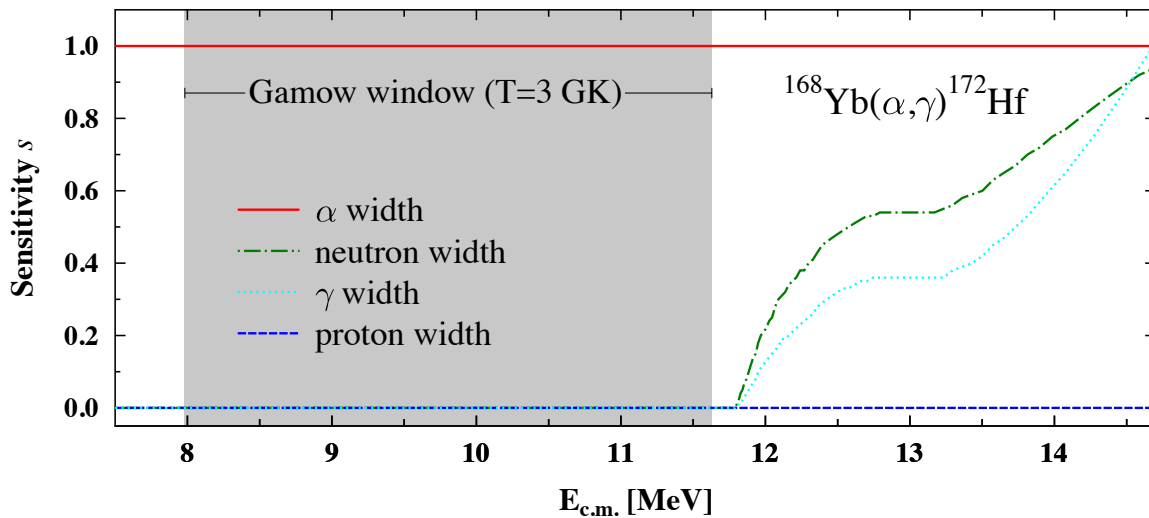


Figure 5.2:

Sensitivities s of the laboratory cross section of the $^{168}\text{Yb}(\alpha,\gamma)$ reaction. The α , neutron, γ , and proton width, *i.e.*, the corresponding transmission coefficients in Eq. (5.1), are separately varied by a factor of two. The absolute value of s is shown - the variation of the neutron width actually yields negative values as the threshold for the $^{168}\text{Yb}(\alpha,n)$ reaction is reached at $E_{\text{c.m.}} \approx 11.8$ MeV. The astrophysically relevant energy range for $T = 3.0$ GK is marked by the shaded area. Taken from [45].

To determine an OMP, it is necessary to find a reaction showing a similar sensitivity in the experimentally accessible energy range as the reaction of astrophysical interest

exhibits in the Gamow window. Recently, charged-particle induced reactions with neutrons as reaction ejectiles were found to be an appropriate tool since they generally show only a small sensitivity to the neutron OMP but are dominated by the charged-particle OMP in the measurable energy range (see, *e.g.*, [119, 89, 120, 80]). This approach to study (α, n) and (p, n) reactions for the determination of α -nucleus and proton-nucleus OMPs can be interpreted as an indirect method to determine the cross sections of (γ, α) and (γ, p) reactions, respectively.

The study of (α, n) reactions

The study of (α, n) reactions to determine α -nucleus OMPs became recently a widely used tool to overcome the lack of experimental data in the relevant energy range for p -process nucleosynthesis (see, *e.g.*, [119, 89, 120, 80]). In general, the study of (α, γ) reactions is only possible near the high-energy end of the Gamow window due to the fastly decreasing reaction cross sections and is usually performed using the activation approach as the beam-induced background hinders the analysis of in-beam γ -ray spectroscopy. Therefore, the number of (α, γ) reactions on p nuclei being explorable is still limited by the need of an unstable reaction product (compare Sec. 4.1). However, the corresponding (α, n) reaction leads in many cases to an unstable isotope, thus, they are accessible with the activation technique. As a typical example, the experiments performed and analyzed in [80] will be explained in detail in the following.

At first, the basic principles of the data analysis of an activation experiment are explained. To determine the number of reactions from the measured decays, several steps of analysis are necessary (for the definition of the variables, compare Fig. 5.3). The number of measured decays N_{meas} is proportional to the number of decays N_{dec} that really occurred during the measurement time $\tau_{\text{meas}} = t_{\text{meas}} - t_{\text{wait}}$:

$$N_{\text{meas}} \propto N_{\text{dec}} = N_{\text{start}} - N_{\text{stop}} = N_{\text{start}} \cdot (1 - \exp(-\lambda \cdot \tau_{\text{meas}})) \quad (5.2)$$

The factor of proportionality generally includes the detection efficiency ε , a correction for possible dead-times of the detection system $f_{\text{dead}} = t_{\text{life}}/t_{\text{real}}$, and a normalization of the observed signal to the number of decays which is the γ -ray intensity I_{γ} in case of using a γ -decay pattern:

$$f = \varepsilon \cdot f_{\text{dead}} \cdot I_{\gamma} \quad (5.3)$$

To calculate the amount of produced nuclei remaining after the activation N_{rem} , the decay law can be applied directly:

$$N_{\text{start}} = N_{\text{rem}} \cdot \exp(-\lambda \cdot \tau_{\text{wait}}), \quad \tau_{\text{wait}} = t_{\text{wait}} - t_{\text{act}} \quad (5.4)$$

The number of produced nuclei which is equal to the number of reactions amounts to:

$$N_{\text{rem}} = \frac{N_{\text{prod}}}{\lambda \cdot \tau_{\text{act}}} (1 - \exp(-\lambda \cdot \tau_{\text{act}})), \quad \tau_{\text{act}} = t_{\text{act}} \quad (5.5)$$

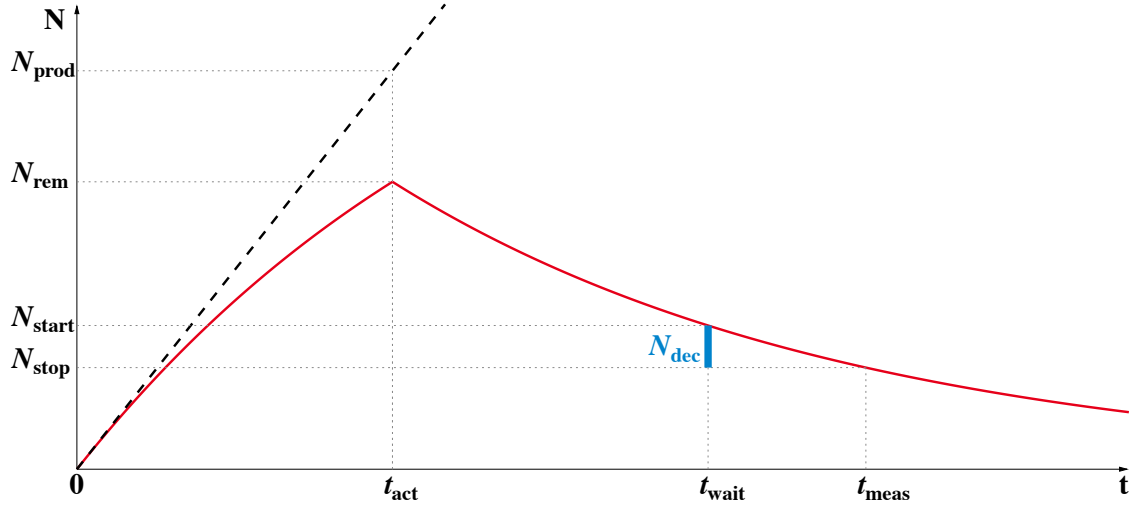


Figure 5.3:

Number of reaction products as function of time. During the duration of the activation $\tau_{\text{act}} = t_{\text{act}}$, a number of N_{prod} reaction products are produced. Due to their radioactive decay, only an amount of N_{rem} nuclei remains after the activation. During the time between activation and determination of the reaction yield $\tau_{\text{wait}} = t_{\text{wait}} - t_{\text{act}}$, this amount is further reduced to N_{start} . If the determination takes a measurement time of $\tau_{\text{meas}} = t_{\text{meas}} - t_{\text{wait}}$ a number of $N_{\text{dec}} = N_{\text{start}} - N_{\text{stop}}$ nuclei is decaying.

if the production rate β is constant during the activation and, thus, simply yields the number of produced nuclei by $N_{\text{prod}} = \beta \cdot \tau_{\text{act}}$.

In case of a varying production rate, *e.g.*, due to changes of the beam intensity or to losses of target material, it is mandatory to monitor it as a function of time and take this data into account to replace Eq. (5.5) with

$$N_{\text{rem}} = \frac{1 - \exp(-\lambda \Delta t)}{\lambda} \cdot \sum_{k=1}^M \beta_k \cdot \exp(-\lambda(M - k)\Delta t). \quad (5.6)$$

The total duration of the activation τ_{act} is in this case divided into M intervals of duration Δt . The time intervals Δt are chosen such that the corresponding production rates β_k are constant.

In total, the number of reactions can be derived from the measured decays using

$$N_{\text{prod}} = (f_{\text{act}} \cdot f_{\text{wait}} \cdot f_{\text{meas}} \cdot f)^{-1} \cdot N_{\text{meas}} \quad (5.7)$$

with the correction factors $f_{\text{act}} = 1 - \exp(-\lambda \tau_{\text{act}})/(\lambda \tau_{\text{act}})$, $f_{\text{wait}} = \exp(-\lambda \tau_{\text{wait}})$, and $f_{\text{meas}} = 1 - \exp(-\lambda \tau_{\text{meas}})$ from Eqs. (5.5), (5.4), and (5.2), respectively. In case of a varying production rate, Eq. (5.6) has to be used instead of f_{act} .

The $^{165}\text{Ho}(\alpha,n)$ and $^{166}\text{Er}(\alpha,n)$ reactions were investigated with the activation approach at the Institute for Structure and Nuclear Astrophysics, University of Notre Dame, Indiana, U.S.A. and the data was analyzed as described above. Figure 5.4 shows the sensitivities of the (α,γ) and (α,n) reactions for the Gamow window and the studied energy range, respectively. In both cases and for both isotopes ^{165}Ho and ^{166}Er , the dominant effect is induced by the α -particle OMP. The (α,n) reactions were studied at nine and eight energies E_{lab} , respectively, using naturally composed targets with areal densities between $700 \mu\text{g}/\text{cm}^2$ and $900 \mu\text{g}/\text{cm}^2$ (compare Tab. 5.1).

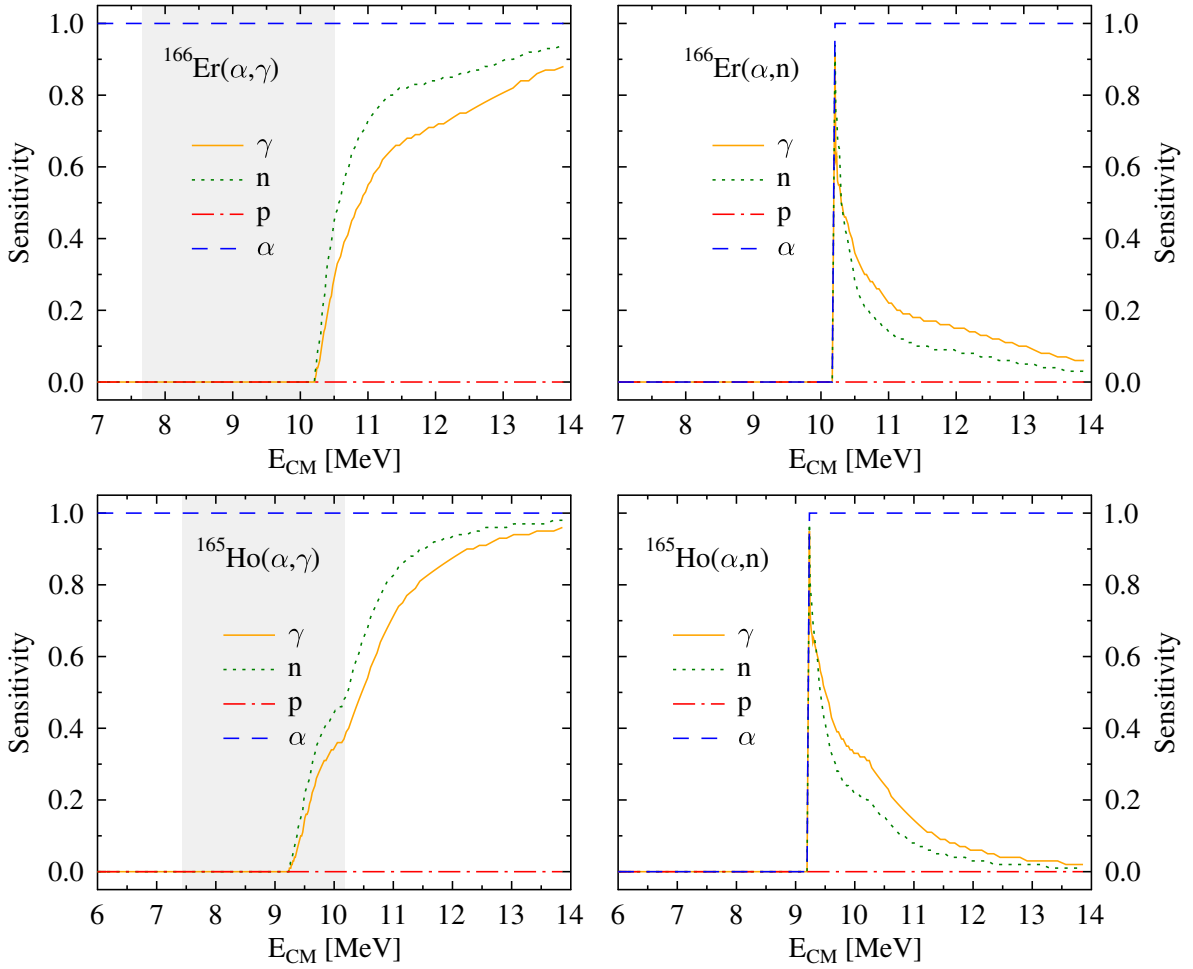


Figure 5.4:

Sensitivities s of the laboratory cross sections of the reactions $^{166}\text{Er}(\alpha,\gamma)$, $^{166}\text{Er}(\alpha,n)$, $^{165}\text{Ho}(\alpha,\gamma)$, and $^{165}\text{Ho}(\alpha,n)$ [114]. The depiction is similar to Fig. 5.2. For the (α,γ) reactions, the sensitivities in the Gamow window and the experimentally investigated energy range differ drastically while the (α,n) reactions show a nearly exclusive sensitivity to the α width. Taken from [15].

Table 5.1:

Characteristics of the holmium and erbium targets used for the study of the reactions $^{165}\text{Ho}(\alpha, n)$ and $^{166}\text{Er}(\alpha, n)$. The identification number (ID) of the targets is listed with the corresponding areal densities derived from the mass and area of the targets (d_{ORNL}) and RBS measurements (d_{target}), respectively, and activation energies E_{α} .

target ID	d_{ORNL} [$\mu\text{g}/\text{cm}^2$]	d_{target} [$\mu\text{g}/\text{cm}^2$]	E_{α} [MeV]	target ID	d_{ORNL} [$\mu\text{g}/\text{cm}^2$]	d_{target} [$\mu\text{g}/\text{cm}^2$]	E_{α} [MeV]
Er-05	806	860±42	11.40	Ho-10	823	861±44	11.01
Er-01	885	828±42	11.75	Ho-11	888	879±45	11.39
Er-13	841	827±42	12.12	Ho-08	876	834±43	11.77
Er-03	840	783±40	12.50	Ho-07	769	777±40	12.30
Er-12	837	865±44	13.00	Ho-06	798	700±36	12.80
Er-10	831	858±44	13.50	Ho-05	740	792±40	13.33
Er-07	807	755±39	14.00	Ho-04	824	798±41	13.83
Er-06	774	823±39	14.85	Ho-03	708	797±41	14.35
Er-04	772	787±40	15.00	Ho-02	825	772±39	14.85
				Ho-12	825	895±46	14.85
				Ho-01	738	741±38	15.35

The energy loss of the projectiles was taken into account by the introduction of an effective energy E_{eff} which was iteratively determined using the constraint

$$\int_{E_{\text{CM}} - \Delta E_{\text{target}}}^{E_{\text{eff}}} \sigma(E) dE = \int_{E_{\text{eff}}}^{E_{\text{CM}}} \sigma(E) dE \quad (5.8)$$

where E_{CM} is the energy available in the centre-of-mass system and ΔE_{target} is the total energy loss in the target foils calculated with the stopping power $S_M(E)$:

$$d_{\text{target}} = \int_{E_{\text{lab}} - \Delta E_{\text{target}}}^{E_{\text{lab}}} \frac{1}{S_M(E)} dE. \quad (5.9)$$

After the irradiation, the activity of the samples was determined by γ -ray spectroscopy in a very close geometry to allow the measurement of very small activities as yielded for the lowest activation energies E_{lab} . Due to the complicated decay schemes of the reaction products ^{168}Tm and ^{169}Yb , respectively, summing effects were corrected for using reference targets which were activated at higher energies E_{lab} . A comparison of the activity determined from a measurement in the very close geometry and a measurement without summing effects yielded a normalization factor for the given decay pattern. Sample spectra are shown in Fig. 5.5.

The experimentally determined cross sections are listed in Tab. 5.2 for both reactions. Using these values, a comparison with calculations based on different α -particle OMPs

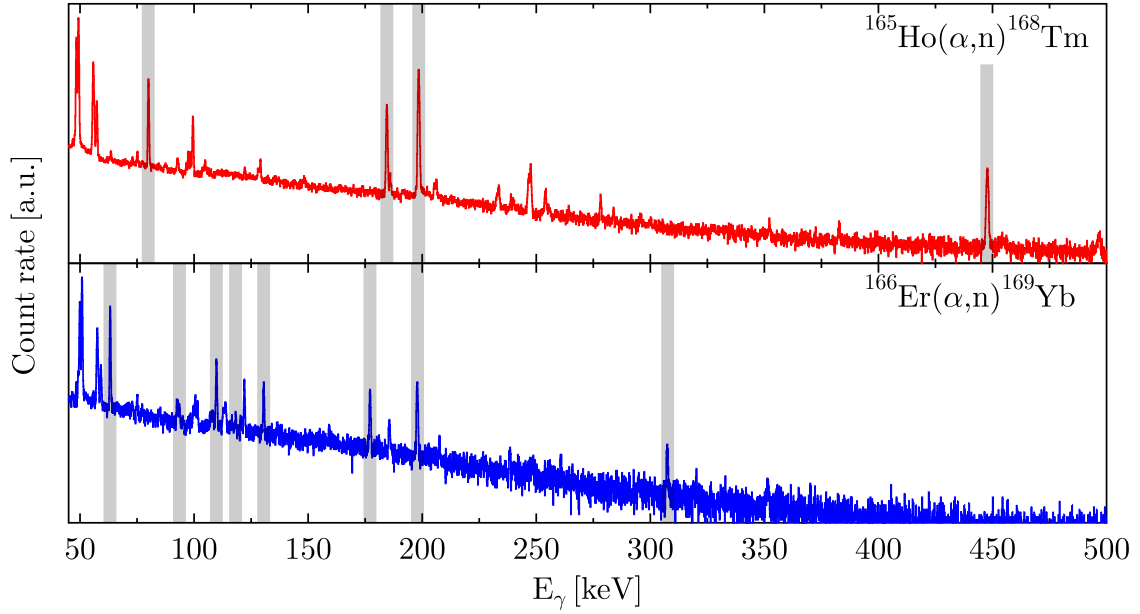


Figure 5.5:

Spectra measured after the activation of naturally composed holmium and erbium targets with α particles. The γ rays emitted after the β decays of the produced unstable isotopes are measured. The transitions corresponding to the decay of ^{168}Tm and ^{169}Yb , the product nuclei of the reactions $^{165}\text{Ho}(\alpha, n)$ and $^{166}\text{Er}(\alpha, n)$, respectively, are marked with grey-shaded areas.

and different γ -ray strength functions was performed. The results are summarized in Fig. 5.6 in terms of S factors as function of effective energies E_{eff} . As concluded in [80], the deviations between prediction and experiment can also be assigned to other transmission coefficients. However, the presented solution for the α -nucleus OMP was also valid for other α -particle induced reactions in that mass region (compare, *e.g.*, [120, 119, 89]). Therefore, the idea of introducing an energy-dependent term in the imaginary part of the α -nucleus OMP can be an important step towards a global description to be used for predictions of cross sections of α -particle induced reactions relevant for the nucleosynthesis of p nuclei.

The study of (p,n) reactions

The lack of experimental data on proton-induced reactions in the energy range relevant for the nucleosynthesis of p nuclei is not as severe as in the case of α -particle induced reactions (compare Fig. 5.1). In general, the lower Coulomb barrier allows to access this energy range also for (p, γ) reactions, therefore, the ground-state cross section is accessible experimentally. However, the determination of the stellar reaction rate still

Table 5.2:

Cross sections of the reactions $^{166}\text{Er}(\alpha, n)$ and $^{165}\text{Ho}(\alpha, n)$ for activation energies E_α and effective energies E_{eff} , respectively.

$^{166}\text{Er}(\alpha, n)$			$^{165}\text{Ho}(\alpha, n)$		
E_α [MeV]	E_{eff} [MeV]	σ [mb]	E_α [MeV]	E_{eff} [MeV]	σ [mb]
11.40	$11.066^{+0.065}_{-0.082}$	$3.24(29)\cdot 10^{-4}$	11.01	$10.677^{+0.067}_{-0.085}$	$2.66(50)\cdot 10^{-4}$
11.75	$11.411^{+0.062}_{-0.077}$	$1.25(41)\cdot 10^{-3}$	11.39	$11.055^{+0.067}_{-0.085}$	$8.20(117)\cdot 10^{-3}$
12.12	$11.777^{+0.062}_{-0.075}$	$2.96(46)\cdot 10^{-3}$	11.77	$11.431^{+0.064}_{-0.078}$	$2.43(29)\cdot 10^{-3}$
12.50	$12.148^{+0.058}_{-0.068}$	$9.54(61)\cdot 10^{-3}$	12.30	$11.952^{+0.059}_{-0.070}$	$9.68(70)\cdot 10^{-3}$
13.00	$12.631^{+0.063}_{-0.074}$	$3.23(24)\cdot 10^{-2}$	12.80	$12.446^{+0.053}_{-0.060}$	$3.57(23)\cdot 10^{-2}$
13.50	$13.121^{+0.061}_{-0.072}$	$9.97(57)\cdot 10^{-2}$	13.33	$12.954^{+0.058}_{-0.067}$	$1.16(7)\cdot 10^{-1}$
14.00	$13.616^{+0.054}_{-0.061}$	$2.91(16)\cdot 10^{-1}$	13.83	$13.438^{+0.058}_{-0.065}$	$3.31(20)\cdot 10^{-1}$
14.85	$14.439^{+0.057}_{-0.063}$	1.57(8)	14.35	$13.956^{+0.057}_{-0.063}$	$8.87(52)\cdot 10^{-1}$
15.00	$14.593^{+0.054}_{-0.060}$	1.87(10)	14.85	$14.432^{+0.062}_{-0.070}$	2.32(17)
				$14.442^{+0.054}_{-0.060}$	2.18(14)
			15.35	$14.936^{+0.051}_{-0.056}$	4.92(29)

relies on theoretical modelling as the contribution of populated excited states has to be calculated. In addition, some of the (p, γ) reactions being important for the final abundance pattern produced within the γ process (see Tab. 6.1) are not measurable without a radioactive beam due to the instability of the target and product isotope, respectively.

The determination of a proton-nucleus OMP which is reliable across the whole mass range covered by γ process nucleosynthesis is therefore also mandatory to avoid uncertainties based on nuclear physics. As in the case of α -particle induced reactions, the study of (p,n) reactions is a useful tool as they usually show sensitivity to the proton-nucleus OMP only. To check for a possible influence of unpaired protons to the general description of the proton-nucleus OMP, the (p,n) reactions on ^{169}Tm ($Z = 69$) and on ^{175}Lu ($Z = 71$) are investigated.

The experiments were performed using the activation technique at the Institute for Structure and Nuclear Astrophysics, University of Notre Dame, Indiana, U.S.A. The targets were of natural composition with areal densities between $1850 \mu\text{g}/\text{cm}^2$ and $2500 \mu\text{g}/\text{cm}^2$ (compare Tab. 5.3). This translates to a similar energy loss as in the case of the erbium and holmium targets described in the previous paragraph. Therefore, a similar uncertainty of the activation energy is taken into account by the introduction of an effective energy as described in Eq. (5.8).

The number of reactions was determined using γ -ray spectroscopy in a very close geometry to allow the measurement of very small activities. The summing effects occurring in the spectra were corrected in the same way as described in the previous paragraph. In

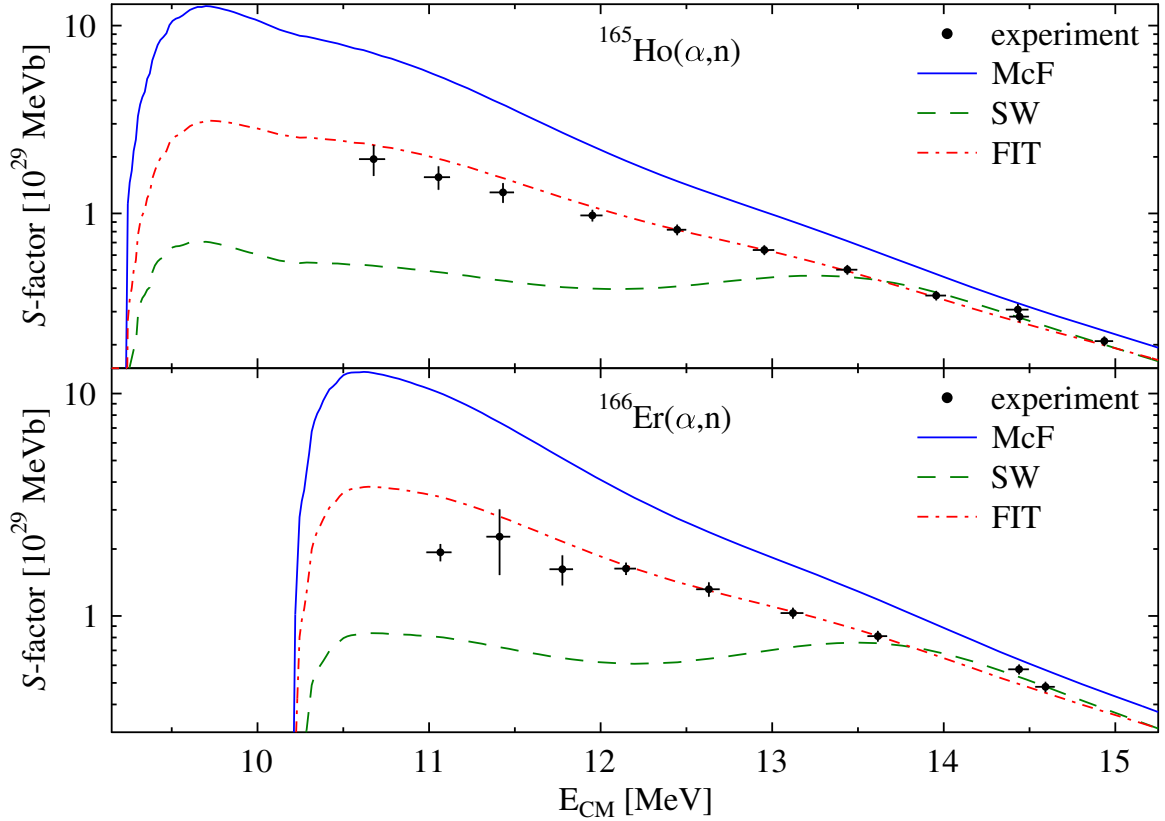


Figure 5.6:

Experimental S factors of the reactions $^{165}\text{Ho}(\alpha, n)$ and $^{166}\text{Er}(\alpha, n)$ compared to theory. The Hauser-Feshbach code SMARAGD is used with different α -particle OMPs: McFadden& Satchler [50] (blue), Sauerwein-Rauscher [120] (green), and adjusted Sauerwein-Rauscher (red) potentials, respectively. The free parameter of the Sauerwein-Rauscher potential, the smoothing factor of the Fermi function is adjusted to $a = 5$ MeV in agreement with [119]. Taken from [15].

case of the $^{166}\text{Er}(\alpha, n)$ and $^{169}\text{Tm}(p, n)$ reaction, the reaction product is ^{169}Yb . Thus, the observed summing effects are identical and can be determined with either of the targets. The experimentally determined cross sections are listed in Tab. 5.4 for both reactions. In case of the $^{169}\text{Tm}(p, n)$ reaction, experimental data is available in a similar energy range [121, 122]. The energy resolution of these measurements is worse as very thick target material was used, and their results do not agree on an absolute scale hinting to a systematic deviation in the absolute determination of the proton energies. The results of this work agree with those of [122] in the overlapping energy range. However, they were not used to extend the energy range for comparison with theoretical predictions as the worse energy resolution does not allow to do so.

The available data is compared to calculations based on different proton-nucleus OMPs in Fig. 5.7. Globally determined OMPs like the ones derived by Jeukenne, Lejeune, and

Table 5.3:

Characteristics of the thulium and lutetium targets used for the study of the reactions $^{169}\text{Tm}(p,n)$ and $^{175}\text{Lu}(p,n)$. The identification number (ID) of the targets is listed with the corresponding areal densities d_{ORNL} and d_{target} , respectively, and activation energies E_p (compare Tab. 5.1).

target ID	d_{ORNL} [$\mu\text{g}/\text{cm}^2$]	d_{target} [$\mu\text{g}/\text{cm}^2$]	E_p [MeV]	target ID	d_{ORNL} [$\mu\text{g}/\text{cm}^2$]	d_{target} [$\mu\text{g}/\text{cm}^2$]	E_p [MeV]
Tm-11	2.06	2.04 ± 0.12	3.30	Lu-02	2.50	2.38 ± 0.12	3.50
Tm-08	2.09	2.04 ± 0.12	3.70	Lu-03	2.56	2.49 ± 0.13	3.99
Tm-12	1.95	1.93 ± 0.11	4.00	Lu-04	2.56	2.37 ± 0.12	4.49
Tm-07	1.95	1.85 ± 0.11	4.50	Lu-05	2.50	2.29 ± 0.12	5.00
Tm-05	1.91	1.96 ± 0.11	5.00	Lu-06	2.50	2.38 ± 0.12	5.50
Tm-09	1.90	1.88 ± 0.11	5.50	Lu-07	2.56	2.42 ± 0.12	6.00
Tm-02	1.90	—	6.20	Lu-08	2.50	2.52 ± 0.13	6.50
Tm-06	1.82	—	7.00	Lu-01	2.40	2.16 ± 0.11	7.00

Table 5.4:

Cross sections of the reactions $^{169}\text{Tm}(p,n)$ and $^{175}\text{Lu}(p,n)$ for activation energies E_p and effective energies E_{eff} , respectively.

$^{169}\text{Tm}(p,n)$			$^{175}\text{Lu}(p,n)$		
E_p [MeV]	E_{eff} [MeV]	σ [mb]	E_p [MeV]	E_{eff} [MeV]	σ [mb]
3.30	$3.244^{+0.036}_{-0.043}$	$9.70(78) \cdot 10^{-4}$	3.50	$3.439^{+0.040}_{-0.048}$	$1.58(13) \cdot 10^{-3}$
3.70	$3.644^{+0.034}_{-0.040}$	$6.04(35) \cdot 10^{-3}$	3.99	$3.936^{+0.039}_{-0.046}$	$1.31(11) \cdot 10^{-2}$
4.00	$3.945^{+0.031}_{-0.036}$	$2.23(14) \cdot 10^{-2}$	4.49	$4.424^{+0.035}_{-0.040}$	$7.91(64) \cdot 10^{-2}$
4.50	$4.444^{+0.029}_{-0.031}$	$1.26(8) \cdot 10^{-1}$	5.00	$4.938^{+0.033}_{-0.036}$	$3.65(27) \cdot 10^{-1}$
5.00	$4.942^{+0.028}_{-0.031}$	$5.13(31) \cdot 10^{-1}$	5.50	$5.436^{+0.032}_{-0.035}$	1.22(10)
5.50	$5.441^{+0.026}_{-0.028}$	1.67(10)	6.00	$5.937^{+0.031}_{-0.033}$	3.42(25)
6.20	$6.139^{+0.024}_{-0.025}$	6.78(37)	6.50	$6.432^{+0.031}_{-0.032}$	8.31(58)
7.00	$6.936^{+0.022}_{-0.022}$	$2.33(12) \cdot 10^{+1}$	7.00	$6.934^{+0.026}_{-0.026}$	$1.84(14) \cdot 10^{+1}$

Mahaux (JLM) [47] and by Bauge, Delaroche, and Girod (BDG) [123] cannot reproduce the measured energy dependency. This situation drastically changes if the isovector component of the OMP by JLM is enlarged in order to enhance the imaginary part. Although the measured data is still underestimated by a factor of 1.6, the energy dependence is almost perfectly reproduced.

To introduce this modification to the OMP by JLM as a standard component, it is mandatory to study its dependency on nuclear properties such as mass or charge number. If systematic studies reveal and confirm such dependencies in the future, the result would

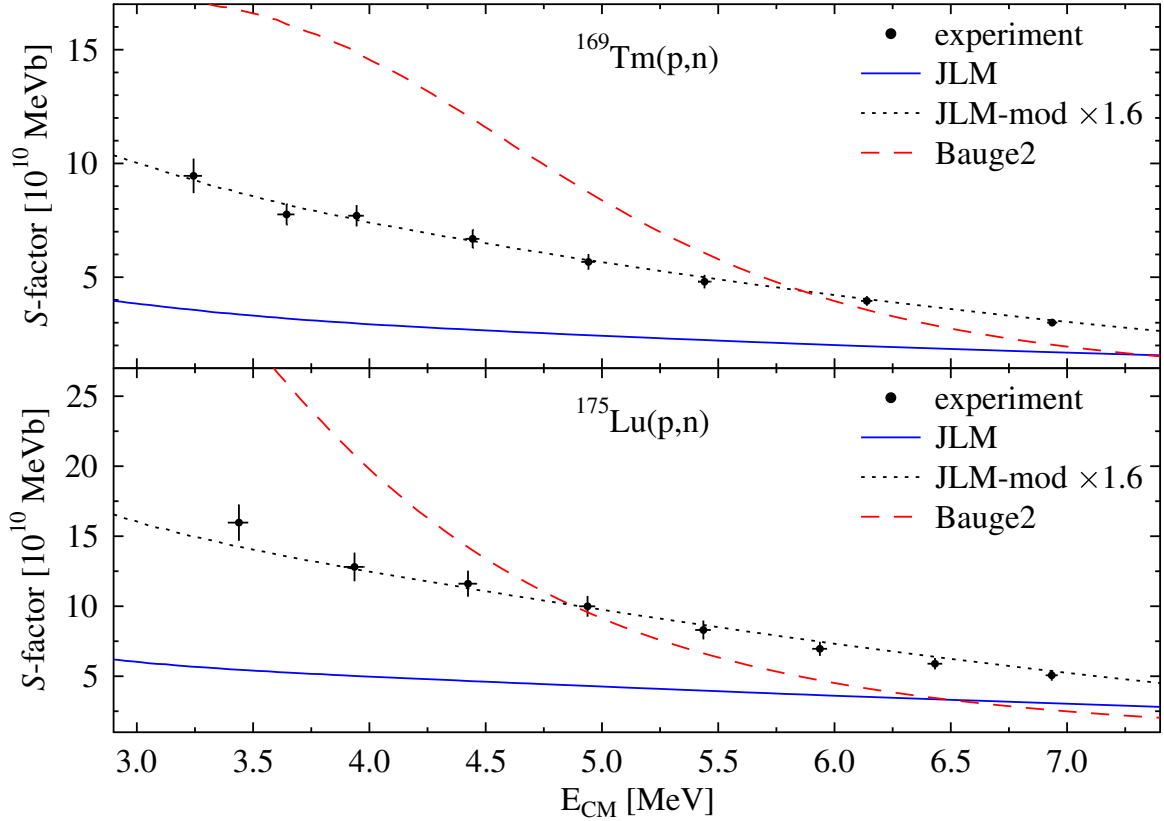


Figure 5.7:

Experimental S factors of the reactions $^{169}\text{Tm}(p,n)$ and $^{175}\text{Lu}(p,n)$ compared to theory. The Hauser-Feshbach code SMARAGD is used with different proton OMPs: JLM [47] (blue), Bauge [123] (red), and modified JLM [124] (black) potentials, respectively. The energy dependence is almost perfectly reproduced by the modified JLM potential. For an absolute adjustment, a factor of 1.6 must be applied [15].

be a microscopic proton-nucleus OMP with a correction for low-energy absorption being globally applicable.

5.1.2 Proton-capture reactions on light nuclei

As mentioned in Sec. 2, the production of the lightest p nuclei up to molybdenum was recently shown to be realised by successive radiative proton-capture reactions at least in a measurable amount [19, 20]. The underlying mechanism and the studies performed in a post-processing network will be explained in detail in Sec. 6.2. As expected from such small reaction chains, the produced abundances become sensitive to selected reaction rates in contrast to the γ process as described in Sec. 5.1.1. In addition, the target nuclei are close to stability or stable. Thus, a complete experimental investigation of the involved reactions becomes possible.

Figure 5.8 shows the reactions involved for the production (and destruction) of ^{74}Se , ^{80}Kr , ^{84}Sr , and ^{92}Mo . The isotope ^{92}Mo is the most abundant p nucleus with an isotopic abundance of $I_{\%} = 14.84\%$ (compare Tab. 2.1). It has one of the smallest overproduction factors in the γ process [17] (compare Fig. 2.6). A chain of radiative proton-capture reactions on the stable neutron-magic $N = 50$ nuclei might be an additional production mechanism as proposed in [19, 20] for type Ia supernovae. Due to the increasing Coulomb barrier, the proton-capture cross sections on ^{90}Zr and ^{91}Nb decrease compared to the other neutron-magic isotopes with $N = 50$. Thus, the corresponding reaction rates determine how much ^{92}Mo can be produced in the explosive scenario of a type Ia supernova.

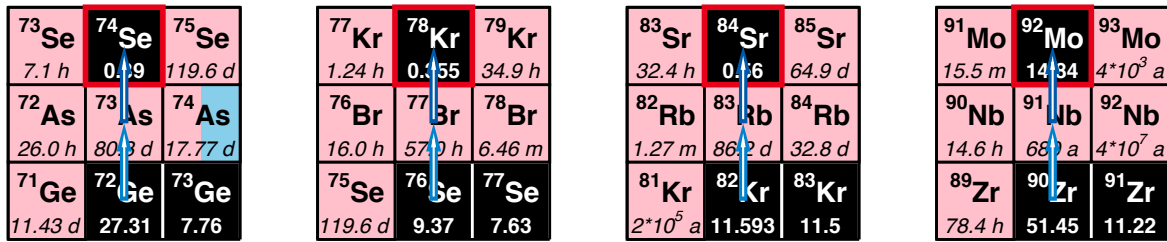


Figure 5.8:

Radiative proton-capture reactions producing the lightest p nuclei. As investigated in [19, 20], the lightest p nuclei are also produced by chains of radiative proton-capture reactions in a type Ia supernova. These reactions are shown in the corresponding extract of the nuclidic chart.

As an unstable isotope, ^{91}Nb is not available in the seed distribution. Thus, every ^{91}Nb nucleus has to be produced before it can capture a proton to become ^{92}Mo . Therefore, the cross sections of the $^{90}\text{Zr}(p,\gamma)$ and $^{91}\text{Nb}(p,\gamma)$ reactions are the most important ones to understand the production of ^{92}Mo in this scenario. Besides the production of ^{92}Mo via radiative proton-capture reactions, its destruction by the same reaction type has to be taken into account, too. However, the produced ^{92}Mo will not be destroyed directly because of the low rate of the $^{92}\text{Mo}(p,\gamma)$ reaction which was recently experimentally confirmed by [81].

In case the reactions leading to the production of ^{92}Mo are strongly influenced by the astrophysical environment, its observed abundance can be used as a benchmark test for the astrophysical conditions realized in different scenarios and nucleosynthesis network calculations. Then, it can be used as a tracer and provides an interesting look to the inside of, *e.g.*, a type Ia supernova.

Investigation of the reaction $^{90}\text{Zr}(p,\gamma)$ The $^{90}\text{Zr}(p,\gamma)$ reaction was recently studied by A. Spyrou and co-workers [125] to solve the unambiguity of the old data sets available in [126, 127]. A 4π summing detector was used to determine the reaction yield and total cross section via γ calorimetry. The results of [125] confirm those of [126] who used the

thick target yield method to determine the total cross section. Thus, the agreement of the two measurements as stated in [125] was not surprising. To exclude an influence of the level scheme, especially of an isomeric state in ^{91}Nb ($E_\gamma = 104$ keV, $t_{1/2} = 60.86$ d), we investigated the reaction using the same technique as in [127]: high-resolution in-beam γ -spectroscopy.

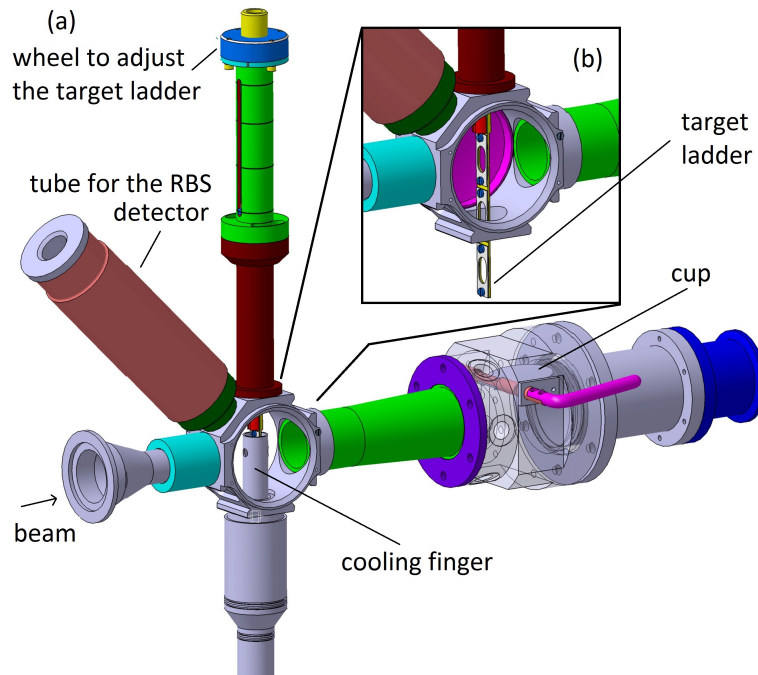


Figure 5.9:

Illustration of HORUS target chamber. (a) Overview. The target chamber is equipped with a cooling finger, a silicon detector for RBS measurements, and a removable cup closely behind the target. (b) Interior view of target chamber. A coating with tantalum prevents from background due to reactions on the aluminum housing. Taken from [45].

We used HORUS at University of Cologne, Germany, with a target chamber optimized for measurements of radiative particle-induced reactions in the astrophysically relevant energy range [98]. Thirteen high-purity Germanium (HPGe) detectors are placed at five different angles with respect to the incoming beam to determine the angular dependency of the prompt γ rays in order to extract the total cross section (compare Fig. 5.9). The observation of the depopulation of the so-called entry-state (marked with γ_i in Fig. 5.10) yields the partial cross sections (p, γ_i) [99]. Their sum equals the total cross section. However, the experimental determination of all corresponding transitions is usually hampered by a lack of knowledge of the complete level scheme up to the energy of the entry-state.

Therefore, the total cross section is usually determined from the transitions of excited

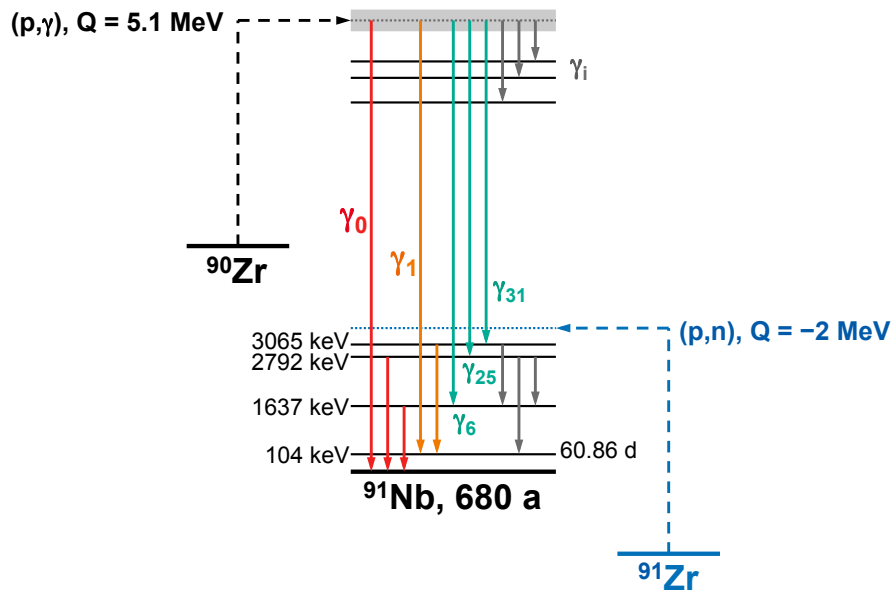


Figure 5.10:

Scheme of prompt γ transitions of the $^{90}\text{Zr}(p,\gamma)$ reaction (not all levels shown). The γ transitions depopulating the entry state (grey band) are marked with γ_i and correspond to the partial cross sections (p,γ_i) . In order to determine the total cross section, all γ transitions ending in the ground state (red) and the isomeric state (yellow) are analyzed and their contributions are added. Contributions stemming from the $^{91}\text{Zr}(p,n)$ reaction populating low-energy excited states in ^{91}Nb further complicate the analysis. Data from [128].

levels to the ground state (marked in red in Fig. 5.10) which collect the contributions of all possible cascades from the entry state. Since there is an isomeric state in ^{91}Nb which serves also as an end point of cascades (transitions marked in yellow in Fig. 5.10) the contributions to the ground state and the isomeric state must be added in this special case to derive the total cross section.

For the targets, we used isotopically enriched material consisting of 97.65% ^{90}Zr and, besides other Zirconium isotopes, 0.96% ^{91}Zr . As indicated in Fig. 5.10, the $^{91}\text{Zr}(p,n)$ reaction feeds the same γ transitions as the $^{90}\text{Zr}(p,\gamma)$ reaction to be investigated up to a certain energy. Therefore, we also prepared targets consisting of 89.20% ^{91}Zr and 5.99% ^{90}Zr and performed measurements with both targets for each energy. This will allow us to disentangle the contribution of both reactions from the observed reaction yields and, thus, determine the total cross sections separately. The targets were prepared as self-supporting foils with thicknesses of about $530 \mu\text{g}/\text{cm}^2$. To stop the proton beam in the target chamber, they were placed with a gold foil in the target ladder. Since the protons were stopped in the gold foil, the corresponding contributions in the spectra are

determined using additional measurements with the target ladder being rotated by 180° , thus, the proton beam directly impinged the gold foils [100].

An exemplary spectrum measured with a HPGe detector positioned at 90° with respect to the beam axis is shown in Fig. 5.11. The transitions corresponding to the depopulation of the entry-state are marked similar as in Fig. 5.10. In addition, a selection of the transitions needed for the determination of the total cross section are marked in red and orange, respectively.

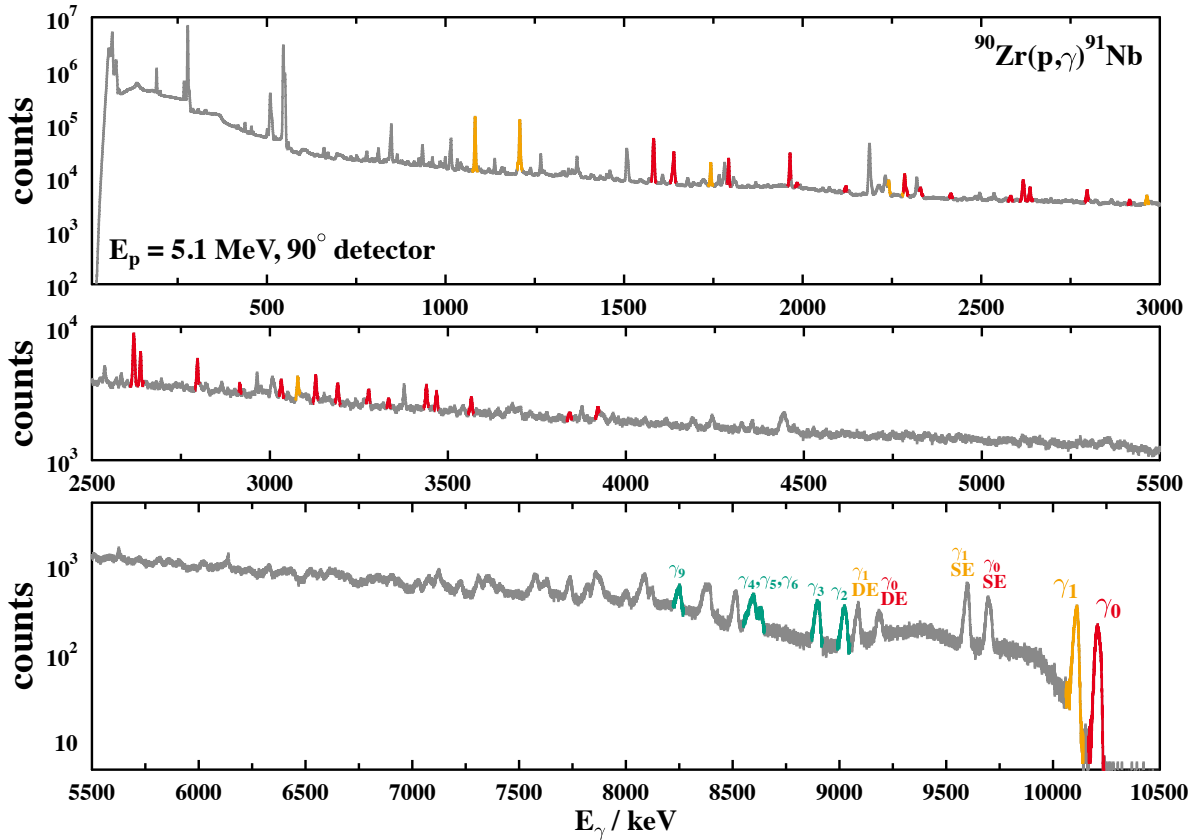


Figure 5.11:

Single spectrum of a HPGe detector placed at 90° with respect to the beam axis in HORUS. The γ transitions marked in red and yellow correspond to transitions to the ground state and isomeric state of ^{91}Nb , respectively, and determine the total cross section. The γ transitions labeled γ_i corresponds to the depopulation of the entry state in ^{91}Nb and determine the partial cross sections (compare Fig. 5.10).

As indicated in Sec. 4.2, the difficulty in the extraction of the cross section from the spectroscopic data is based on the angular distribution of the emitted prompt γ rays, *i.e.*, the γ yield at different angles ϑ with respect to the proton beam. The measured counts $N_{p\gamma+pn}^{j \rightarrow i}(\vartheta)$ for a transition from energy level j to energy level i in ^{91}Nb , containing

contributions from the reactions $^{90}\text{Zr}(p,\gamma)$ and $^{91}\text{Zr}(p,n)$ is given by

$$N_{p\gamma+pn}^{j\rightarrow i}(\vartheta) = (\sigma_{p\gamma}^{j\rightarrow i}(\vartheta)I_{p\gamma} + \sigma_{pn}^{j\rightarrow i}(\vartheta)I_{pn})\varepsilon_{\gamma}(E)m_{\text{T}}N_{\text{p}} \quad (5.10)$$

with the product of the cross section σ and the angular distribution $W(\vartheta)$ to $\sigma^{j\rightarrow i}(\vartheta) = \sigma^{j\rightarrow i}W^{j\rightarrow i}(\vartheta)$ as unknown variables, the relative isotopic abundances $I_{p\gamma}$ and I_{pn} of ^{90}Zr and ^{91}Zr , respectively, the detection efficiency ε for the energy E of the observed transition, the areal density m_{T} of the zirconium target, and the number of protons N_{p} impinging the target. The corresponding values for the γ transition of the seventh excited state in ^{91}Nb to its ground-state with energy $E_{\gamma} = 1790.62$ keV are shown for both zirconium targets in Fig. 5.12. The angular distribution varies greatly between both targets due to the different entry states of both reactions resulting from their different Q values.

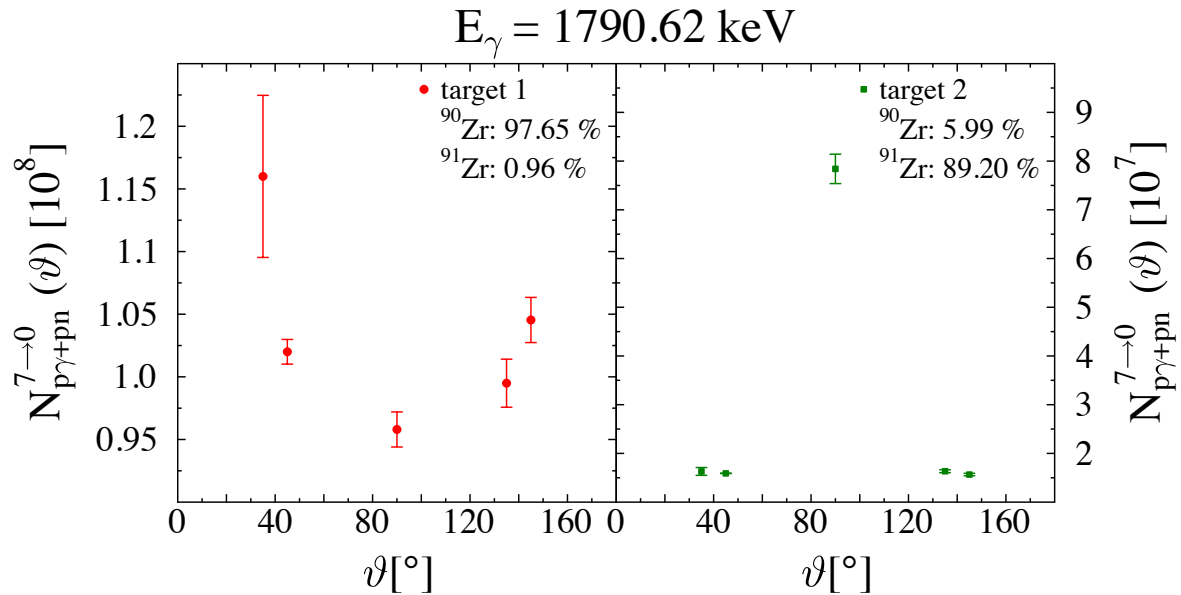


Figure 5.12:

Efficiency-corrected events for the investigation of the $^{90}\text{Zr}(p,\gamma)$ and $^{91}\text{Zr}(p,n)$ reaction. *left*: Angular distribution for target 1 enriched in ^{90}Zr . *right*: Angular distribution for target 2 enriched in ^{91}Zr . For details, see text. Taken from [129].

The unknown product $\sigma_{p\gamma}^{j\rightarrow i}(\vartheta)$ is derived from the data measured with the two zirconium targets 1 and 2 as characterized above using the equation

$$\sigma_{p\gamma}^{j\rightarrow i}(\vartheta) = \frac{N_{p\gamma+pn}^{j\rightarrow i,1}(\vartheta)}{\varepsilon_{\gamma}(E)m_{\text{T}}^1N_{\text{p}}^1} - \frac{N_{p\gamma+pn}^{j\rightarrow i,2}(\vartheta)}{\varepsilon_{\gamma}(E)m_{\text{T}}^2N_{\text{p}}^2} \cdot \frac{I_{\text{pn}}^1/I_{\text{pn}}^2}{I_{\text{p}\gamma}^1 - I_{\text{p}\gamma}^2 I_{\text{pn}}^1/I_{\text{pn}}^2}. \quad (5.11)$$

The integration of a sum of Legendre polynomials fitted to the data as shown in Fig. 5.13 for the transition of the seventh excited state in ^{91}Nb to its ground-state yields the cross section derived from the observed γ transition.

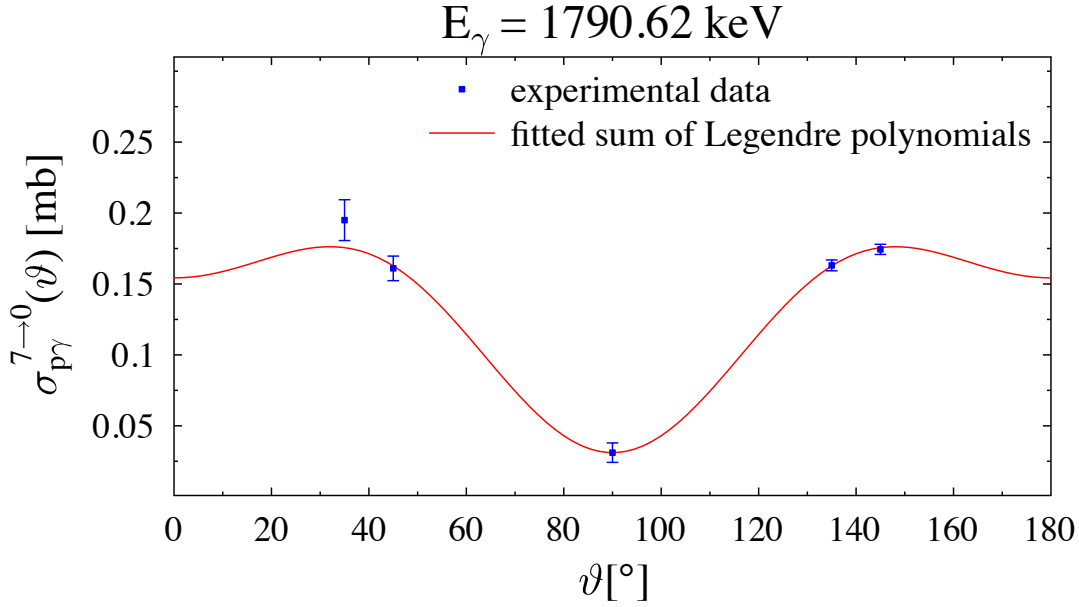


Figure 5.13:

Angular distribution of the contribution of the $^{90}\text{Zr}(p,\gamma)$ reaction to the γ transition from the seventh excited state of ^{91}Nb to its ground-state. The results of the data analysis (blue) according to Eqs. (5.10) and (5.10) is used to fit a sum of Legendre polynomials (red). For details, see text. Taken from [129].

Figure 5.14 shows preliminary results for the total cross section in comparison with the cross section data [127, 125]. The total cross sections published in [127] include estimated cross sections of the unobserved γ rays terminating in the ground or first excited state. Our experimental results agree with the data of [127] very well. The data by [125] yields higher cross sections, especially at higher energies. Furthermore, the experimental results are compared with theoretical cross section predictions by the TALYS code [46]. The cross section predictions are sensitive to the γ -ray strength function and the proton optical model potential. Hence, the cross section predictions were calculated with all variations for this nuclear physics input available in TALYS. Our experimental results agree very well with the theoretical predictions using the default settings of the TALYS code (compare Tab. 3.1).

Besides the total cross sections, we have analysed partial cross sections as well. Up to date, we have obtained partial cross sections for the transitions terminating in the ground state and three excited states. As an example, the partial cross section to the ground state is depicted in Fig. 5.15. It is compared to TALYS calculations using the default settings (compare Tab. 3.1). A remarkable agreement of both the energy dependence and the absolute values is found.

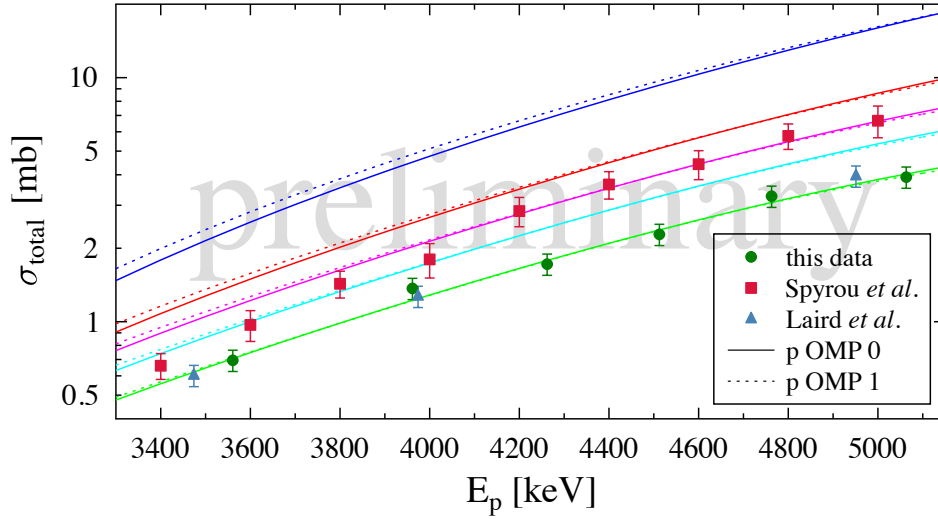


Figure 5.14:

Total cross section of the reaction $^{90}\text{Zr}(p,\gamma)$. The results of this work (green circles) are depicted with the results published in [127] (blue triangle) and in [125] (red squares), respectively. In addition, cross sections predicted using the TALYS code are shown. Different combinations of proton OMPs and γ -ray strength functions are used as input. Different line styles represent the used proton OMP: [49] solid and [123] dashed, respectively. Different line colors represent the used γ -ray strength function: [69] lightgreen, [52, 53] blue, [68] cyan, [69] magenta, and [130] red. For details, see text. Taken from [131].

Investigation of the reaction $^{91}\text{Nb}(p,\gamma)$ The reaction $^{91}\text{Nb}(p,\gamma)$ is not experimentally studied so far. Measurements in inverse kinematics using a storage ring or a recoil mass separator (compare Sec. 4.3) are not realized yet and a measurement in standard kinematics requires the availability of a radioactive target sample of ^{91}Nb isotopes. As the amount of target material is limited by the activity of the sample, the measurement has to be performed using γ calorimetry due to the higher sensitivity (see Sec. 4.2). Among the unstable isotopes acting as target nuclei in Fig. 5.8, the isotope ^{91}Nb has by far the longest half-life with $t_{1/2} = 680$ a. Therefore, it is the most promising candidate for the production and usage of a probe to be used in an experiment in standard kinematics.

One possible method to produce a small amount of ^{91}Nb to be used as a target is the irradiation of a molybdenum target enriched in ^{92}Mo with protons of energies between 15 MeV and 25 MeV energy [132]. Due to the closed neutron shell, the dominating reaction channels in this energy range are $^{92}\text{Mo}(p,2p)$, $^{92}\text{Mo}(p,pn)$, and $^{92}\text{Mo}(p,2n)$. Since ^{91}Nb is either produced directly or via subsequent electron capture decays the produced niobium is isotopically almost pure. As can be seen from Fig. 5.16 the production of ^{93}Nb by the

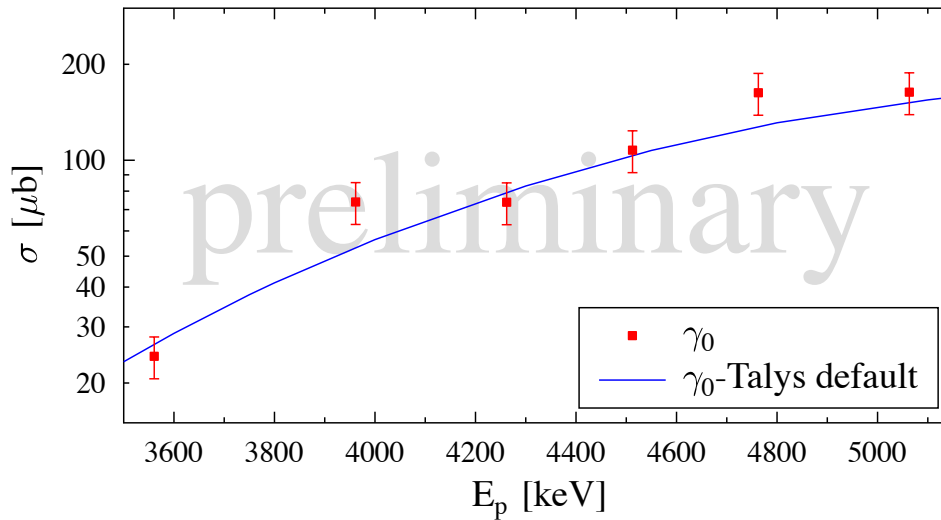


Figure 5.15:

Partial cross section of the reaction $^{90}\text{Zr}(p,\gamma)$. The results of this work (red squares) are compared to a prediction using the TALYS code in its default settings (compare Tab. 3.1). For details, see text. Taken from [131].

reaction $^{92}\text{Mo}(p,\gamma)$ is hampered by the much lower reaction cross section as well as by the very large half-life of ^{93}Mo ($t_{1/2} = 4000$ a).

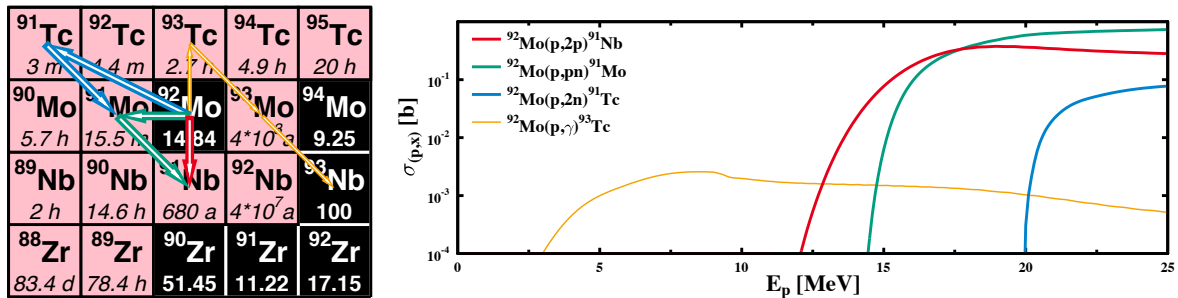


Figure 5.16:

Production of target sample of ^{91}Nb . The irradiation of an enriched ^{92}Mo target with protons between 15 MeV and 25 MeV leads to the almost isotopically pure production of ^{91}Nb . For details, see text.

The chemical purification of the sample material has to be optimized for the reduction of molybdenum in the sample. However, even if some ^{92}Mo remains in the sample material the contribution from the reaction $^{92}\text{Mo}(p,\gamma)$ to the measured spectra can be easily separated because of its different Q value ($Q = 4087$ keV) compared to the reaction $^{91}\text{Nb}(p,\gamma)$ ($Q = 7462$ keV).

The cross sections shown in Fig. 5.16 were calculated using the TALYS code [46]. Besides the reactions presented there, the calculations also predict a non-vanishing contribution of the reaction channel (p,p α) producing the unstable isotope ^{88}Zr which decays with a half-life of $t_{1/2} = 83.4$ d via ^{88}Y ($t_{1/2} = 106.6$ d) to ^{88}Sr . To check the validity of the predictions and investigate contributions of other molybdenum isotopes, an activation experiment was performed at Physikalisch Technische Bundesanstalt (PTB) Braunschweig, Germany [132].

Naturally composed molybdenum foils with areal densities of about 10.28 mg/cm² were irradiated with protons in the energy range of $E_p = 15$ MeV to 19 MeV. For each energy, a short irradiation (about 15 minutes) as well as a long irradiation (about 8 hours) were performed to account for the wide range of half-lives of the radioactive isotopes expected to be produced. Fig. 5.17 shows a typical spectrum measured directly after a short irradiation using a 100% HPGe detector provided by PTB Braunschweig, Germany. The dominating peaks correspond to the γ transitions after the β decays of ^{94}Tc and ^{94m}Tc . The decay of ^{91}Mo feeding the abundance of ^{91}Nb is also observed. For the long irradiations, the targets were stored for several weeks, thus, these short-lived isotopes disappeared. Then, another γ spectroscopy of the targets takes place using a Low-Energy Photon-Spectrometer at Goethe University Frankfurt, Germany. The setting is optimized to monitor the X rays emitted in the decay of ^{91}Nb to determine the total production yield for different proton energies. These measurements are still ongoing. The comparison of yield-to-contaminant ratios will determine the optimum incident proton energy and target thickness for the production of ^{91}Nb from highly-enriched ^{92}Mo .

If the cross section shown in Fig. 5.16 are experimentally confirmed, a ^{91}Nb sample can be produced by irradiating a molybdenum target enriched in ^{92}Mo with protons of energies of 20 MeV energy. An amount of $1.2 \cdot 10^{16}$ ^{91}Nb nuclei yields after the irradiation of 300 mg sample material enriched to 95% in ^{92}Mo with a current of about 80 μA for about 24 hrs.

Experiments with high-intensity proton-beams at FRANZ The current layout of the FRANZ facility is shown schematically in Fig. 5.18. The protons are produced in a volume-type ion-source to allow beam currents of up to $I_p = 200$ mA with energies of $E_p = 120$ keV. The Low-Energy Beam-Transport (LEBT) section consists of four solenoids to transport the beam and a chopper system to provide beam pulses with a length of about 100 ns at repetition rates of 250 kHz. The LEBT prepares the beam to characteristics accepted by the Radio-Frequency Quadrupole (RFQ). This linear accelerator component further focusses the beam and accelerate it so that it matches the requirements of the interdigital H-mode (IH) drift tube linac. After passing this second stage of acceleration, the beam has an energy of $E_p = 2$ MeV with a spread of roughly 1% due to the high space-charge density. The design current is up to $I_p = 20$ mA in a quasi continuous-wave mode as the time structure of the RFQ and IH with a repetition rate of 175 MHz and bunch lengths of 1 ns persists.

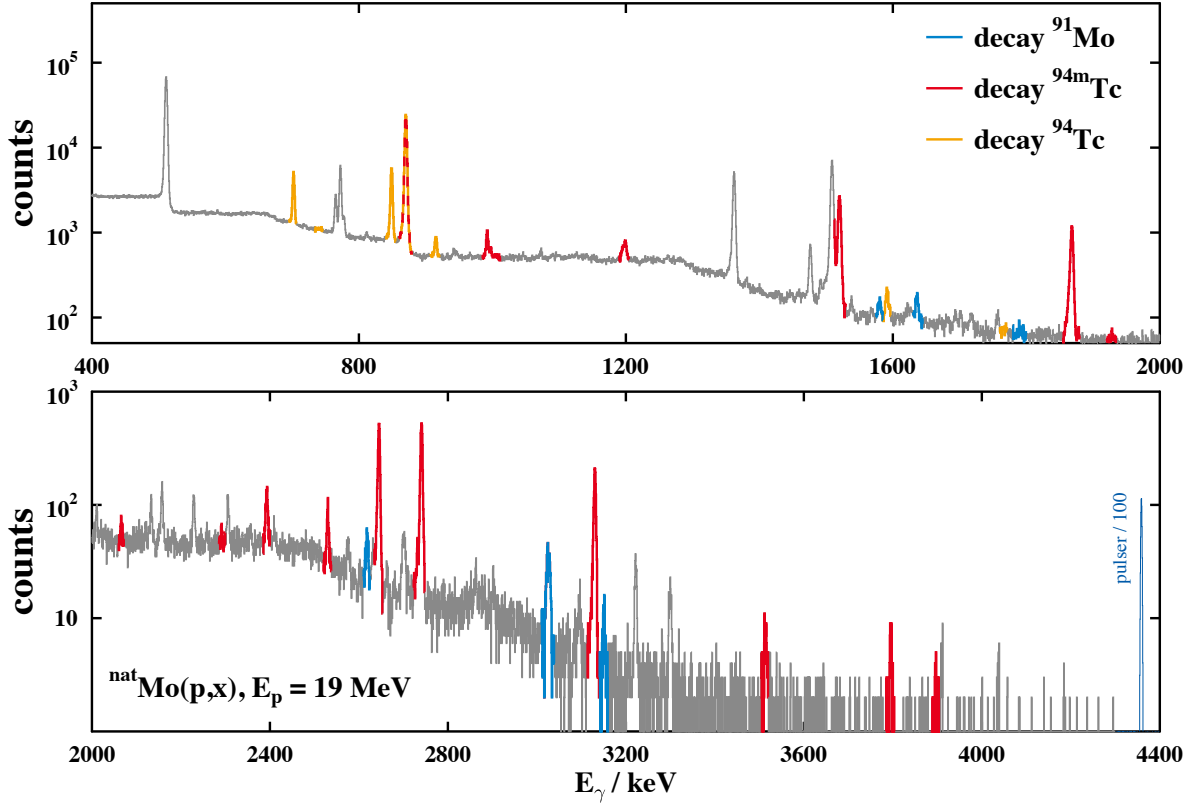


Figure 5.17:

Typical spectrum after the activation of natMo with protons. The target was irradiated for 15 minutes with $E_p = 19$ MeV. The spectrum was measured directly after the activation with a 100% HPGe detector at PTB Braunschweig. The γ transitions of the β decay of ^{91}Mo feeding ^{91}Nb are marked in blue. The main activity stems from ^{94}Tc and ^{94m}Tc produced, *e.g.*, by the $^{94}\text{Mo}(p,n)$ reaction. For details, see text.

This Medium-Energy Beam-Transport (MEBT) section is completed by a cross-bar H-mode (CH) rebuncher which allows the variation of the beam energy by 10%, therefore, energies from $E_p = 1.8$ MeV to 2.2 MeV are provided for the High-Energy Beam-Transport (HEBT) section serving the experimental setups [133]. The dipole magnet of the HEBT allows the deflection in three different beam-lines. The beam-dump is located straightforward while two experimental setups are available at deflection angles of 40° and 80° , respectively.

The beam-line at 80° is dedicated to experiments using the activation technique with neutrons as projectiles. The proton beam impinges on a neutron production target of ^7Li . Neutrons are released in the energy range of several keV up to 200 keV corresponding to the exact proton-beam energy and target thickness [103]. The beam-line at 40° is optimized for in-beam experiments using a 4π BaF_2 calorimeter [94] for the detection of

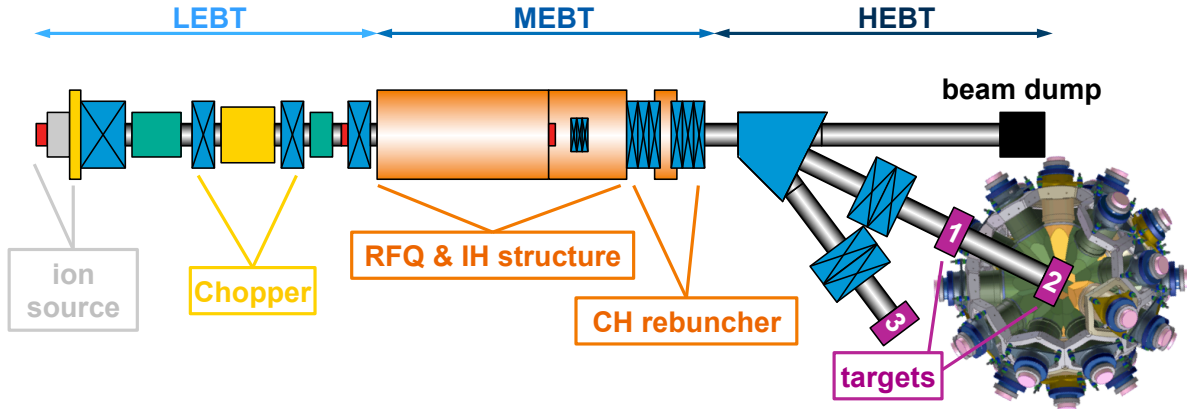


Figure 5.18:
Schematic layout of the FRANZ facility, Frankfurt a.M., Germany. For details, see text.

prompt photons emitted in a radiative proton- or neutron-capture reaction, respectively. A doublet of quadrupole magnets is used to focus the beam on either the neutron production target or the target for proton-capture. Table 5.5 lists the main characteristics of the magnets. A camera system is used as a diagnostic tool in a twofold way. First, it monitors the position of the beam-spot and allows adjustment via steering to ensure the alignment with the target. Second, it allows the determination of the power deposition in the sample during the experimental run by the observation of the thermal radiation emitted of the sample material to know the beam intensity profile and use it during the analysis of the data.

Table 5.5:

The basic components of the HEBT section at FRANZ is the deflecting dipole magnet and a doublet of quadrupole magnets to focus the beam. Their main characteristics as derived within this work are listed.

dipole magnet		quadrupole magnets	
maximum field B :	1.0 T	maximum field gradient G :	7.6 T/m
bending radius R_0 :	216 mm	maximum pole tip field B_0 :	0.41 T
bending angle ϕ :	20–90°	effective magnetic length L_{eff} :	150 mm
pole iron gap d :	40 mm	overall length of singlet L_{overall} :	260 mm
pole base width W :	150–300 mm	aperture diameter d :	105 mm
current I :	175 A	current I :	137 A
voltage U :	17 V	voltage U :	13 V
power P :	3 kW	power P :	1.8 kW

Figure 5.18 shows the results of the beam-transport simulation through the HEBT section using the simulation software TraceWin [134]. The envelope of the beam in x and

y direction, *i.e.*, the 3σ range where 99.7% of the beam intensity is located, is depicted with magnet settings optimized for target position 2 in Fig. 5.18. At distance 0 cm, the beam is delivered by the CH rebuncher with a diameter of 17 mm and 12 mm in x and y direction, respectively. The dipole magnet deflecting the beam into the 40° beam line is located at a distance of 38.3 cm. It focusses the beam in x direction, *i.e.*, in the deflection plane. Neglecting fringe fields, its influence in the y direction is negligible, thus, the high space charge of the beam yields defocussing.

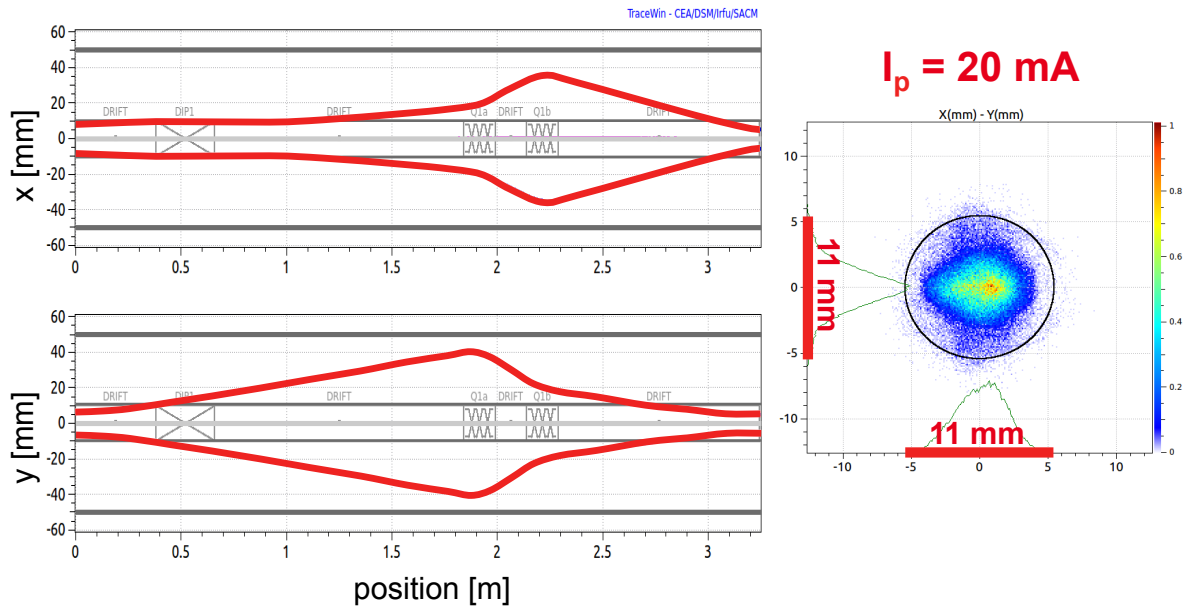


Figure 5.19: Simulation of beam transport in HEBT section of FRANZ. The left panels show the change of the envelope of the beam as a function of its position in the HEBT section. The right panel depicts the dimension of the beam at target position 2 in Fig. 5.18. For details, see text.

The quadrupole doublet at a distance of 184 cm focusses first in x and then in y direction. It is possible to confine the beam diameter at target position (325 cm distance) to values of $\Delta x = 11$ mm and $\Delta y = 11$ mm. Compared to beams with lower intensities as delivered from, *e.g.*, tandem accelerators, the resulting beam spot is quite large. However, the high intensity and the resulting high power deposition require a broad area where the beam hits the target to avoid damage of the target. Intrinsically small beam spots are broadened by defocussing or wobbling to avoid damage of the targets. In our case, the areal power density is about 105 W/cm^2 – a manageable value if sophisticated cooling methods are applied.

Development of high-power resistive targets Different techniques are applied to avoid damage of targets when they are heated by the power deposition of a charged-

particle beam. Corresponding to the expected heating of the target, cooling by ventilation, by high-pressure water-flow, or indirectly by liquid nitrogen with a cooling finger are used in varying realizations. In case of the study of proton-induced reactions at FRANZ, the total power deposition is as high as $P_{\text{dep}} = 10$ kW for a beam with $E_p = 2$ MeV and $I_p = 5$ mA.

In contrast to experiments with well-collimated beams, the power deposition occurs on a rather broad area. Therefore, cooling by a high-pressure water-flow might still be sufficient if an optimized combination of target and backing material is found. When investigating the $^{91}\text{Nb}(p,\gamma)$ reaction using calorimetry of the prompt γ rays, as foreseen at FRANZ, the Q values of all reactions occurring in the backing material should be much lower than $Q(^{91}\text{Nb}(p,\gamma)) = 7458$ keV. Thus, the background stemming from the backing material occurs at lower energies in the measured spectra and does not interfere with the signal. Nevertheless, the cross section for radiative proton-capture reactions should be small to avoid high background-induced count rates in the detection system. Due to the small range of the low-energy protons, the power will be deposited in the front of the backing material while the cooling is applied in the back. Therefore, a high thermal conductivity is mandatory to ensure a sufficient heat transfer from the backing material to the water cooling and the melting temperature must be high. In addition, the material should be available in metallic form with highest elemental purities and provide easy machining [135].

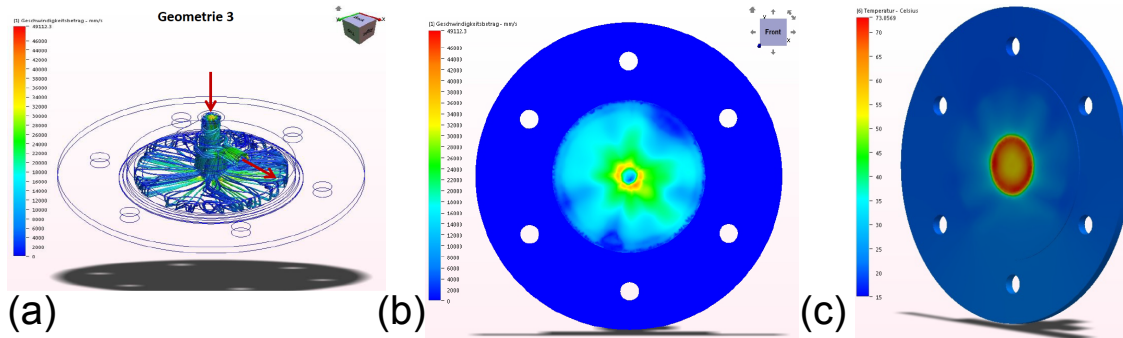


Figure 5.20:

Exemplary simulation of high-pressure water-flow cooling. (a) Geometry of the inlet and outlet apertures. (b) Velocity distribution of water-flow projected on backing material. (c) Temperature distribution in the backing material. Composed from [135].

Taking into account the constraints on the backing material in the listed order, the most suitable material for the $^{91}\text{Nb}(p,\gamma)$ reaction is tungsten. The highest Q value of its isotopes is reached for the most neutron-rich stable tungsten isotope: $Q(^{186}\text{W}) = 5997$ keV. The cross section for the $^{186}\text{W}(p,\gamma)$ reaction at $E_p = 2$ MeV is about eight orders of magnitude smaller compared to the $^{91}\text{Nb}(p,\gamma)$ reaction. In addition, its thermal conductivity amounts to $k = 174.0$ W m $^{-1}$ K $^{-1}$. It can be ordered from stock as metallic foil in varying thicknesses with elemental purities of up to 99.95%.

Different geometries for the water flow were simulated using Autodesk® Simulation Computational Fluid Dynamics [136]. Figure 5.20(a) illustrates the geometry of the inlet and outlet apertures and the water flow resulting in the lowest peak-temperatures. The water is injected to the center of the disk of backing material, flows towards its edges, and is reabsorbed with an outlet at the center. The velocity of the water flow is slowed down from the center to the edges as shown in Fig. 5.20(b). Therefore, the temperature of the backing material is efficiently reduced in the center but rises towards the edges of the beam-spot as depicted in Fig. 5.20(c). For a proton current of $I_p = 2$ mA, the temperature will not exceed 200°C , thus, neither the target material nor any of the material used for mounting will be damaged [135].

The distribution of protons within the area of the beam-spot was chosen homogeneously for these first simulations. However, the implementation of the intensity profile of the proton beam as extracted from Fig. 5.19 is mandatory to receive a more realistic temperature distribution. Before a prototype is built, a draft of the target chamber including all supply lines is needed to examine whether the presented geometry fits well into the 4π BaF₂ calorimeter.

Draft of target chamber to study (p,γ) reactions at FRANZ The 4π BaF₂ calorimeter to be used for the study of (p,γ) reactions at FRANZ was originally designed and optimized for the study of (n,γ) reactions. Therefore, the space inside the detector's spherical shell is very limited and it is also in short supply of feedthroughs. A draft of the target chamber takes into account the basic requirements to investigate radiative proton-capture reactions: an extension of the beam-line into the detector's spherical shell, a cold trap to reduce deposits of residual gas at the target's surface, a measurement of the current impinging the target, and a cooling mechanism as described in the previous paragraph [137].

The beam-line at FRANZ has a broad diameter of 10 cm (compare Fig. 5.19). If one of the detector modules with pentagonal section is removed the maximum diameter available amounts to 48 mm. Therefore, the extension of the beam-line is cone-shaped as shown in Fig. 5.21. The cold-trap consists of a hollow cylinder made of copper which is indirectly cooled from a reservoir of liquid nitrogen located outside the calorimeter by a thin copper bar with rectangular section. The length of the section is determined to 25 mm by an available feedthrough of the calorimeter. The width was varied in a simulation to optimize the final temperature of the hollow cylinder. An acceptable trade-off between heat transmission and losses was found for a width of 8 mm if no heat insulation was applied [137].

The measurement of the current impinging the target is accompanied by the construction of an aperture and the application of an electron suppression potential. The former is needed to control the position of the beam-spot at the target and – if needed – to adjust this position by a set of steerers located after the focussing quadrupole doublet (compare Fig. 5.18) with the aim of centering the beam-spot to the target. The latter

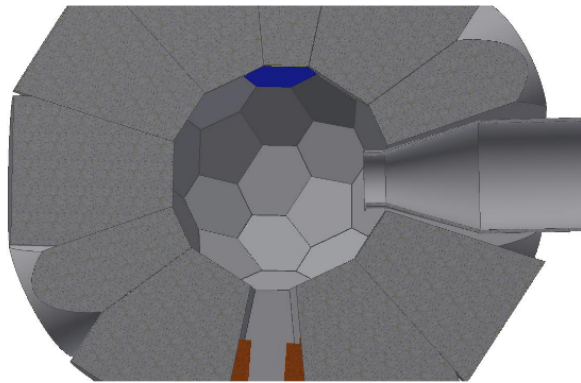


Figure 5.21:

Half-section of 4π BaF₂ calorimeter with cone-shaped end of beam-line. A detector module with pentagonal section is removed to insert a cone-shaped part of the beam-line. The cone reduces the diameter from 100 mm to 48 mm. The cylindrical end is needed to mount the target chamber and to house apertures for beam diagnostics and electron suppression (compare Fig. 5.22). Taken from [137].

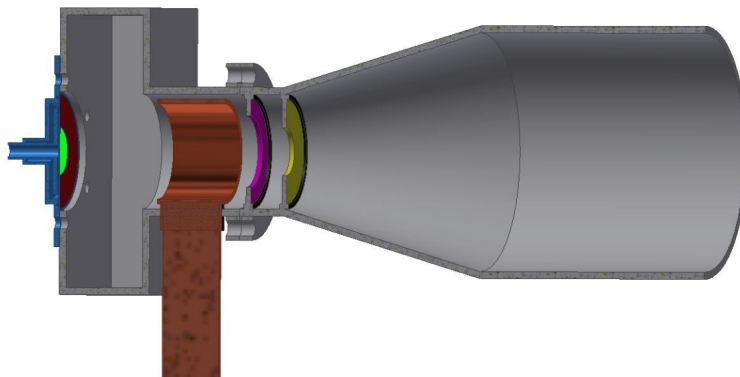


Figure 5.22:

Half-section of target chamber for 4π BaF₂ calorimeter with cone-shaped end of beam-line. On the left, the mounting structure for the target including the inlet and outlet of the high-pressure water cooling is shown in blue. The size of a typical beam-spot is indicated in green. The cold-trap is located between the end of the beamline and the target chamber (brown). The magenta aperture is used to apply an electron suppression potential while the yellow one controls the position of the beam-spot. Taken from [137].

is mandatory for a correct measurement of the absolute current stemming from the proton beam. Secondary electrons emitted from the target are deflected to the target by the applied potential to avoid an incorrect measurement of the current at the target. The space and location of both devices is defined (compare Fig. 5.22) but the final characteristics are not yet fixed.

The final design of the target chamber and its construction in combination with high-power resistive targets are realized within a recently started Master thesis [138].

5.2 Photon-induced reactions

As explained in Chap. 2, photon-induced reactions play a major role in the γ process producing the p nuclei. After the excitation of the target nucleus above the particle-separation threshold, neutrons or charged-particles are emitted in a (γ,n) , (γ,p) or (γ,α) reaction. High temperatures of several 10^9 K provide a continuous-energy spectrum of photons with a significant amount in the MeV-energy range as described by the Planck's distribution. However, due to these temperatures, nuclear states in the MeV-energy range can be populated as described by the Boltzmann equation. Therefore, the experimental determination of the corresponding stellar reaction rate is hampered.

To mimic this situation as close as possible, the inverse reactions are usually studied experimentally (compare Sec. 5.1) and the cross section of the photon-induced reaction is derived by the principle of detailed balance. If the photon-induced reaction is directly studied only the contribution of the ground-state to the stellar reaction rate is determined. As stated in [139], the amount of this contribution is generally far below the percent range. Therefore, . . . *The fact that photodisintegrations play a role in certain astrophysical processes, specifically in the γ process, often gives rise to the misconception that a photodisintegration measurement will directly help with determining the astrophysical reaction rate.* (quote from T. Rauscher, [140]). However, . . . *the experimental study of γ -induced reactions can provide useful information for certain nuclear properties relevant to heavy element nucleosynthesis.* (quote from T. Rauscher *et al.*, [139]), especially, if the partial cross sections are measured in addition to the total cross section (compare Sec. 7).

The following subsections focus on recently performed studies with photon-induced reactions. In Subsec. 5.2.1, a systematic approach for (γ,n) reactions in a wide mass range of $140 \leq A \leq 204$ is presented. Since many unstable isotopes are part of the reaction network for the γ process, the usage of inverse kinematics is mandatory to study the most influential reactions. The example of (γ,n) reactions on molybdenum isotopes is explained in Subsec. 5.2.2.

5.2.1 Systematic studies with real photons

Real-photon beams are available from different sources with varying characteristics. During the 1950s to 1970s, photons from in-flight positron annihilation were widely used to study giant dipole resonances systematically [141]. Later, other groups performed similar studies using bremsstrahlung sources, *e.g.*, [142]. However, studies related to the nucleosynthesis of the p nuclei have to cover the energy range right above the particle separation threshold (compare Fig. 3.4). Recently, measurements were performed using bremsstrahlung sources, *e.g.*, [143, 144, 88, 87, 145] as well as quasi-monoenergetic

photons from Laser Compton Backscattering, *e.g.*, [65, 146, 147] and [148] as review. Also tagged photons are available in this energy range with high energy resolution at the low-energy photon tagger NEPTUN at the S-DALINAC, Darmstadt [101].

Studying charged-particle induced reactions, the cross section of a reaction is determined experimentally and the reaction rate is calculated from a deconvolution of the cross section and the Maxwell-Boltzmann distribution (compare Chap. 3). In the case of photon-induced reactions, continuous-energy bremsstrahlung yields the cross section σ only for the complete energy range of the bremsstrahlung spectrum which ranges from 0 to the energy of the electron beam E_{\max} producing the bremsstrahlung spectrum. Thus, an energy-integrated cross section I_σ is usually introduced and the reaction yield Y equals:

$$Y = N_T \cdot I_\sigma(E_{\max}) = N_T \int_S^{E_{\max}} \sigma(E) \cdot N_\gamma^{\text{brems}}(E, E_{\max}) \cdot dE \quad (5.12)$$

with the number of target atoms N_T , the reaction threshold S , the maximum energy of the bremsstrahlung distribution E_{\max} , and the number of photons per unit area and energy $N_\gamma^{\text{brems}}(E, E_{\max})$. Therefore, a deconvolution of the cross section $\sigma(E)$ is needed. This can be realized using assumptions on the energy dependence [149] or sophisticated deconvolution methods [150].

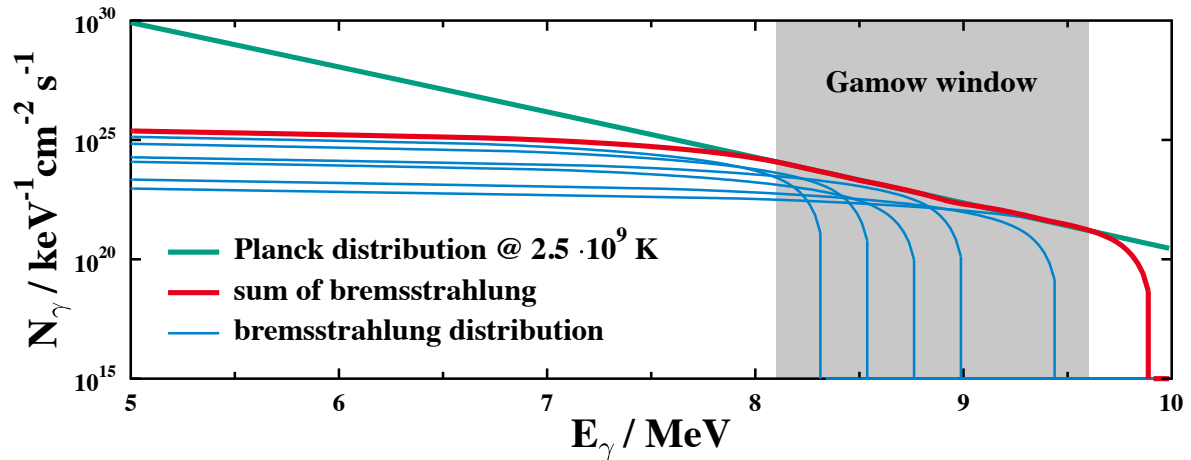


Figure 5.23:

Approximation of a Planck distribution by bremsstrahlung spectra. The exponential tail of a Planck distribution n_{Planck} at a temperature of $2.5 \cdot 10^9$ K is shown (green) in the energy range of 5 MeV to 10 MeV. The red line is the sum of several bremsstrahlung distributions $N_{\gamma,i}^{\text{brems}}(E, E_{\max,i})$ weighted with temperature dependent factors $a_i(T)$ (blue) with different maximum energies $E_{\max,i}$ and approximates the Planck distribution in the grey shaded area.

However, the information of astrophysical interest is the reaction rate $\lambda(T)$ for a given

temperature:

$$\lambda(T) = \int c \cdot n_{\text{Planck}}(T) \cdot \sigma(E) \cdot dE. \quad (5.13)$$

Instead of determining the cross section $\sigma(E)$ and calculating the rate using the Planck distribution $n_{\text{Planck}}(T)$ (compare Eq. (3.6), the rate is directly determined if the Planck distribution can be approximated experimentally.

Figure 5.23 illustrates that a sum of bremsstrahlung spectra each weighted by a temperature dependent factor $a_i(T)$ reproduces the Planck distribution in the astrophysically interesting energy range (compare Fig. 3.4). Thus, the Planck distribution is approximated by

$$c \cdot n_{\text{Planck}}(T) \approx \sum a_i(T) \cdot N_{\gamma,i}^{\text{brems}}(E, E_{\text{max},i}). \quad (5.14)$$

the reaction rate can be rewritten using Eqs. (5.16) and (5.12) to

$$\lambda(T) \propto \sum a_i(T) \cdot A(E_{\text{max},i}) \quad (5.15)$$

with $A(E_{\text{max},i})$ being proportional to the reaction yield Y . However, the data are derived under laboratory conditions, *i.e.*, no excited states are populated in the target nuclei. Therefore, it is more appropriate to call the results derived with this method ground-state reaction rates.

We used the activation approach in combination with high-resolution γ spectroscopy (compare Sec. 4.1). In this case, $A(E_{\text{max},i})$ is determined by

$$A = \varepsilon_{\gamma} \cdot I_{\gamma} \cdot \tau \cdot \frac{t_L}{t_R} \cdot Y \quad (5.16)$$

with the detector efficiency ε_{γ} , the branching factor I_{γ} of the observed decay line, and the dead-time correction t_L/t_R . The factor τ corrects for the continuous decay of produced unstable nuclei during the activation, waiting time and γ spectroscopy. Its detailed composition was already explained in Subsec. 5.1.1.

During the last years, a systematic study of (γ, n) reactions in the mass region $140 \leq A \leq 210$ was performed with the described approach at the Darmstadt High-Intensity Photon Setup (DHIPS) [145]. The ground-state reaction rates were determined measuring and analyzing spectra as shown exemplarily in Fig. 5.24 for the activation of $^{\text{nat}}\text{Yb}$, $^{\text{nat}}\text{Hg}$, and $^{\text{nat}}\text{Pb}$ with photons. Tables 5.6 and 5.7 list the investigated reactions and the corresponding characteristics of the experiments like the target properties, activation energies and durations, half-life of the reaction product and observed γ transitions, respectively. The results of measurements are shown in Fig. 5.25. The aim of this systematic study was the test of the reliability of reaction rates predicted within the Hauser-Feshbach statistical model. Thus, the experimentally determined ground-state reaction rates are compared to predicted values with the standard settings of the TALYS code [46] (compare Tab. 3.1). As shown in Fig. 5.25, no systematic deviations were

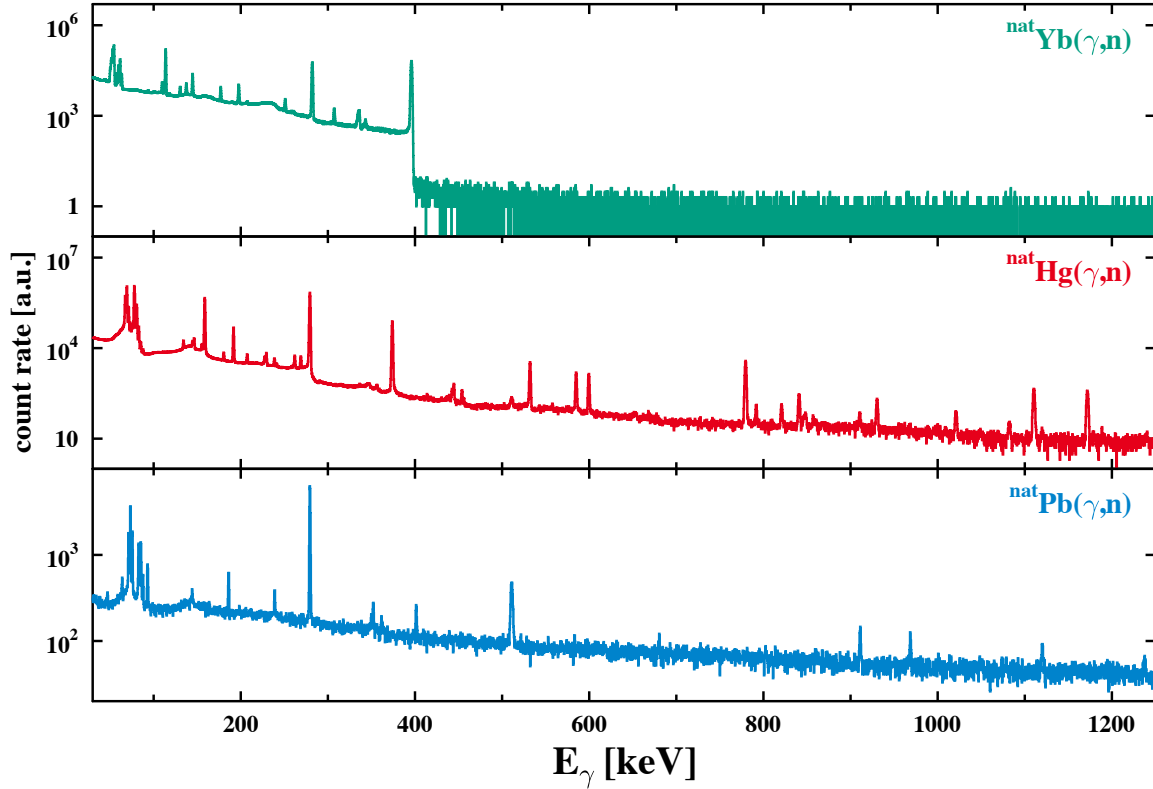


Figure 5.24:

Spectra after irradiation of $^{\text{nat}}\text{Yb}$, $^{\text{nat}}\text{Hg}$, and $^{\text{nat}}\text{Pb}$ with photons. The spectra were measured with different HPGe detectors after the activation of the targets at DHIPS, Darmstadt [145]. For detailed information on the corresponding experiments, see Tab. 5.6.

found and no deviation bigger than the normally stated accuracy of a factor of 3 for (γ, n) reactions [22] occurred.

In addition to this systematic study, quasi-monoenergetic photons from Laser Compton Backscattering (LCB) were used to investigate (γ, n) reactions with the activation approach [146, 152, 147, 153]. The High Intensity γ -ray Source (HI γ S), at Triangle Universities Nuclear Laboratory, U.S.A., provides today the most intense LCB photon beam in the MeV-energy range [151]. Due to the different shape of the produced photon spectrum (compare Fig. 5.26), the extraction of the ground-state reaction rate as described above is not possible but the cross section can be derived as a function of energy. Although the systematic uncertainties are different if bremsstrahlung or LCB photons are used the extracted reaction rates agree well within uncertainties [147].

Using LCB photons for an in-beam experiment meets the demands of T. Rauscher *et al.* quoted in the beginning of Sec. 5.2 [139] for experimental information of the partial cross section of (γ, n) reactions. For that purpose, the neutrons must be detected in coincidence with the prompt γ rays emitted if an excited state is populated in the product nucleus.

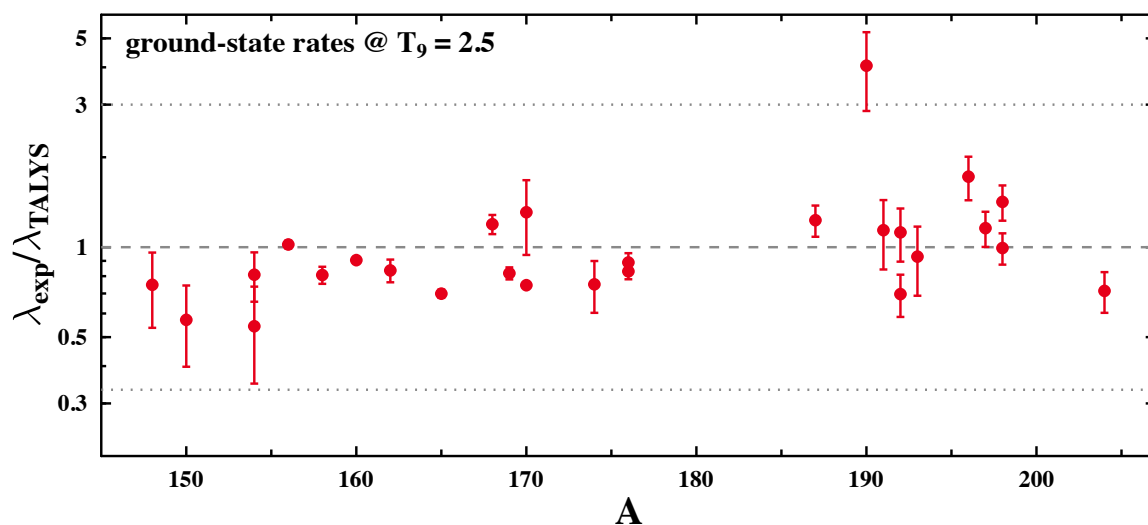


Figure 5.25:

Comparison of measured to predicted (γ,n) rates of (γ,n) reactions. The ratio of the experimentally determined reaction rate λ_{exp} to the rate λ_{TALYS} predicted with the standard settings of the TALYS code [46] is shown. The picture summarizes data of the experimental campaigns listed in Tabs. 5.6 and 5.7.

At HI γ S, the γ^3 setup is available to detect these prompt γ rays with a combination of HPGe and LaBr detectors [72]. This setup will be extended with neutron detectors and the determination of partial cross sections of the reaction $^{87}\text{Rb}(\gamma,n)$ will be investigated next year [154].

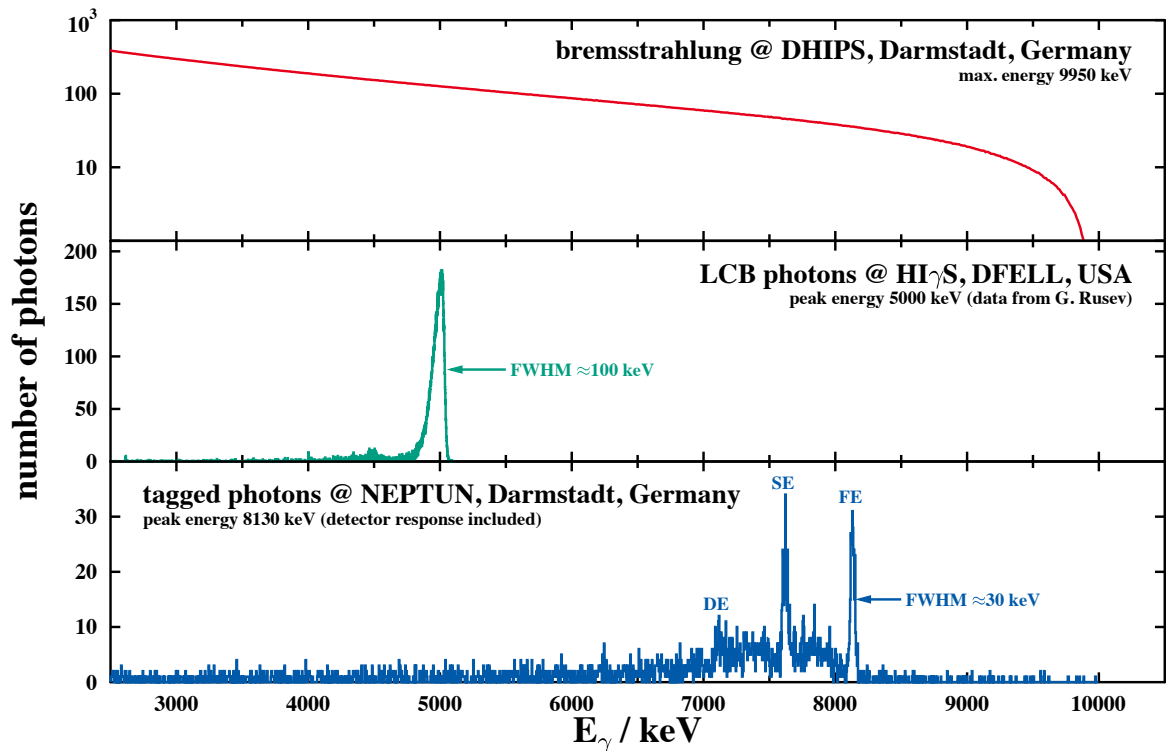


Figure 5.26:

Spectral composition of photon beams from different sources. at DHIPS and HI γ S. *top*: Bremsstrahlung spectrum produced with an electron beam of an energy of 9950 keV at DHIPS, Darmstadt. [145]. *middle*: LCB photons produced at HI γ S, U.S.A. Both, position and width of the peak are adjustable (see [151]). *bottom*: Tagged photons produced at NEPTUN, Darmstadt [101]. The energy resolution of the tagged photons allows the identification of the detector response of the used HPGc detector.

Table 5.6: Experiments performed within systematic study of (γ, n) reactions at DHIPS, Darmstadt [145]. Target material and average masses $\langle \text{mass} \rangle$ are listed with the energies E_{max} and average durations $\langle t_{\text{act}} \rangle$ of the activation. The observed reaction is listed with the neutron separation energy S_n , the half-life $t_{1/2}$ of the reaction product and the γ transitions with the highest intensity per decay observed in the spectra measured with HPGe detectors.

target	$\langle \text{mass} \rangle$ [mg]	E_{max} [keV]	$\langle t_{\text{act}} \rangle$ [h]	reaction	S_n [keV]	$t_{1/2}$	γ transition	Ref.
^{148}Nd , metal	40–50	7450–9800	6–24	$^{148}\text{Nd}(\gamma, n)$	7333	10.98(1) d	91.1, 531.0 keV	[88]
^{150}Nd , metal	40–50	7450–9800	6–24	$^{150}\text{Nd}(\gamma, n)$	7380	1.728(1) h	211.3, 114.3 keV	[88]
^{154}Sm , oxide	500–1750	7450–9800	6–24	$^{154}\text{Sm}(\gamma, n)$	7968	46.284(4) h	103.2, 69.7 keV	[88]
^{154}Gd , metal	40–50	7450–9800	6–24	$^{154}\text{Gd}(\gamma, n)$	8895	240.4(10) d	97.4, 103.2 keV	[88]
^{160}Gd , metal	40–50	7450–9800	6–24	$^{160}\text{Gd}(\gamma, n)$	7451	18.479(4) h	363.6, 58.0 keV	[88]
^{156}Dy , oxide	600–1300	9050–9900	6–24	$^{156}\text{Dy}(\gamma, n)$	9441	9.9(2) h	226.9, 184.6 keV	[155]
^{158}Dy , oxide	600–1300	9050–9900	6–24	$^{158}\text{Dy}(\gamma, n)$	9056	8.14(4) h	326.3, 182.4 keV	[155]
^{160}Dy , oxide	600–1300	9050–9900	6–24	$^{160}\text{Dy}(\gamma, n)$	8576	144.4(2) d	58.0 keV	[155]
^{165}Ho , oxide	1100–1900	8370–9900	0.5	$^{165}\text{Ho}(\gamma, n)$	7988	29(1) min	91.4, 73.4 keV	[155]
^{162}Er , oxide	1000–1500	7450–9900	3–24	$^{162}\text{Er}(\gamma, n)$	9205	3.21(3) h	826.6, 211.2 keV	[155]
^{170}Er , oxide	1000–1500	7450–9900	3–24	$^{170}\text{Er}(\gamma, n)$	7257	9.391(18) d	109.8 keV	[155]
^{169}Tm , oxide	700–1000	8370–9900	6–24	$^{169}\text{Tm}(\gamma, n)$	8034	93.1(2) d	198.3, 816.0 keV	[155]
^{168}Yb , oxide	800–1900	7150–9900	6–24	$^{168}\text{Yb}(\gamma, n)$	9051	(9.25 d) ^a	(207 keV) ^a	[155]
^{170}Yb , oxide	800–1900	7150–9900	6–24	$^{170}\text{Yb}(\gamma, n)$	8470	32.018(5) d	63.1, 198.0	[155]
^{176}Yb , oxide	800–1900	7150–9900	6–24	$^{176}\text{Yb}(\gamma, n)$	6865	4.185(1) d	396.3, 282.5 keV	[155]
^{174}Hf , oxide	800–900	8370–9900	6–24	$^{174}\text{Hf}(\gamma, n)$	8506	23.6(1) h	123.7, 297.0 keV	[155]
^{176}Hf , oxide	800–900	8370–9900	6–24	$^{176}\text{Hf}(\gamma, n)$	8165	70(2) d	343, 434 keV	[155]
^{185}Re , metal	340	7650–9900	24	$^{185}\text{Re}(\gamma, n)$	7669	35.4(7) d	111.2 keV	[156]
^{187}Re , metal	340	7650–9900	24	$^{187}\text{Re}(\gamma, n)$	7359	3.7186(5) d	137.2, 122.6 keV	[156]

^a subsequent decay of ^{167}Tm , $t_{1/2}(^{167}\text{Yb}) = 17.5(2)$ min

Table 5.7:
Experiments performed within systematic study of (γ, n) reactions at DHIPS, Darmstadt [145]. Target material and average masses (mass) are listed with the energies E_{max} and average durations $\langle t_{\text{act}} \rangle$ of the activation. The observed reaction is listed with the neutron separation energy S_n , the half-life $t_{1/2}$ of the reaction product and the γ transitions with the highest intensity per decay observed in the spectra measured with HPGe detectors. Tab. 5.6 continued.

$^{\text{nat}}\text{Os}$, oxide	300–450	7600–9200	6–24	$^{192}\text{Os}(\gamma, n)$, $^{191}\text{Os}_{\text{g.s.}}$	7558	15.4(1) d	129.4 keV	[87]
$^{\text{nat}}\text{Os}$, oxide	300–450	7600–9200	6–24	$^{192}\text{Os}(\gamma, n)$, $^{191}\text{Os}_m$	7632	13.10(5) h	74.4 keV	[87]
$^{\text{nat}}\text{Ir}$, metal	330	7875–9900	6–24	$^{193}\text{Ir}(\gamma, n)$	7772	73.827(13) d	316.5, 468.1 keV	[87]
$^{\text{nat}}\text{Pb}$, metal	440	8775–9900	12–24	$^{204}\text{Pb}(\gamma, n)$	8395	51.87(1) h	401.3, 279.2 keV	[157]
$^{\text{nat}}\text{Hg}$, sulfide	1970–2720	8325–9900	12–24	$^{196}\text{Hg}(\gamma, n)$	8839	9.9(5) h	779.8, 61.5 keV	[157]
$^{\text{nat}}\text{Hg}$, sulfide	1970–2720	8325–9900	12–24	$^{198}\text{Hg}(\gamma, n)$	8484	64.14(5) h	77.4, 191.4 keV	[157]
$^{\text{nat}}\text{Hg}$, sulfide	1970–2720	8325–9900	12–24	$^{204}\text{Hg}(\gamma, n)$	7495	46.61(2) d	279.2 keV	[157]
$^{\text{nat}}\text{Pt}$, metal	800	7650–9900	24	$^{190}\text{Pt}(\gamma, n)$	8911	10.87(12) h	608.0, 568.9 keV	[143]
$^{\text{nat}}\text{Pt}$, metal	800	7650–9900	24	$^{192}\text{Pt}(\gamma, n)$	8676	2.83(2) d	538.9, 409.4 keV	[143]
$^{\text{nat}}\text{Pt}$, metal	800	7650–9900	24	$^{198}\text{Pt}(\gamma, n)$	7557	19.8915(19) h	77.4, 191.4 keV	[143]
$^{\text{nat}}\text{Au}$, metal	150	8325–9900	12–24	$^{197}\text{Au}(\gamma, n)$	8072	6.1669(6) d	355.7, 333.0 keV	[149]

5.2.2 (γ, n) reactions with virtual photons

Extending the systematic studies described in the previous subsection towards unstable nuclei relies on the usage of radioactive ion beams in inverse kinematics. Compared to particle-induced reactions, the situation is complicated for photon-induced reactions as a target of photons has to be provided. This is realized by the technique of Coulomb excitation in which a target of a high- Z element is bombarded with a radioactive ion beam of relativistic energies. *E.g.*, if the reaction ${}^AZ(\gamma, n){}^{A-1}Z$ is of interest, the reaction $\text{Pb}({}^AZ, {}^{A-1}Z+n)\text{Pb}$ is studied. Due to the Lorentz contraction of the electromagnetic field of the target nuclei, the radioactive projectiles pass a high-energy field of so-called virtual photons. If the interaction leaves the projectiles in excited states above the particle separation threshold the process is called Coulomb dissociation (CD). The reaction products are kinematically focused in forward direction and have similar energies as the incident ion beam. This process is schematically shown in Fig. 5.27.

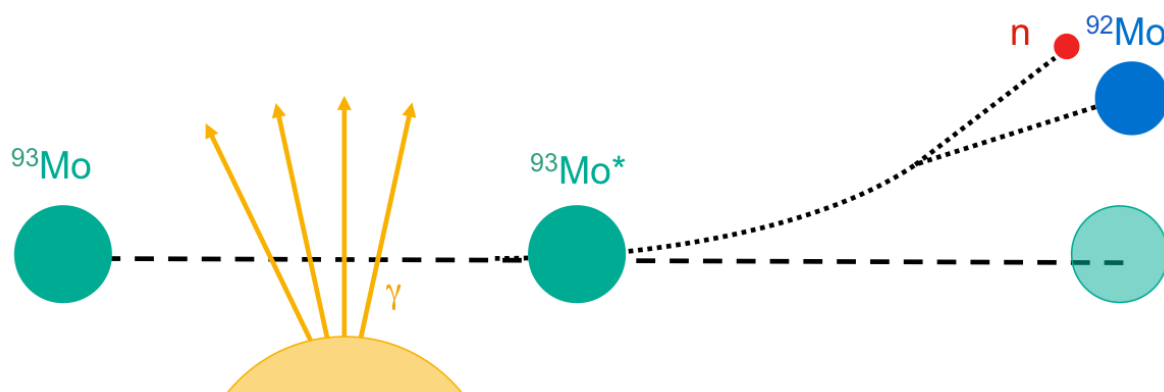


Figure 5.27:

Schematic view of a Coulomb Dissociation reaction. The high-energy projectile impinges on the Lorentz contracted Coulomb field of a high- Z target. If it is left in an excited state above the neutron separation threshold S_n , a neutron is emitted. All reaction products are focussed into forward direction.

The energy of the projectiles is chosen as high as possible due to several reasons. First of all, the higher the energy of the projectile the more the Coulomb field of the high- Z nucleus is distorted, thus, leading to a higher fraction of E1 excitations. Secondly, the used detection systems cover 4π solid angles due to the fact that all reaction products are predominantly focussed in forward directions. At last, CD dominates the nuclear background for small scattering angles, hence, avoiding low statistics after the subtraction of this background component.

The excitation energy E^* is determined by the invariant-mass method. All projectile-like decay products are detected in a kinematically complete experiment. Additionally, the γ rays emitted by the excited projectile near the target position are measured yielding information whether an excited state of the product nucleus was populated. The

excitation energy E^* is then derived by

$$E^* = c^2 \sqrt{\sum_i^N m_i^2 + \sum_{i \neq j}^N \gamma_i \gamma_j m_i m_j (1 - \beta_i \beta_j \cos \theta_{ij})} - m_{\text{projectile}} c^2 + E_\gamma. \quad (5.17)$$

Here, $m_{\text{projectile}}$ is the rest mass of the projectile and E_γ is the energy of the prompt γ rays in the projectile rest frame. The variables $\beta_{i,j}$, $\gamma_{i,j}$, and $m_{i,j}$ are the velocities, Lorentz factors, and rest masses of N outgoing particles, respectively. The angle between their momentum vectors $\vec{p}_{i,j}$ is denoted θ_{ij} .

The cross section of a photon-induced reaction σ_γ is related to the differential CD cross section $d\sigma_{CD}/dE^*$ by

$$\frac{d\sigma_{CD}}{dE^*} = \frac{1}{E^*} n_\lambda(E^*) \cdot \sigma_{\gamma,\lambda} \quad (5.18)$$

with the excitation energy E^* and the number of virtual photons, n_λ , of a given multipolarity λ [158]. In contrast to real photons, the multipolarity is not equally distributed in a virtual photon field. The energy dependence of the different multiplicities as well as their relative distribution depends on the chosen kinematics and is calculated based on the approach by Weizsäcker and Williams [159]. An example is shown in Fig. 5.28.

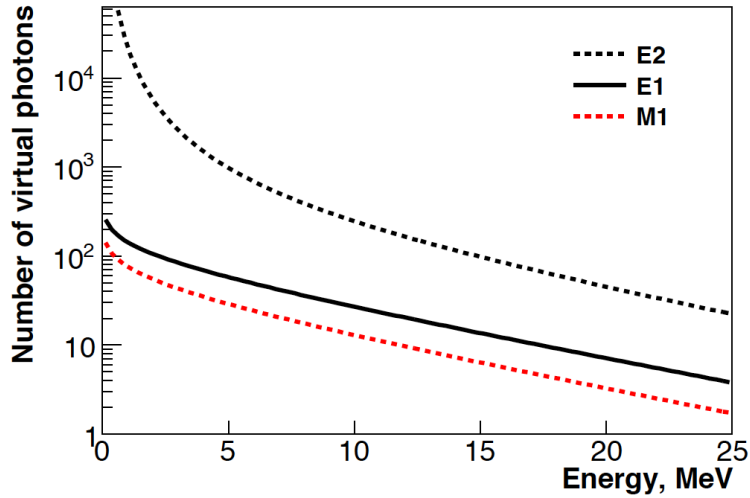


Figure 5.28:

Virtual photon spectra for different multiplicities. Unlike in case of real photons, the virtual photon field depends on multipolarity. The energy dependencies as well as the relative amounts of the different multiplicities are determined by the chosen kinematics. The photon fields are shown for ^{100}Mo impinging with 500 AMeV on a Pb target. Taken from [160].

The CD cross section σ_{CD} is derived from the reaction probability P which is determined by how often the outgoing channel was observed in comparison to the number of incoming

particles:

$$P = \frac{\# \text{ outgoing reacted ions}}{\# \text{ incoming ions}} \approx \frac{\# \text{ reacted ions}}{\# \text{ unreacted ions}}. \quad (5.19)$$

However, the CD cross section σ_{CD} cannot be determined by the reaction probability of a lead target P_{Pb} only. First of all, there is a non-negligible probability that the dissociation reaction takes place at the setup material instead. This probability P_{empty} is derived from a measurement without a target and its contribution is simply subtracted. Furthermore, nuclear break-up as another reaction mechanism has to be considered as well. This probability is determined by a measurement with a low- Z target like, *e.g.*, carbon for which Coulomb excitation is negligible because of the Z^2 dependence of the amount of virtual photons. As the lead and carbon nuclei provide different radial dimensions, a scaling factor α is introduced to normalize the components.

This scaling factor can be calculated from a geometrical approach, the so-called black-disk model, to

$$\alpha_{\text{black disk}} = \frac{A_{\text{proj}}^{1/3} + A_{\text{Pb}}^{1/3}}{A_{\text{proj}}^{1/3} + A_{\text{C}}^{1/3}}. \quad (5.20)$$

Another approach is the analysis of reaction channels which do not occur due to Coulomb excitation as their reaction threshold is close to or above the so-called adiabatic cut-off energy $E_{\text{cut-off}} = \hbar\gamma\beta c/b_{\text{min}}$ which is the maximum energy transferred to the projectiles by electromagnetic excitation. To derive the value of $\alpha_{\text{cut-off}}$, it is adjusted until the peaks corresponding to these reaction channels vanish in the spectra.

No matter how the scaling factor α was derived the CD cross section is derived from the different reaction probabilities by

$$\sigma_{CD} = \left(\frac{M_{\text{Pb}}}{d_{\text{Pb}}N_A} \right) P_{\text{Pb}} - \alpha \left(\frac{M_{\text{C}}}{d_{\text{C}}N_A} \right) P_{\text{C}} - \left(\frac{M_{\text{Pb}}}{d_{\text{Pb}}N_A} - \alpha \left(\frac{M_{\text{C}}}{d_{\text{C}}N_A} \right) \right) P_{\text{empty}} \quad (5.21)$$

with the molar masses M_i and thicknesses d_i of the lead and carbon targets, respectively.

Experimental setup at GSI, Darmstadt, Germany An experimental setup to perform measurements in complete kinematics is available at GSI Helmholtzzentrum für Schwerionenforschung GmbH (GSI), Darmstadt, Germany. It was sometimes named by the dipole magnet separating the outgoing particles by their mass-to-charge ratio and the neutron detector: ALADiN-LAND setup. At the upcoming accelerator complex FAIR, Darmstadt, Germany, this setup will be extended to match the higher beam intensities and beam energies to be delivered. At its final stage, the setup will be called R³B describing the fact that Reactions with Relativistic Radioactive Beams will be studied. Meanwhile, the various detection systems undergo upgrades or are newly built. Therefore, the current status of the setup is referred to as LAND-R³B setup at times. Figure 5.29 depicts schematically the accelerator complex at GSI, Darmstadt, Germany [160]. The UNiVersal Linac ACcelerator (UNILAC) provides the primary beam with

energies up to 10 MeV/nucleon. It is delivered to the heavy-ion synchrotron SIS where energies up to 1 GeV/nucleon and intensities of about 10^{10} ions/s are reached depending on the accelerated nuclei. Radioactive beams are produced by the in-flight method using a Be production target with a thickness of 4 g/cm^2 for fragmentation of the primary beam particles. The fragment separator FRS [161] is used to select the fragments of interest according to their magnetic rigidity. Furthermore, scintillation detectors as indicated by S2 and S8 in the inlay of Fig. 5.29 are placed in the FRS beam-line to determine the masses of the fragments by time-of-flight measurements.

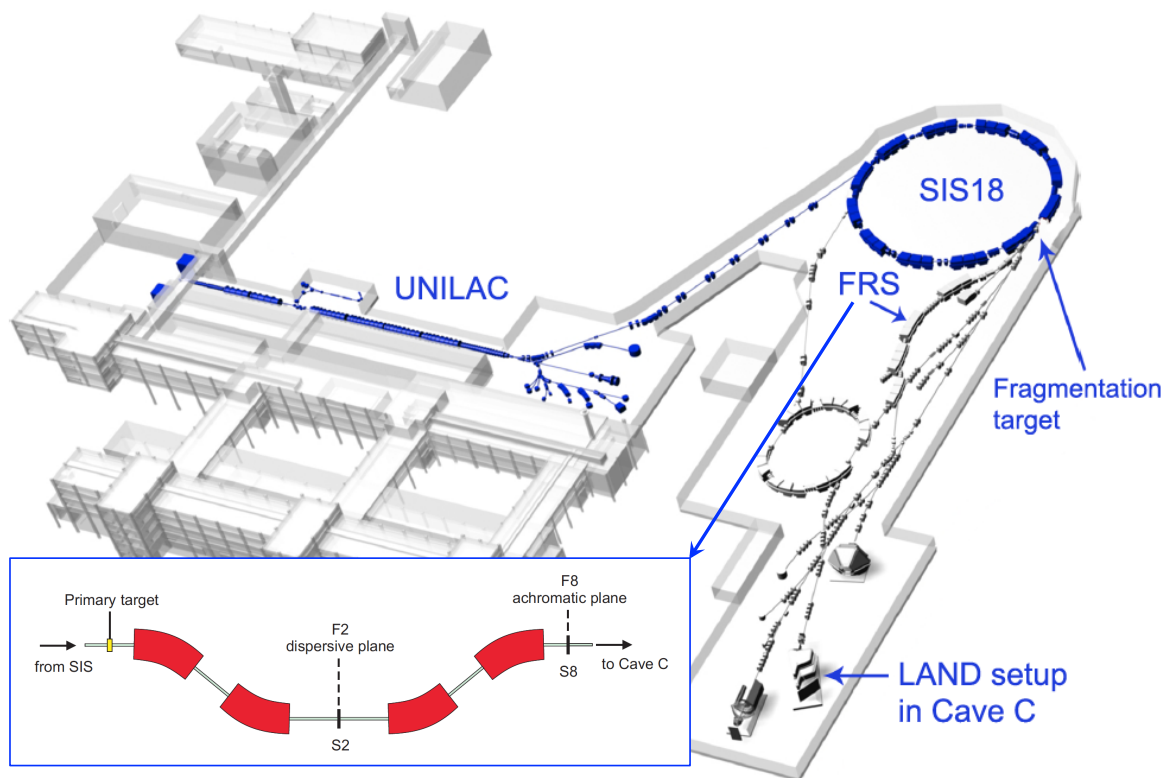


Figure 5.29:

Overview of the accelerator facility at GSI, Darmstadt, Germany. The UNILAC accelerates the primary beams which are further accelerated in SIS18. The radioactive ion beam is created in-flight by fragmentation. The FRS sorts the species of interest out and delivers the beam to the experimental setup in Cave C. The inlay shows the position of two scintillator detectors S2 and S8 in the FRS. Composed from [160].

An ALADiN-LAND setup is exemplarily shown in Fig. 5.30. Besides ALADiN and LAND, the detectors are usually varied to optimize detection efficiency and energy resolution. Therefore, the combination used in the lateron discussed experimental campaign S295 is presented here. Although the detection systems varies from experiment to ex-

periment, the main purposes of the setup persist: identification of incoming particles (incoming ID), measurement of prompt γ rays, separation of neutrons and fragments (ALADiN), measurement of neutrons (LAND), and measurement of heavy fragments.

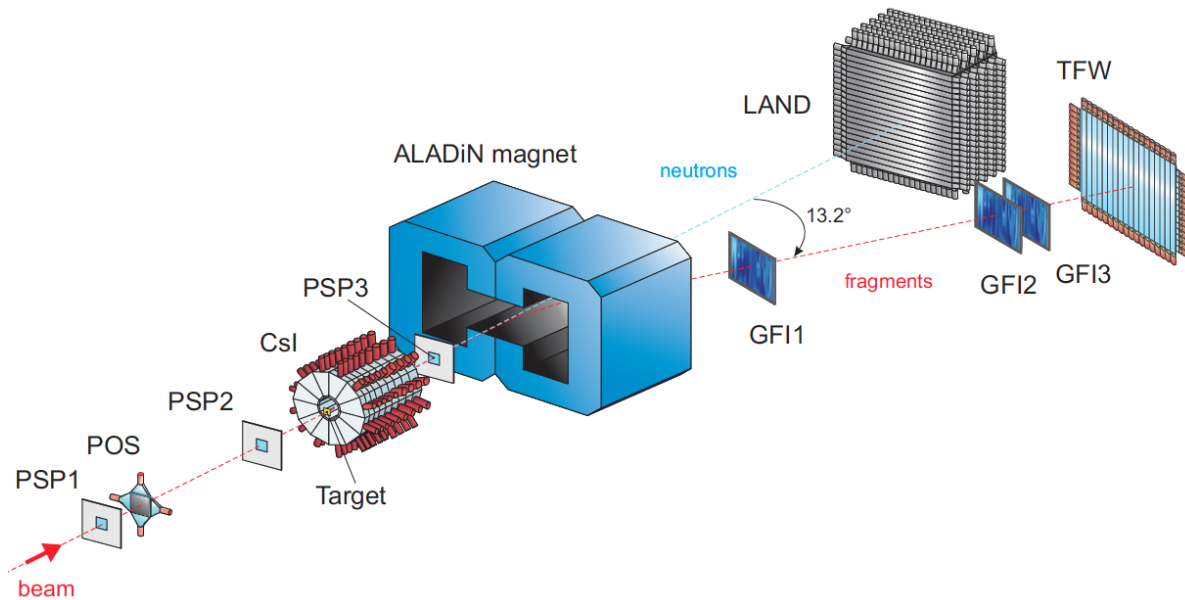


Figure 5.30:

Example of an ALADiN-LAND experimental setup (not to scale). The basic components are the ALADiN magnet for the separation of neutrons and fragments and the LAND detector for the observation of neutrons. Together with S2 and S8 (see Fig. 5.29), the detectors PSP1, POS, and PSP2 provide the identification of incoming particles. The CsI detector surrounds the target and provides information about prompt γ rays. The heavy fragments are tracked and identified in the so-called fragment arm consisting of GFI1, GFI2, GFI3, and TFW. Taken from [160].

The POS detector is a thin, square-shaped plastic scintillator detector which is read out by four photomultipliers and used to measure the time-of-flight with start signals from S2 and S8. In front and behind the target, the position of the beam is determined by Si pin-diodes called PSP in Fig. 5.30. The dimension of the beam spot and its emittance is defined by a system of active slits called ROLU [162] located between PSP2 and the target. The Pb target is placed at the beginning of the CsI detector [163, 164] which is used to measure the γ rays being emitted by the excited projectiles. Each of the single crystals covers a solid angle which is defined by the aim to realize the Doppler correction by suitable amplifications of the single signals. Thus, the energy of the emitted photons in the rest frame of the emitting source can be measured directly.

A large gap dipole magnet (ALADiN [165]) separates the charged fragments and the neutrons emitted in the reaction. To determine the trajectories of the charged fragments,

another Si pin-diode before the magnet (PSP3 in Fig. 5.30 and several large-area fiber detectors [166] behind the magnet are used. By defining the deflection angle in the magnetic dipole field, the magnetic rigidity of the particle is fixed and, thus, its mass-to-charge ratio. The Time-of-Flight Wall (TFW in Fig. 5.30 determines the charge of a fragment by measuring its energy loss. It can also provide information about its velocity if another POS-type detector is placed close to the target.

The LAND neutron detector [167] provides with its $2 \times 2 \text{ m}^2$ active area a 100% acceptance for the emitted neutrons with kinetic energies up to 5.6 MeV. Using the two far-end sides of the one meter thick detector array time-of-flight and position information is available. A detailed description of this setup is given in [160].

In the experimental campaign S295, the (γ, n) cross sections of the isotopes $^{92,93,94,100}\text{Mo}$ should be derived from the corresponding CD cross sections [168]. To study the stable isotopes ^{94}Mo and ^{100}Mo the corresponding beams were delivered as primary beams by the synchrotron SIS. The beam of ^{93}Mo and ^{92}Mo nuclei was produced by a primary ^{94}Mo beam via one and two neutron removal, respectively. However, the cross sections of these two isotopes have been measured one after the other due to an easier analysis. As the analysis of the CD experiment on ^{94}Mo is still ongoing [169], the fundamental steps will be described using the analysis presented in [160] as an illustrating example. The thesis work [160] and the results presented therein are not part of this work.

Fundamental steps of the analysis To determine the CD cross section from the measured data, several fundamental steps are needed in the analysis. In detail and complexity, they can vary significantly depending on factors like, *e.g.*, the usage of primary or secondary beams.

Generally, the desired reaction channel is chosen from a variety of reactions present in the data due to the high energy of the beam and due to its mixed composition. At first, the identification of the incoming particles is performed by a combination of time-of-flight and energy-loss measurements. The time-of-flight stems from a correlation of the FRS detectors S2 and S8 with the POS detector and provides the mass-to-charge ratio of a particle. The charge is known from its energy loss in the PSP detectors. A typical result for a secondary beam is shown in Fig. 5.31a).

The second and more complex step is the determination of the outgoing channel. Here, several cuts which determine certain conditions for the different detectors must be applied and combined. If absolute data on a cross section is needed the knowledge about the efficiency of these cuts as well as about the introduced systematic deviations is crucial but not easily determinable. *E.g.*, a cut on a one-neutron event in LAND misses some events as the detection efficiency is only close to 100% but, for the same reason, two-neutron events might be counted as one-neutron events. Therefore, these efficiencies usually stem from extensive simulations of the given experimental situation as discussed in [170].

LAND is very commonly used to determine the outgoing channel as it either provides

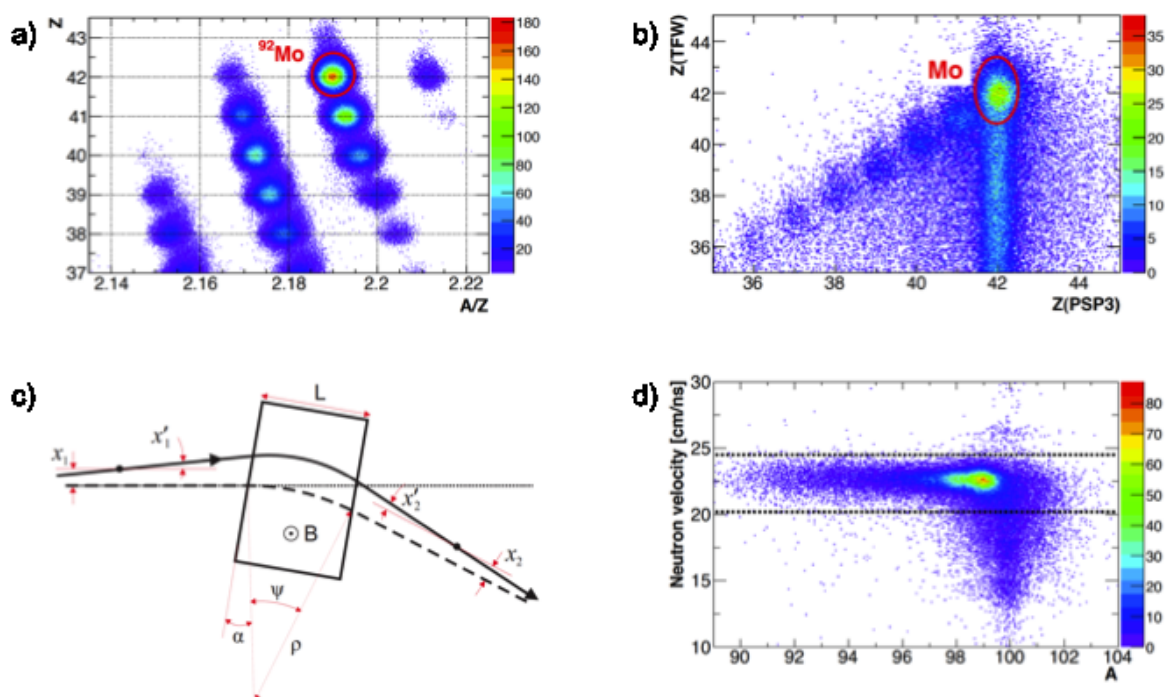


Figure 5.31:

Fundamental steps of analyzing data of Coulomb Dissociation measured at ALADiN-LAND setup. a) Identification of incoming particle. The charge Z is determined from the energy loss of the particle in detectors PSP1 and PSP2 (see Fig. 5.30). The mass-to-charge ratio A/Z stems from a time-of-flight measurement between detectors placed at the FRS (S2, S8 in Fig. 5.29) and the POS detector in Cave C. b) Determination of charge Z in outgoing reaction channel. The energy loss in PSP3 and TFW is compared and an elliptical cut on molybdenum is used. c) Illustration of tracking procedure. The mass-to-charge ratio in the outgoing reaction channel stems from the magnetic rigidity of the particle in ALADiN. Its track is determined from its positions in detectors in front of ALADiN (*e.g.*, PSP3) and behind ALADiN (*e.g.*, GFI1). d) Velocity cut for neutrons detected by LAND. The velocity is deduced from a time-of-flight measurement and has to be within a certain range (marked with dashed lines) if the neutrons stem from a reaction at the target position. Composed from [160].

cuts on the neutron multiplicity or is used as a veto if no neutrons occur in the outgoing channel. To avoid contributions from scattered neutrons, a velocity cut must be applied as shown in Fig. 5.31d). The number of heavy fragments stems from the detectors in the so-called fragment arm. The charge Z is determined by the energy loss, *e.g.*, in the TFW and PSP3 (see Fig. 5.31 b). The mass-to-charge ratio is deduced from a tracking procedure for which the positions measured in PSP3 in front of ALADiN and in the GFI detectors behind ALADiN are used. As shown in Fig. 5.31c), possible flight paths

are reconstructed and, using a field map of ALADiN, the magnetic rigidity yields the mass-to-charge ratio.

To extract the energy dependence of the CD cross section, the data must be interpreted as a function of the excitation energy E^* . For each event fulfilling the constraints on the incoming particle and chosen reaction channel, the excitation energy E^* is calculated with Eq. (5.17). As described in detail in [160], the CsI detector caused severe problems in the analysis as its efficiency could not be determined unambiguously for the complete energy range. Therefore, the energy emitted by prompt γ rays denoted E_γ in Eq. (5.17) was not available and the results of the experimental campaign S295 are limited to integral cross sections. To compare these values with results stemming from experiments using real photons [171], the E1 and E2 components of the cross section σ_γ were calculated from systematics of giant quadrupole resonances in molybdenum isotopes [172]. As shown in Fig. 5.32, a convolution with the corresponding virtual photon spectra yields the expected CD cross section σ_{CD}^{exp} .

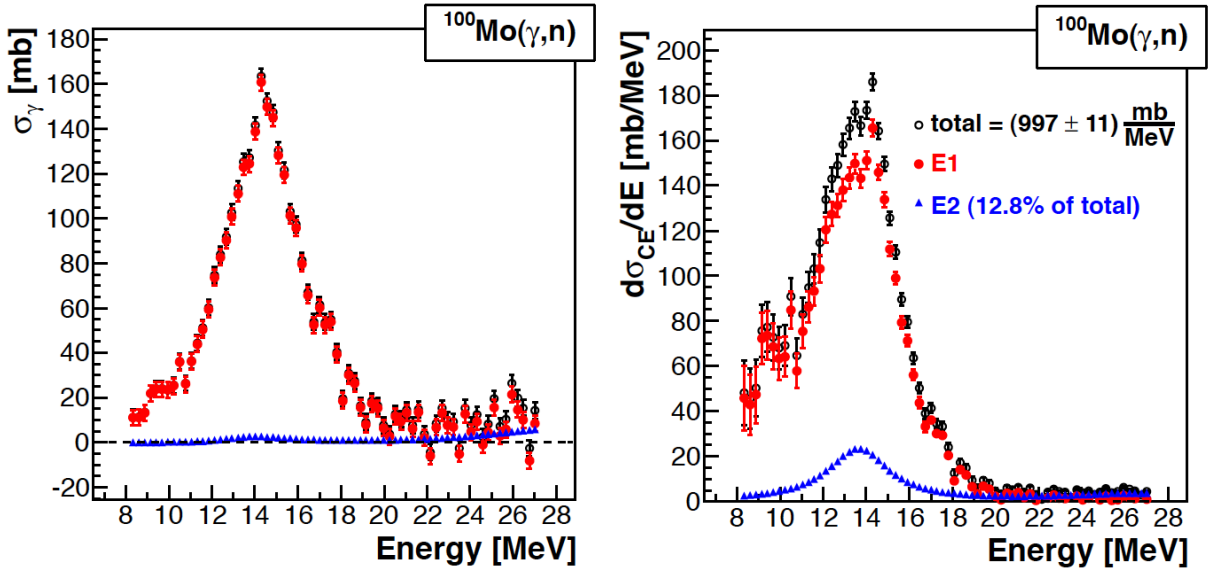


Figure 5.32:

Determination of CD cross section based on the data by Beil *et al.* [171]. *left*: The total photoabsorption cross section σ_γ (black) is splitted to an E1 component (red) and an E2 component (blue) based on systematics in the molybdenum region [172]. *right*: A CD cross section σ_{CD}^{exp} is derived by a convolution with the virtual photon spectra shown in Fig. 5.28. Composed from [160].

Applying this method, an integral CD cross section of (997 ± 61) mb results for the reaction $^{100}\text{Mo}(\gamma, n)$. A scaling factor of (0.8 ± 0.1) is needed to match the value of (799 ± 81) mb derived from the experimental data of campaign S295. This factor is within a well-known correction for results of the Saclay group and stems from the efficiency of their neutron detector [173]. It was also reported by other measurements with real

photons in this mass region [174, 175]. Thus, a reliable agreement for the integral cross section derived from Coulomb dissociation and experiments with real photons was found.

6

Consequences for p-process nucleosynthesis

This chapter focusses on the question how experimental results influence our picture of the processes contributing to the nucleosynthesis of the p nuclei. As in the previous chapter, two different approaches are presented. At first, general findings related to systematic experimental studies and the overall production of the p nuclei are presented. Afterwards, the role of key reactions for the production of the most abundant p nucleus ^{92}Mo is discussed as an example how the knowledge about such key reactions can alter our understanding of the importance of different production sites and scenarios of the p nuclei.

6.1 General remarks

As already explained in detail in Chap. 2, there is a number of processes related to a bunch of astrophysical sites where conditions occur to produce the p nuclei from different seed distributions. All in common is the explosive character, *i.e.*, the processes occur on short timescales with high temperatures and span a broad part of the chart of nuclei including a number of radioactive isotopes. Only one process is able to produce all known p nuclei from the lightest one, ^{74}Se , up to the heaviest one, ^{196}Hg . However, the γ process fails in reproducing the p nuclei in correct ratios even though nuclear uncertainties are taken into account (compare Fig. 2.6).

As these uncertainties were derived from the usage of different nuclear input to Hauser-Feshbach based calculations of cross sections it is important to check experimentally whether the used nuclear input provides reliable data across the part of the chart of nuclei which is covered by the γ process, *i.e.*, stable and proton-rich isotopes with mass numbers between about 70 and 210. This is realized in systematic investigations similar to those introduced in Subsecs. 5.1.1 and 5.2.1. Based on such studies, it is nowadays known that the predicted reaction rates are reliable within a factor of 3 if neutrons or protons occur as projectiles or ejectiles and factors up to 10 if α particles are involved [22]. These numbers are valid for so-called global nuclear input, *i.e.*, parameterized functions fitted to the available experimental data in the complete mass range covered by the γ process.

Therefore, the need of broader data bases especially in the case of reactions involving α particles is obvious to reduce these uncertainties. However, it is not yet clear whether all nuclear aspects are taken into account sufficiently in the parameterized functions serving as base of the global input. This might be well-known but as yet not well-describable nuclear aspects like, *e.g.*, the influence of closed neutron or proton shells on level densities or parity distributions. In addition, there might be some hidden traps in the fitting process itself when the reaction mechanism is not fully described. A recent example is the assumption that the deviations for reactions including α particles stem from so-called sub-Coulomb excitation [139]. As the influence of this effect is coupled to low-energy E2 excited states it is mandatory to improve the knowledge about this nuclear structure data in combination with measured cross sections to test this assumption. Another approach for a test is the investigation of reactions with α particles as ejectiles as in [176].

As the nuclear uncertainties are an undebatable fact their influence on branchings of the γ process was tested in [22]. As explained in Chap. 2, a branching of the γ process is indicated when the (γ,p) and/or (γ,α) reaction rates is comparable to the (γ,n) reaction rate. In the low-mass region, these branchings occur near or even at the valley of stability and usually for (γ,p) reactions. In the high-mass region, branchings are dominated by (γ,α) reactions occurring four to eight mass units off the valley of stability [17]. As the location of the branchings determines the mass number for which a lighter element is reached and, thus, the abundance ratios of the *p* nuclei it is important to constrain their location. Therefore, the reactions with the highest impact on the location of branchings were extracted in [22] and recommended for experimental studies to get rid of the uncertainties stemming from the global nuclear input. Some of these reactions are only accessible using radioactive ion beams (compare Tab. 6.1).

Another approach to determine key reactions in huge reaction networks is the brute-force method of varying a certain type of reaction rates by a given factor and compare their influence on the final abundance distribution. This was performed in [23]. In this case, the influence of systematic uncertainties related to a certain type of reaction rates is determined. In addition, a benchmark is derived which uncertainties do not generally change the final abundance distribution. As listed in Tab. 6.1, the overlap of the reaction rates found in [22] and [23] is limited to four reactions: $^{92}\text{Mo}(\alpha,\gamma)^{96}\text{Ru}$, $^{102}\text{Pd}(\alpha,\gamma)^{106}\text{Cd}$, $^{116}\text{Sn}(\alpha,\gamma)^{120}\text{Te}$, and $^{124}\text{Xe}(\alpha,\gamma)^{128}\text{Ba}$. It is remarkable that both a neutron-magic nucleus (^{92}Mo , $N = 50$) and a proton-magic nucleus (^{116}Sn , $Z = 50$) are included. Thus, independent of the approach, nuclear structure seems to be of some importance. In combination, these studies showed that there is indeed a set of key reactions for the γ process highlighting roughly 50 reactions out of the 10,000 reactions involved in the network calculation.

References [22] and [23] were published in 2006. Since then, a number of the recommended reactions were investigated experimentally or – like in the case of $^{91}\text{Nb}(p,\gamma)$ – are to be investigated soon. Therefore, Tab. 6.1 comments on the current status of experimental investigation emphasizing already published results (method and reference).

Table 6.1:

Most important reaction rates in the γ process. Two different approaches led to a set of key reactions of the γ process which were recommended for experimental investigation by [22] with highest priority or [23]. The reactions recommended in both publications are highlighted in bold font. The entries in the columns are sorted by the mass number of the target isotope. Note that in case of radiative capture the inverse reaction usually plays the important role in the γ process (compare Sec. 5.1). As comments, either the current status of experimental investigation is listed or the half-lives of involved unstable isotopes.

Ref. [22]	comment	Ref. [23]	comment
$^{76}\text{Se}(\alpha,\gamma)$	in progress [108]	$^{70}\text{Ge}(\alpha,\gamma)$	
$^{79}\text{Br}(\text{p},\gamma)$		$^{71}\text{Ge}(\text{n},\text{p})$	neutron counting [177] ^a
$^{80}\text{Se}(\text{p},\gamma)$	γ spectroscopy [178]	$^{72}\text{Ge}(\text{p},\gamma)$	
$^{84}\text{Kr}(\text{p},\gamma)$		$^{74}\text{Ge}(\text{p},\gamma)$	γ spectroscopy [99]
$^{89}\text{Y}(\text{p},\gamma)$	γ spectroscopy [179]		4π summing [180]
	4π summing [181]	$^{76}\text{As}(\text{n},\text{p})$	activation [124] ^a
$^{92}\text{Mo}(\alpha,\gamma)$	4π summing [182]	$^{73}\text{As}(\text{p},\gamma)$ ^b	$t_{1/2} = 80.3$ d
$^{93}\text{Nb}(\text{p},\gamma)$	γ spectroscopy [183]	$^{75}\text{Se}(\text{n},\text{p})$	neutron counting [177] ^a
$^{94}\text{Mo}(\alpha,\gamma)$		$^{77}\text{Se}(\text{n},\text{p})$	
$^{96}\text{Ru}(\alpha,\gamma)$		$^{77}\text{Br}(\text{p},\gamma)$ ^b	$t_{1/2} = 57.0$ h
$^{97}\text{Tc}(\text{p},\gamma)$	$t_{1/2} = 4 \cdot 10^6$ a	$^{83}\text{Rb}(\text{p},\gamma)$ ^b	$t_{1/2} = 86.2$ d
$^{98}\text{Ru}(\alpha,\gamma)$		$^{85}\text{Sr}(\text{n},\text{p})$	activation [184] ^a
$^{102}\text{Pd}(\alpha,\gamma)$		$^{86}\text{Rb}(\text{n},\text{p})$	$t_{1/2} = 18.7$ d
$^{108}\text{Cd}(\alpha,\gamma)$		$^{91}\text{Nb}(\text{p},\gamma)$ ^b	this work
$^{110}\text{Cd}(\text{p},\gamma)$		$^{92}\text{Mo}(\alpha,\gamma)$	4π summing [182]
$^{116}\text{Sn}(\alpha,\gamma)$	4π summing [182] ^c	$^{95}\text{Tc}(\text{p},\gamma)$	$t_{1/2} = 20$ h
$^{118}\text{Sn}(\text{p},\gamma)$		$^{99}\text{Rh}(\text{p},\gamma)$	$t_{1/2} = 16$ d
$^{124}\text{Xe}(\alpha,\gamma)$		$^{102}\text{Pd}(\alpha,\gamma)$	
$^{128}\text{Xe}(\text{p},\gamma)$		$^{103}\text{Ag}(\text{p},\gamma)$	$t_{1/2} = 1.1$ h
$^{130}\text{Ba}(\alpha,\gamma)$	activation [185]	$^{105}\text{Ag}(\text{p},\gamma)$	$t_{1/2} = 41.29$ d
$^{134}\text{Ba}(\text{p},\gamma)$		$^{106}\text{Cd}(\alpha,\gamma)$	activation [186]
$^{138}\text{Ce}(\text{p},\gamma)$		$^{109}\text{In}(\text{p},\gamma)$	$t_{1/2} = 4.167(18)$ h [187]
$^{141}\text{Pr}(\alpha,\gamma)$	activation [120] ^d	$^{116}\text{Sn}(\alpha,\gamma)$	4π summing [182] ^c
$^{148}\text{Sm}(\alpha,\gamma)$		$^{118}\text{Te}(\alpha,\gamma)$	$t_{1/2} = 6$ d
$^{150}\text{Gd}(\alpha,\gamma)$	$t_{1/2} = 1.8 \cdot 10^6$ a	$^{124}\text{Xe}(\alpha,\gamma)$	
$^{152}\text{Gd}(\alpha,\gamma)$		$^{125}\text{Cs}(\text{p},\gamma)$	$t_{1/2} = 45$ m
$^{154}\text{Dy}(\alpha,\gamma)$	$t_{1/2} = 3 \cdot 10^6$ a	$^{163}\text{Yb}(\alpha,\gamma)$	$t_{1/2} = 11.1$ m
$^{168}\text{Yb}(\alpha,\gamma)$	activation [82]	$^{192}\text{Hg}(\alpha,\gamma)$	$t_{1/2} = 4.9$ h
$^{174}\text{Hf}(\alpha,\gamma)$			

^a derived from measurement of inverse reaction^b reaction relevant for proton-capture chain (see [19] and [20])^c no particular results shown^d derived from measurement of $^{141}\text{Pr}(\alpha,\text{n})$ reaction

6.2 The production of ^{92}Mo

As explained in Chap. 2, the p nuclei of molybdenum and ruthenium are tremendously underproduced in the γ process occurring during type II supernovae [22, 23]. Therefore, an additional astrophysical site for the γ process or an additional production process have to be considered to reproduce the observed solar abundances. Instead of changing reaction rates in the complete reaction network and looking at the consequences for the abundances it is also possible to apply local changes, *i.e.*, only the rates of reactions in the neighbourhood of the p nucleus of interest are varied. Then, more detailed investigations of the influence of these reactions is possible as the amount of data remains manageable. We performed such variations for the molybdenum and ruthenium p nuclei [169] and used trajectories or tracers derived for a type II supernova (similar to [22, 23]) and for a type Ia supernova (similar to [20]). As an independent tool compared to previous studies, the Post-Processing Nucleosynthesis (PPN) simulation framework provided by the Nucleosynthesis Grid (NuGrid) research platform [188] is used. NuGrid offers trajectories or tracers obtained from simulations of stellar evolution with only energy-producing nuclear reactions included [189, 190]. The PPN studies can use these data or import similar information from other sources to solve a large reaction network including more than 5,000 isotopes. The information about the rates of the corresponding 60,000 reactions can be extracted from different nuclear data sets. In this work, the Basel Reaction Library (REACLIB) [191] and the JINA Reaclib Database V1.1 [192] were used. The complete investigation for $^{92,94}\text{Mo}$ and $^{96,98}\text{Ru}$ is explained in detail with a variety of illustrations in [169]. In this work, the results for ^{92}Mo are summarized and discussed.

PPN simulations for type II supernova model For type II supernova, the Hashimoto trajectories for fourteen different layers as already used in previous studies [17, 22, 23] were the input for the PPN simulations. These trajectories contain the evolution of temperature in time and of density in time in the different layers. The innermost layer experiences the highest peak temperature at the earliest time. Very rapidly, the peak temperature is reached from a base temperature. Afterwards, an exponential decay occurs. This behaviour is general for all layers although both the base and peak temperature decrease in the outer regions. The peak temperatures range from about 2 GK to 3 GK. The density profiles are of similar shape and cover a range of $2 \cdot 10^5 \text{g/cm}^2$ to $6 \cdot 10^5 \text{g/cm}^2$ (compare Chap. 2).

The overall production and destruction of isotopes during the post-processed event are displayed using time-integrated fluxes f . The flux f is determined by the rate of the nuclear reaction r and the abundance of the target nuclei N_t at a certain time [189, 190]. Their absolute values illustrate the importance of a certain reaction path in the network calculation. If the fluxes of all production and destruction reactions, f_{prod} and f_{destr} , respectively, are evaluated relatively to each other, the difference represents the net abundance yield of the simulation. To derive meaningful values, the sum of all production fluxes is normalized to 100% and the normalization factor is also used for

the destruction fluxes. The difference $f_{\text{prod}} - f_{\text{destr}}$ indicates that the abundance of the considered isotope increases during the PPN if the sign is positive and vice versa. The absolute net production can be derived using the abundance of the isotope available in the seed distribution. To constrain the illustrated information to a reasonable amount, the fluxes below a chosen percentage are cut off. In this work, a cut-off value of 1% was chosen.

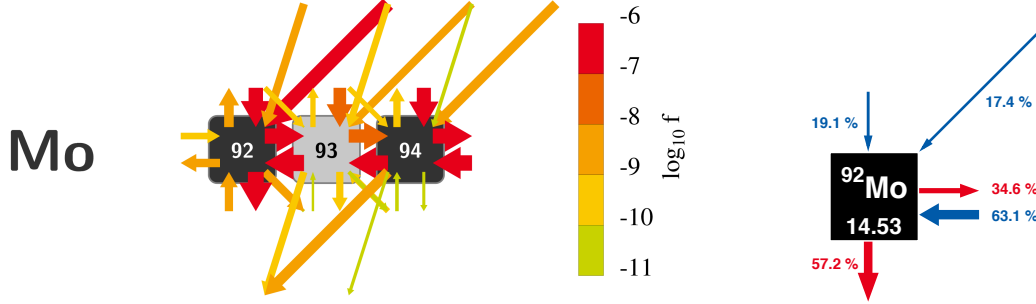


Figure 6.1:

Time-integrated production and destruction fluxes of type II supernova. *left*: Time-integrated fluxes for ^{92}Mo , ^{93}Mo , and ^{94}Mo . Colors indicate the order of magnitude of the flux and the thickness of the arrows scales linearly with $\log_{10} f$. *right*: Normalized time-integrated fluxes for ^{92}Mo . The arrows indicating production fluxes f_{prod} (blue) and destruction fluxes f_{destr} (red), respectively, scale linearly with the percentage. For details, see text. Data from [169].

The time-integrated absolute fluxes f in the isotopic chain are dominated by (γ, n) and (n, γ) reactions which are in the same order of magnitude for ^{95}Mo to ^{100}Mo . Therefore, no significant net production is expected for these isotopes. For the p nuclei ^{92}Mo and ^{94}Mo , the situation is different since more reactions provide significant fluxes and the situation becomes rather crowded as shown in Fig. 6.1. Therefore, the normalized time-integrated fluxes for ^{92}Mo are also shown. The main production flux of $f_{\text{prod}} = 63.1\%$ stems from the $^{93}\text{Mo}(\gamma, n)$ reaction although the abundance of ^{93}Mo ($t_{1/2} = 4000$ a) has to be fed first. The reactions $^{96}\text{Ru}(\gamma, \alpha)$ and $^{93}\text{Tc}(\gamma, p)$ contribute to the abundance of ^{92}Mo similarly ($f_{\text{prod}} = 17.4\%$ and 19.1% , respectively). The destruction is due to the reactions $^{92}\text{Mo}(\gamma, p)$ and $^{92}\text{Mo}(n, \gamma)$ with fluxes of $f_{\text{destr}} = 57.2\%$ and 34.6% , respectively.

However, these values do not represent the importance of a reaction rate on their own as the fluxes also rely on the abundances of the target nuclei. Therefore, sensitivity studies were performed with the reaction rates being varied within the uncertainties stated in [22]. The rate of reactions including a neutron or a proton was scaled with factors 0.2, 0.5, 2, and 5 while factors of 0.1, 0.2, 5, and 10 were applied for reactions including an α particle. The sensitivity s is defined as the ratio of the relative change of the input variable and the relative change of the output variable. In our case, the change

of the reaction rate r/r_{REF} must be compared to the change of the isotopic abundance N/N_{REF} . Usually, a linear correlation is expected, *i.e.*,

$$s = \frac{r/r_{\text{REF}}}{N/N_{\text{REF}}} = \text{const.}, \quad (6.1)$$

and the change of the abundance can be predicted from the change of the rate. If the correlation of an isotopic abundance to a certain reaction rate is known and, *e.g.*, a new experimental rate becomes available, the corresponding new isotopic abundance is known without performing another PPN study. However, not all reactions producing and destroying the *p* nucleus ^{92}Mo and changing the ^{92}Mo abundance by more than 5% within the applied rate variations behave like this.

The reactions complying with the applied cut-off condition are not the same ones as those yielding a relative flux above 1%. Firstly, the reaction $^{93}\text{Tc}(\gamma, \text{p})$ with $f_{\text{prod}} = 19.1\%$ is not depicted in the sensitivity study as its influence for the relative flux stems from the abundance of ^{93}Tc ($t_{1/2} = 2.75$ h) which has to be produced by photodisintegration of ruthenium isotopes first. Secondly, reactions are considered which do not directly produce or destroy ^{92}Mo but change the reaction path towards or away ^{92}Mo . The $^{94}\text{Mo}(\gamma, \alpha)$ reaction bypasses ^{92}Mo and directly feeds ^{90}Zr . Therefore, the ^{92}Mo abundance is decreased with the corresponding rate being increased. In contrast, the $^{98}\text{Ru}(\gamma, \text{n})$ reaction increases the amount of ^{96}Ru being available. Thus, an increased rate results in a slightly increased ^{92}Mo abundance. In case of the $^{94}\text{Mo}(\text{n}, \gamma)$ reaction, an increase of the rate also results in an increase of the ^{92}Mo abundance although the reaction path is changed away of ^{92}Mo . Here, the reduction of neutrons being available for the destruction reaction $^{92}\text{Mo}(\text{n}, \gamma)$ is an explanation.

The reaction $^{92}\text{Mo}(\gamma, \text{p})$ with the highest destruction flux $f_{\text{destr}} = 57.2\%$ shows the highest sensitivity of all reactions although the relative flux of the most important production reaction $^{93}\text{Mo}(\gamma, \text{n})$ is higher ($f_{\text{prod}} = 63.1\%$). To understand this behaviour, the inclusion of the $^{94}\text{Mo}(\gamma, \text{n})$ reaction is necessary as this reaction initially produces the unstable ^{93}Mo isotope ($t_{1/2} = 4000$ a). Indeed, the photo-neutron reaction of ^{94}Mo has the highest constructive sensitivity and, in combination with the constructive sensitivity of the $^{93}\text{Mo}(\gamma, \text{n})$ reaction similar values result as for the $^{92}\text{Mo}(\gamma, \text{p})$ reaction.

So far, the results of the complete type II supernova model were discussed. Though, the conditions in the integrated fourteen layers are very different (compare, *e.g.*, [17]) and there might be different trends if the layers are observed separately. For comparison, the innermost layer with Hashimoto trajectory 1 and two midway layers with Hashimoto trajectory 4 and 5 are considered in the following. First, the mass fractions as a function of time for the isotopes related to the final abundance of ^{92}Mo as well as for protons and neutrons are discussed. The amount of free protons and neutrons is reduced by two orders of magnitude in the midway layer 4 since, in total, less photodisintegration reactions occur due to the lower temperatures. For both layers, the abundances of the molybdenum and ruthenium isotopes achieve an equilibrium right after the peak

temperature is reached, *i.e.*, production and destruction reactions cancel each other. As expected, the abundance of ^{92}Mo is increased in both layers. However, this increase is less pronounced in the innermost layer and, astonishingly, the p nucleus ^{94}Mo is even destroyed.

The relative time-integrated fluxes in the innermost layer 1 and the midway layer 5 provide an explanation (see Fig. 6.2). The high temperature in the innermost layer allows for an efficient destruction of ^{92}Mo by the $^{92}\text{Mo}(\gamma,p)$ reaction. The destruction flux in this layer is with $f_{\text{destr}} = 66.8\%$ almost 10% higher compared to the flux in the complete model. In contrast, the main production flux by the $^{93}\text{Mo}(\gamma,n)$ reaction is reduced about 5%. This situation changes dramatically if the outer layers are taken into account. In the midway layer corresponding to Hashimoto trajectory 5, the reaction $^{92}\text{Mo}(\gamma,n)$ provides the only relative destruction flux higher than 1%. In addition to the dominating production flux by the $^{93}\text{Mo}(\gamma,n)$ reaction, proton-induced reactions on niobium isotopes like $^{91}\text{Nb}(p,\gamma)$ and $^{92}\text{Nb}(p,n)$ start to contribute significantly with $f_{\text{prod}} = 6.5\%$ and 1.8% , respectively.



Figure 6.2:

Normalized time-integrated fluxes of ^{92}Mo for different Hashimoto trajectories. As in Fig. 6.1, the production f_{prod} (blue) and destruction fluxes f_{destr} (red) are shown for *left*: the innermost layer 1 and *right*: a midway layer 5. For details, see text. Data from [169].

Therefore, the experimental investigation of the $^{91}\text{Nb}(p,\gamma)$ reaction as described in Subsec. 5.1.2 yields important information to understand the production of ^{92}Mo in a type II supernova model for a $25 M_{\odot}$. On the one hand, the reaction provides a significant production flux in the outer layers. On the other hand, the inverse $^{92}\text{Mo}(\gamma,p)$ reaction supplies the most important destruction flux in the inner layers. As the astrophysical rates of photon-induced reactions are usually deduced from the inverse radiative particle-induced reaction (compare Sec. 5.1) the influence of the experimental data will be twofold in terms of production and destruction fluxes and general in terms of the application at different layers of the type II supernova model.

PPN simulations for type Ia supernova model The temperature and density profiles stem from a two-dimensional delayed detonation model of a White Dwarf accreting material from a main-sequence or evolved companion star and eventually overcoming the Chandrasekhar mass. The astrophysical model is described in detail in [193] while the usage of tracer particles for the determination of characteristic temperature and density profiles is explained in [194]. So far, we used two profiles of the 4,624 ones derived for the general study described in [20]. The profiles were chosen from a smaller set providing maximum production of the *p* nucleus ^{92}Mo . The set was further reduced by demanding a fixed peak temperature of 3.2 GK. Then, the tracer with maximum and minimum abundance of ^{92}Mo – tracer 1 and tracer 2, respectively, were selected for a detailed study.

Although the detailed study is still in progress, it is already foreseeable that the results will be similar to those for the type II supernova. *I.e.*, the $^{92}\text{Mo}(\gamma, p)$ reaction as well as the $^{91}\text{Nb}(p, \gamma)$ reaction contribute to the final abundance of ^{92}Mo in the type Ia supernova. Therefore, the need of an experimental investigation of the rates of these reactions by studying the radiative proton-capture reaction is furthermore stressed.

7

Summary and outlook

This work described the origin of the p nuclei and several experimental investigations to understand the nuclear physics responsible for their production at various astrophysical sites in different processes. The modelling of these processes relies on the rates of the nuclear reactions producing the p nuclei. Since these reaction networks consist typically of several thousand reactions with mostly unstable target nuclei theoretical predictions of the corresponding rates are performed within the framework of the Hauser-Feshbach statistical model. In addition, theoretical input is needed to determine the stellar rates which are dramatically different compared to the laboratory rates as the target nuclei exist mostly in excited states due to the high temperatures in any of the possible scenarios.

Systematic investigations aim at providing a broad data base to enhance the reliability of the nuclear physics input to the Hauser-Feshbach statistical model including nuclear masses, nuclear level densities, particle optical model potentials (OMP), and γ -ray strength functions. In this work, the investigation of proton and α -particle OMPs using (p,n) and (α ,n) reactions, respectively, is summarized. The study of the $^{165}\text{Ho}(\alpha,n)$ and $^{166}\text{Er}(\alpha,n)$ reactions [80] with the activation approach confirmed a recent correction of the α -particle OMP [120]. Similarly, the study of the $^{169}\text{Tm}(p,n)$ and $^{175}\text{Lu}(p,n)$ reactions [15] resulted in the application of a modification of the proton OMP as suggested by [124]. However, further experimental investigations are needed in both cases to establish such corrections and modifications in globally applicable particle OMPs. *E.g.*, a change with charge and mass number should be investigated and the effect of unpaired protons or neutrons must be understood.

As another example, the study of (γ ,n) reactions in a broad mass range of $140 \leq A \leq 210$ is described. The data was derived in several experimental campaigns using bremsstrahlung photons at DHIPS, Darmstadt [145]. The ground-state reaction rates were extracted from the data obtained by the activation approach and were compared to predictions within the Hauser-Feshbach statistical model. The typical uncertainty of a factor of 3 claimed for this type of reactions [22] was confirmed. However, photon-induced reactions can also provide stringent tests for the nuclear physics input to the calculations if the in-beam technique is used. An upcoming example is the applica-

tion of so-called γ -n coincidences using an extended version of the γ^3 setup [72] with Laser-Compton Backscattering photons at HI γ S. Partial cross sections of the reaction $^{87}\text{Rb}(\gamma, n)$ will be investigated [154] and shed light on the γ -ray strength function and nuclear level density as explained in [139].

Although the reaction network comprises several thousands of reactions there are of course individual reactions which influence the produced abundance pattern more than on average. For the most widely studied process for the synthesis of the p nuclei, the γ process [21], a set of such reactions is collected in Tab. 6.1 from the investigations in [22] and [23]. One of these reactions, the $^{74}\text{Se}(\alpha, \gamma)$ reaction, is currently studied at the recoil mass separator DRAGON at TRIUMF, Canada [108]. The aim is to enable the recoil mass separator which was designed for the study of the $^{15}\text{O}(\alpha, \gamma)$ reaction [107] to measure (α, γ) and (p, γ) reactions with beams up to a mass number of $A = 90$.

As explained in detail in [139], the investigation of radiative capture reactions is favoured to study the photon-induced reactions occurring in the γ process. In some cases, like the production of the most abundant p nucleus ^{92}Mo , these radiative capture reactions play themselves a significant role in the nucleosynthesis processes (compare [19, 20]). Therefore, this work also discusses the experimental investigation of the $^{90}\text{Zr}(p, \gamma)$ and $^{91}\text{Nb}(p, \gamma)$ reactions. For the previous one, data is available [127, 126, 125] and was measured [129, 131] using different experimental methods. Although the uncertainties of each measurement are rather small, systematic deviations between the data sets do not allow the exclusion of one or another nuclear physics input of predictions within Hauser-Feshbach statistical model (compare Fig. 5.14). Therefore, the identification and prevention of systematic uncertainties remains an important task for experimentalists. Completely different challenges arise if the target nucleus is unstable. In case of the $^{91}\text{Nb}(p, \gamma)$ reaction, the efforts towards the production of a target of the unstable ^{91}Nb ($t_{1/2} = 680$ a) are described in this work. As the amount of available target material will be very limited, a high-intensity proton beam is mandatory to investigate the reaction in standard kinematics. The status of design and construction of an appropriate beam line at the facility FRANZ, Frankfurt, as well as of the development of high-power resistive targets and a low-background target chamber for a 4π BaF₂ calorimeter are reported. The developments will be investigated in test experiments once a proton beam is available at FRANZ. In addition, the study of the $^{91}\text{Nb}(p, \gamma)$ reaction might become possible at DRAGON in inverse kinematics covering a somewhat lower energy range than FRANZ. Measurements at a storage ring like the ESR at GSI Helmholtzzentrum für Schwerionenforschung (GSI), Darmstadt, could yield the data to investigate the Gamow window [109] also for higher energies.

The radioactive beams provided at GSI, Darmstadt, were also used to investigate the cross sections of (γ, n) reactions at the ALADiN-LAND setup. The results for an experiment using the method of Coulomb Dissociation in inverse kinematics [168, 160]

are briefly summarized as an example in this work. The analysis of the complex data is still ongoing [169]. The upcoming R³B setup at FAIR, Darmstadt, will also allow the study of (γ ,p) reactions. The present layout of the R³B setup can be extended with tracking detectors for α particles. The corresponding efforts in detector development and optimized read-out of the data could lead to a world-wide unique setup to measure the ratios cross sections of (γ ,n), (γ ,p), and (γ , α) reaction simultaneously. Then, the experimental investigation of the branchings of the γ process is possible and provides an important step towards a complete understanding of the nucleosynthesis of the p nuclei.

8

Zusammenfassung

Die vorliegende Arbeit beschreibt experimentelle kernphysikalische Untersuchungen, die dem Verständnis der Nukleosynthese der p -Kerne in verschiedenen astrophysikalischen Szenarien und den entsprechenden Prozessen dienen. Damit ist sie im Forschungsgebiet der Nuklearen Astrophysik angesiedelt, dass sich seit dem Erscheinen der Arbeiten von E.M. Burbidge, G.R. Burbidge, W.A. Fowler, and F. Hoyle [1], sowie unabhängig davon A.G.W. Cameron [2] im Jahr 1957 neben Fragen zur stellaren Entwicklung auch mit der Synthese der Elemente schwerpunkthaft beschäftigt.

Die leichtesten Elemente Wasserstoff und Helium werden bereits in der Primordialen Nukleosynthese direkt nach dem Urknall gebildet [3]. In Sternen entstehen daraus durch Fusionsprozesse die Elemente bis zur Eisen-Nickel-Region. Durch die wachsende Bindungsenergie pro Nukleon wird bei diesen Reaktionen Energie frei, die als Strahlungsdruck dem Gravitationsdruck entgegen wirkt und so den Stern in einem stabilen Zustand hält [4]. Schwerere Elemente als Eisen, d.h. Elemente mit einer größeren Ladungszahl als $Z = 26$, werden durch Neutroneneinfangreaktionen und β -Zerfälle erzeugt. Man unterscheidet hier zwischen dem s -Prozess [7], der bei geringen Neutronendichten während verschiedener stellarer Entwicklungsphasen abläuft, und dem r -Prozess [6], der in einem explosiven Ereignis mit sehr hohen Temperaturen und Neutronendichten, wie z.B. einer Kernkollaps-Supernova statt findet. Bereits in den Arbeiten [1] und [2] wurde festgestellt, dass es etwa 35 Isotope auf der protonenreichen Seite des Stabilitätstals gibt, die nicht in diesen Prozessen erzeugt werden können.

Der wohl am besten untersuchte Vorschlag zur Erzeugung dieser sogenannten p -Kerne [12] ist der γ -Prozess [21], bei dem eine vorgegebene Saatverteilung, die meist der solaren Häufigkeitsverteilung (vergleiche Abb. 2.1) entspricht, einem hochenergetischen Photonenbad ausgesetzt wird. Dies kann in verschiedenen astrophysikalischen Szenarien vorliegen, denen eine sehr hohe Temperatur im Bereich einiger GK gemein ist, die gemäß der Planck-Verteilung (siehe Gl. (3.6) für eine ausreichende Anzahl von Photonen mit Energien im MeV-Bereich sorgt. Nun werden zunächst durch (γ, n) -Reaktionen immer protonenreichere Isotope gebildet, bis schließlich die Neutronenseparationsenergie so hoch wird, dass die Raten von (γ, α) - und/oder (γ, p) -Reaktionen eine ähnliche Größenordnung erreichen. An diesen sogenannten „branchings“ (dt. Verzweigungen)

führt die Reaktionskette dann zu einem leichteren Element. Nach dem raschen Abklingen der Temperatur zerfallen die noch vorliegenden β -instabilen Isotope mittels Zerfallsketten zurück zum Stabilitätstal und erzeugen so – neben Spuren anderer Isotope – die p -Kerne (siehe Abb. 2.4).

Alternative Prozesse, wie z.B. der rp -Prozess [25] oder der νp -Prozess [27], bauen die Häufigkeiten der p -Kerne durch eine Kette von Protoneneinfangreaktionen und β -Zerfällen ausgehend von leichteren Elementen auf. Diese Prozesse können aber nicht die Existenz der schweren p -Kerne jenseits der Sb-Sn-Te-Region erklären, da die stetig wachsende Coulomb-Barriere zu einer Reduktion der Protoneneinfangwahrscheinlichkeit führt und die kleiner werdenden Wirkungsquerschnitte die Prozesse stoppen [26].

Der γ -Prozess verläuft typischerweise bei Temperaturen im Bereich einiger GK und Dichten einiger 10^5 g/cm^3 und findet sowohl in Kernkollaps- als auch in thermonuklearen Supernova-Explosionen statt. Beide Szenarien tragen dazu bei, die beobachteten solaren Häufigkeiten der p -Kerne zu erzeugen.

Aus kernphysikalischer Sicht ist es für die Modellierung der Synthese der p -Kerne notwendig, die Reaktionsraten eines über einige Tausend Isotope ausgedehnten Netzwerks zu kennen. Die meisten der mehrere Zehntausende umfassenden Reaktionen finden an instabilen Kernen statt und entziehen sich der experimentellen Untersuchung. Außerdem muss die Anregung der Kerne in der heißen Umgebung berücksichtigt werden – Reaktionen am Grundzustand finden nur im Sub-Promillebereich statt [139]. Daher ist es notwendig, die Raten in einem geeigneten Modell zu berechnen. Aufgrund der hohen Niveaudichten wird dazu in der Regel das Hauser-Feshbach oder Statistische Modell [41] verwendet.

Hierbei wird die Reaktion in zwei voneinander unabhängig ablaufende Teile zerlegt. Zunächst wird ein sogenannter Compound-Kern C^* in einem hoch-angeregten Zustand aus der Reaktion des Targetkerns A und des Projektils a erzeugt. Anschließend zerfällt der Compound-Kern in das Produkt B und das Ejektil b . Die Wahrscheinlichkeit für das Auftreten eines jeden Teils wird unabhängig mit Hilfe von Transmissionskoeffizienten berechnet. Aus diesen setzt sich dann der Wirkungsquerschnitt für die Reaktion zusammen (vergleiche Gln. (3.7), (3.8) und (3.9)). In die Berechnung der Transmissionskoeffizienten gehen Informationen zu Energie, Spin und Parität der beteiligten Kernniveaus ein. Die Wechselwirkung von Teilchen wie Neutronen, Protonen oder α -Teilchen mit dem Kern wird mit Hilfe von Optischen Teilchen-Kern-Potentialen beschrieben. Im Falle von Photonen müssen Gamma-Stärkefunktionen verwendet werden. Daneben müssen Kernmassen und Niveaudichten der Kerne bekannt oder modelliert werden. Bei der Berechnung mit unterschiedlichen Codes wie z.B. SMARAGD [44] oder TALYS [46] kommen Abweichungen dadurch zustande, dass unterschiedliche Beschreibungen dieser kernphysikalischen Eingangsgrößen verwendet werden (vergleiche Tab. 3.1).

Um die Verlässlichkeit der vorhergesagten Wirkungsquerschnitte und Reaktionsraten zu verbessern, ist es notwendig, dass global anwendbare Eingangsgrößen zur Verfügung ste-

hen, die im gesamten durch die astrophysikalische Netzwerkrechnung abgedeckten Bereich der Nuklidkarte gültig sind. Dazu sind systematische Untersuchungen notwendig, die in der Regel mit Hilfe der Aktivierungsmethode durchgeführt werden. In dieser Arbeit werden die Optischen Teilchen-Kern-Potentiale für Protonen und α -Teilchen einem solchen systematischen Ansatz unterzogen. Dazu wurden aufgrund von Sensitivitätsbetrachtungen anstelle der astrophysikalisch relevanten (p,γ) - und (α,γ) -Reaktionen die (p,n) - und (α,n) -Reaktionen an den entsprechenden Targetkernen ausgewählt.

Die Reaktionen $^{165}\text{Ho}(\alpha,n)$ und $^{166}\text{Er}(\alpha,n)$ wurden mit Hilfe der Aktivierungsmethode am Institute for Structure and Nuclear Astrophysics der University of Notre Dame, Indiana, U.S.A., untersucht. Dünne metallische Folien mit natürlicher Isotopenzusammensetzung wurden mit α -Teilchen im Energiebereich von etwa 11.0 MeV bis 15.5 MeV bestrahlt. Danach wurde die Anzahl der Reaktionen gemäß der im Kapitel 5.1.1 beschriebenen Analyse aus Spektren bestimmt, in denen die im Anschluss an die β -Zerfälle der instabilen Reaktionsprodukte emittierten γ -Übergänge detektiert wurden. Die daraus gewonnenen Wirkungsquerschnitte der Reaktionen wurden mit den Vorhersagen aus dem Hauser-Feshbach-Formalismus verglichen [80]. Dabei wurde die beste Beschreibung für ein α -Kern-Potential gefunden, dass im entsprechenden Massenbereich mit Hilfe einer energieabhängigen Korrektur schon mehrfach für gute Übereinstimmung gesorgt hat [120].

Entsprechend wurden auch die Reaktionen $^{169}\text{Tm}(p,n)$ und $^{175}\text{Lu}(p,n)$ am Institute for Structure and Nuclear Astrophysics der University of Notre Dame, Indiana, U.S.A., untersucht. Die Bestrahlung erfolgte mit Protonen im Energiebereich von 3.3 MeV bis 7.0 MeV [15]. Auch hier konnte die Energieabhängigkeit der bestimmten Wirkungsquerschnitte mit einem modifizierten Protonen-Kern-Potential [124] sehr gut reproduziert werden. Allerdings war eine absolute Anpassung um einen Faktor 1.6 notwendig.

Sowohl für α -Kern-Potentiale als auch für Protonen-Kern-Potentiale sind weitere systematische Untersuchungen notwendig, damit die bisher gefundenen Korrekturen und Modifikationen in global anwendbare Potentiale münden können. So ist es z.B. notwendig zu verstehen, ob und wie sich die Korrekturen als Funktion von Massen- und Ladungszahl verhalten, aber auch ob es z.B. Abhängigkeiten in Bezug auf ungepaarte Protonen und Neutronen gibt.

Ein weiteres Beispiel für eine systematische Untersuchung ist die Messung von (γ,n) -Reaktionen im Massenbereich $140 \leq A \leq 210$. Die Daten wurden in mehreren experimentellen Kampagnen am DHIPS-Aufbau [145] der Technischen Universität Darmstadt gewonnenen. Dabei werden Targets mit natürlicher Isotopenzusammensetzung mit einem Bremsstrahlungsspektrum aktiviert. Durch die Verwendung unterschiedlicher Endpunktsenergien ist es möglich, die Reaktionsrate des Grundzustands des untersuchten Isotops direkt zu bestimmen, ohne den Wirkungsquerschnitt aus den experimentellen Daten zu extrahieren. In den Tabn. 5.6 und 5.7 sind alle Reaktionen aufgeführt, die am DHIPS-Aufbau untersucht wurden. Für die Vorhersage der Raten von (γ,n) -Reaktionen wird eine Unsicherheit eines Faktors 3 angegeben [22]. Beim Vergleich der ex-

perimentellen Daten mit den Vorhersagen der Standardeinstellungen des TALYS-Codes [46] konnte dieser Faktor bestätigt werden.

Photonen-induzierte Reaktionen können aber noch wesentlich strengere Test, insbesondere für die Gamma-Stärkefunktionen und die Kernniveaudichten bieten, indem man die partiellen Wirkungsquerschnitte untersucht. In diesem Fall unterscheidet man, ob die (γ, n) -Reaktion den Produktkern im Grundzustand oder in einem angeregten Zustand hinterlässt. Dazu ist es notwendig, ein schmalbandiges Photonenspektrum zu verwenden, wie es mit den weltweit höchsten Intensitäten derzeit an der High Intensity γ -ray Source (HI γ S) [151] des Triangle Universities Nuclear Laboratory, U.S.A., zur Verfügung steht. Unter Verwendung des γ^3 -Aufbaus [72], eines Detektorarrays aus hochauflösenden Germanium-Halbleiterzählern und hocheffizienten LaBr-Szintillationsdetektoren, in Kombination mit Neutronenzählern aus Flüssigszintillator können sogenannte Neutronen-Gamma-Koinzidenzen detektiert werden. Damit werden in naher Zukunft die partiellen Wirkungsquerschnitte der Reaktion $^{87}\text{Rb}(\gamma, n)$ untersucht [154] und liefern so die gewünschten Informationen.

Obschon die astrophysikalischen Netzwerkrechnungen einige Tausend Isotope und die zugehörigen Zehntausenden Reaktionen umfassen, gibt es doch einige besondere Reaktionen die einen über den Durchschnitt hinausgehenden Einfluss auf die Produktion der p -Kerne haben. Im Fall des γ -Prozesses wurden solche Schlüsselreaktionen mit Hilfe unterschiedlicher Ansätze bestimmt: einerseits wurden diejenigen Reaktionen herausgegriffen, die bei der Variation der Raten eines bestimmten Reaktionstyps einen besonders großen Einfluss zeigten [23], andererseits wurden die Reaktionen ermittelt, die einen besonderen Einfluss auf die Position der oben erwähnten Verzweigungen hatten [22]. Interessanterweise gibt es nur vier Reaktionen, die in beiden Studien vorkommen: $^{92}\text{Mo}(\alpha, \gamma)^{96}\text{Ru}$, $^{102}\text{Pd}(\alpha, \gamma)^{106}\text{Cd}$, $^{116}\text{Sn}(\alpha, \gamma)^{120}\text{Te}$ und $^{124}\text{Xe}(\alpha, \gamma)^{128}\text{Ba}$ (vergleiche die Übersicht in Tab. 6.1). In allen vier Fällen ist es die photonen-induzierte Umkehrreaktion, die in der Netzwerkrechnung besonders hervortritt. Die Auflistung anhand der Teilcheneinfangreaktionen ist damit begründet, dass diese bei einer experimentellen Untersuchung bevorzugt sein soll.

Aber es gibt auch Fälle wie die Produktion des häufigsten p -Kerns ^{92}Mo in denen auch die Teilcheneinfangreaktionen selbst eine signifikante Rolle im Nukleosyntheseprozess spielen können (vergleiche dazu [19, 20]). Deshalb werden in dieser Arbeit auch die Untersuchungen der Reaktionen $^{90}\text{Zr}(p, \gamma)$ und $^{91}\text{Nb}(p, \gamma)$ beschrieben. Für die erstgenannte Reaktion liegen bereits experimentelle Daten vor. Die Reaktion wurde mittels der Methode der „Thick-target yield“ (dt. Dickes-Target-Ausbeute) [126], mittels γ -Spektroskopie [127] und mittels γ -Kalorimetrie [125] im Strahl untersucht. Während die Ergebnisse von [126] und [125] im Rahmen der Unsicherheiten gut übereinstimmen, weichen die Resultate von [127] signifikant nach unten ab. Daher wurde die Reaktion nochmals mittels γ -Spektroskopie im Strahl am Aufbau HORUS [98] der Universität zu Köln untersucht bei verschiedenen Energien am oberen Ende des astrophysikalisch

relevanten Energiebereichs untersucht [100]. Es konnte eine gute Übereinstimmung mit den Resultaten von [127] gefunden werden. Dieser Fall zeigt, dass es nicht ausreicht, die statistischen Unsicherheiten bei den verschiedenen experimentellen Ansätzen zu reduzieren, sondern dass es insbesondere notwendig ist, systematische Fehlerquellen zu identifizieren und bestmöglich zu korrigieren. Andernfalls ist es nicht möglich, unter Einbeziehung aller vorhandenen experimentellen Resultate die Anwendbarkeit verschiedener kernphysikalischer Eingangsgrößen des Hauser-Feshbach-Formalismus – in diesem Fall die Gamma-Stärkefunktionen und die Protonen-Kern-Potentiale – einzuschränken.

Vollkommen andere Herausforderungen stellen sich, wenn der Targetkern einer zu untersuchenden Reaktion instabil ist. Bei einer geeignet langen Halbwertszeit und ausreichend großen Produktionswirkungsquerschnitten ist es in Einzelfällen möglich, ein Target zu erzeugen und in direkter Kinematik zu untersuchen. Im Fall der Reaktion $^{91}\text{Nb}(p,\gamma)$ soll die Produktion durch Bestrahlung eines angereicherten ^{92}Mo -Targets mit Protonen im Energiebereich von 15 MeV bis 20 MeV statt finden. Um die nur theoretisch vorhergesagten Wirkungsquerschnitte experimentell zu untersuchen und eventuell störende Reaktionen zu finden, wurden dünne Molybdänfolien natürlicher Isotopenzusammensetzung an der Physikalisch Technischen Bundesanstalt, Braunschweig, mit Protonen im entsprechenden Energiebereich bestrahlt [132]. Da die Halbwertszeit von ^{91}Nb mit $t_{1/2} = 680$ Jahren sehr groß ist, dauert die Spektroskopie der aktivierten Targets noch an. Erste vorläufige Auswertungen deuten jedoch daraufhin, dass der gewählte Produktionsmechanismus erfolgreich angewandt werden kann.

Da die Menge des verfügbaren Materials bei einem solchen radioaktiven Target beschränkt bleibt, ist es notwendig mit möglichst hohen Projekttilströmen zu arbeiten, um ein detektierbares Signal zu erhalten. An der Frankfurter Neutronenquelle am Stern-Gerlach-Zentrum (FRANZ) der Goethe Universität Frankfurt wird ein Protonenbeschleuniger realisiert, der Ströme von 2 mA in einem Energiebereich von 1.8 MeV bis 2.2 MeV zur Verfügung stellt. Damit eine solcher Strahlstrom gezielt auf das Target transportiert werden kann, ist es notwendig, die in dieser Arbeit vorgestellte Strahlführung [133] zu realisieren. Außerdem wurden Kühlmechanismen entwickelt, die die im Target deponierte Leistung effizient abführen und somit eine Beschädigung während des Experiments verhindern [135]. Auch das Design einer Targetkammer für das zu verwendende 4π -BaF₂-Kalorimeter [94] ist bereits vorhanden. Sobald an FRANZ ein entsprechender Protonenstrahl zur Verfügung steht, wird die Anwendbarkeit der gemachten Entwicklungen in Testexperimenten untersucht.

Da der Energiebereich an FRANZ begrenzt ist, müssen weitere experimentelle Untersuchungen gemacht werden, um den kompletten für die Nukleosynthese von ^{92}Mo relevanten Energiebereich der Reaktion $^{91}\text{Nb}(p,\gamma)$ abzudecken. Für Energien kleiner als die von FRANZ zur Verfügung gestellten 1.8 MeV kommt der „mass recoil separator“ (dt. Massentrückstoß-Separator) DRAGON [107] in Frage. Hier wird das Experiment in inverser Kinematik durchgeführt und die erzeugten Produktkerne nachgewiesen. Obwohl

DRAGON für die Untersuchung von Reaktionen an leichten Kernen, insbesondere der Reaktion $^{15}\text{O}(\alpha,\gamma)$, entwickelt wurde, konnte kürzlich gezeigt werden, dass die Anlage auch mit Kernen höherer Massenzahl arbeiten kann. Die Reaktion $^{74}\text{Se}(\alpha,\gamma)$, die zu den Schlüsselreaktionen für den γ -Prozess gezählt wird (vergleiche Tab. 6.1) wurde bereits bei zwei Energien untersucht [108]. Eine Fortsetzung ist im Dezember 2014 geplant. Für Energien oberhalb der von FRANZ zur Verfügung gestellten 2.2 MeV kann die inverse Kinematik an einem Speicherring realisiert werden. Der ESR des GSI Helmholtzzentrums für Schwerionenforschung (GSI), Darmstadt, arbeitet bei höheren Energien bis minimal etwa 5 MeV/u. Die Lücke wird durch den derzeit im Aufbau befindlichen CRYRING geschlossen, der in Bereiche von etwa 3 MeV/u vorstoßen soll [109].

Die an der GSI, Darmstadt, zur Verfügung stehenden radioaktiven Strahlen konnten auch verwendet werden, um die Wirkungsquerschnitte von (γ,n) -Reaktionen am ALADiN-LAND Aufbau zu untersuchen. Dabei kommt die Methode des Coulomb-Aufbruchs in inverser Kinematik zum Einsatz [168, 160]. Das benötigte Photonentarget wird durch ein Target realisiert, dessen Material eine hohe Ladungszahl aufweist. Die auf Energien von einigen 100 MeV/u beschleunigten Kerne werden dann durch das Lorentz-kontrahierte elektromagnetische Feld der Targetkerne durch den Austausch virtueller Photonen so hoch angeregt, dass ein Neutron emittiert werden kann. Die Analyse der Daten ist komplex und zeitaufwändig, da die Messung in vollständiger Kinematik erfolgen muss, d.h. die Impulse aller Reaktionsprodukte müssen bestimmt werden, um die Anregungsenergie aus der sogenannten invarianten Masse zu bestimmen. Daher ist die Analyse aller in der Experimentkampagne S289 gewonnenen Daten noch nicht vollständig abgeschlossen [169].

Der im Aufbau befindliche Nachfolger für FAIR, der R³B-Aufbau, bietet die Möglichkeit neben (γ,n) -Reaktionen gleichzeitig (γ,α) -Reaktionen zu untersuchen. Die bisherige Anordnung des R³B-Aufbaus erlaubt es, auch die Detektion von α -Teilchen in Betracht zu ziehen. Die Realisation ist allerdings anspruchsvoll, da sich die Flugbahnen der α -Teilchen nach der Passage des separierenden Dipolmagneten wesentlich weniger von denen der schweren Fragmente unterscheiden als die der Protonen. Der Aufwand in Detektorentwicklung und Optimierung der Datenaufnahme würde allerdings dadurch belohnt, dass eine weltweit einzigartige Anlage vorläge, die die Messung von Verhältnissen der Wirkungsquerschnitte von (γ,n) -, (γ,p) - und (γ,α) -Reaktionen ermöglichte. Damit könnten die Verzweigungen des γ -Prozesses erstmals auch für radioaktive Kerne untersucht werden und damit einen entscheidenden Schritt zum vollständigen Verständnis der Nukleosynthese der p -Kerne beitragen.

Bibliography

- [1] E. Burbidge, G. Burbidge, W. Fowler, F. Hoyle, *Rev. Mod. Phys.* **29** (1957) 547.
- [2] A. Cameron, *Stellar Evolution, Nuclear Astrophysics, and Nucleogenesis*, Chalk River Report CRL-41, technical report, A.E.C.L. Chalk River, Canada, 1957.
- [3] A. Coc, *J. Phys. Conf. Ser.* **420** (2013) 012136.
- [4] F.-K. Thielemann, F. Brachwitz, C. Freiburghaus, E. Kolbe, G. Martínez-Pinedo, T. Rauscher, F. Rembgas, W. R. Hix, M. Liebendörfer, A. Mezzacappa, K.-L. Kratz, B. Pfeiffer, K. Langanke, K. Nomoto, S. Rosswog, H. Schatz, M. Wiescher, *Prog. Part. Nucl. Phys.* **46** (2001) 5.
- [5] H.-T. Janka, *Annu. Rev. Nucl. Part. Sci.* **62** (2012) 407.
- [6] M. Arnould, S. Goriely, K. Takahashi, *Phys. Rep.* **450** (2007) 97.
- [7] F. Käppeler, R. Gallino, S. Bisterzo, W. Aoki, *Rev. Mod. Phys.* **83** (2011) 157.
- [8] M. Pignatari, R. Gallino, M. Heil, M. Wiescher, F. Käppeler, F. Herwig, S. Bisterzo, *Astrophys. J.* **710** (2010) 1557.
- [9] M. Lugaro, F. Herwig, J. C. Lattanzio, R. Gallino, O. Straniero, *Astrophys. J.* **586** (2003) 1305.
- [10] K. Lodders, *Astrophys. J.* (2003) 1220.
- [11] W. Hillebrandt, M. Kromer, F. Röpke, A. Ruiter, *Front. Phys.* **8** (2013) 116.
- [12] D. L. Lambert, *Astron. Astroph. Rev.* **3** (1992) 201.
- [13] E. Anders, N. Grevesse, *Geochim. Cosmochim. Acta* **53** (1989) 197.
- [14] C. Arlandini, F. Käppeler, K. Wisshak, R. Gallino, M. Lugaro, M. Busso, O. Straniero, *Astrophys. J.* **525** (1999) 886.
- [15] J. Glorius, *Experimental studies of optical potentials for p-process nucleosynthesis*, PhD Thesis, Goethe Universität Frankfurt a.M., 2013.
- [16] P. De Bièvre, P. D. P. Taylor, *Int. J. Mass Spectrom. Ion Proc.* **123** (1993) 149.
- [17] M. Arnould, S. Goriely, *Phys. Rep.* **384** (2003) 1.
- [18] J. Audouze, J. W. Truran, *Astrophys. J.* **202** (1975) 204.
- [19] M. Kusakabe, N. Iwamoto, K. Nomoto, *Astrophys. J.* **726** (2011) 25.
- [20] C. Travaglio, F. Röpke, R. Gallino, W. Hillebrandt, *Astrophys. J.* **739** (2011) 93.

- [21] S. E. Woosley, W. M. Howard, *Astrophys. J. Suppl. Ser.* **36** (1978) 285.
- [22] T. Rauscher, *Phys. Rev. C* **73** (2006) 015804.
- [23] W. Rapp, J. Görres, M. Wiescher, H. Schatz, F. Käppeler, *Astrophys. J.* **653** (2006) 474.
- [24] R. Wallace, S. Woosley, *Astrophys. J. Suppl. Ser.* **45** (1981) 389.
- [25] H. Schatz, K. Rehm, *Nucl. Phys.* **A777** (2006) 601.
- [26] H. Schatz, A. Aprahamian, V. Barnard, L. Bildsten, A. Cumming, M. Ouellette, T. Rauscher, F.-K. Thielemann, M. Wiescher, *Phys. Rev. Lett.* **86** (2001) 3471.
- [27] C. Fröhlich, G. Martínez-Pinedo, M. Liebendörfer, F.-K. Thielemann, E. Bravo, W. R. Hix, K. Langanke, N. T. Zinner, *Phys. Rev. Lett.* **96** (2006) 142502.
- [28] A. Arcones, C. Fröhlich, G. Martínez-Pinedo, *Astrophys. J.* **750** (2012) 18.
- [29] K. Farouqi, K.-L. Kratz, L. I. Mashonkina, B. Pfeiffer, J. J. Cowan, F.-K. Thielemann, J. W. Truran, *Astrophys. J.* **694** (2009)(1) L49.
- [30] S. Goriely, J. José, M. Hernanz, M. Rayet, M. Arnould, *Astron. Astroph.* **383** (2002) L27.
- [31] S. E. Woosley, D. H. Hartmann, R. D. Hoffman, W. C. Haxton, *Astrophys. J.* **356** (1990) 272.
- [32] K. Langanke, G. Martínez-Pinedo, *Rev. Mod. Phys.* **75** (2003) 819.
- [33] V. Costa, M. Rayet, R. A. Zappalà, M. Arnould, *Astron. Astroph.* **358** (2000) 67.
- [34] M. Jaeger, R. Kunz, A. Mayer, J. Hammer, G. Staudt, K.-L. Kratz, B. Pfeiffer, *Phys. Rev. Lett.* **87** (2001) 202501.
- [35] M. Rayet, M. Arnould, M. Hashimoto, N. Prantzos, K. Nomoto, *Astron. Astroph.* **298** (1995) 517.
- [36] W. M. Howard, B. S. Meyer, S. E. Woosley, *Astrophys. J.* **373** (1991) 5.
- [37] M. Kusakabe, N. Iwamoto, K. Nomoto, *Nucl. Phys.* **A758** (2005) 459 .
- [38] K. Iwamoto, F. Brachwitz, K. Nomoto, N. Kishimoto, H. Umeda, W. R. Hix, F.-K. Thielemann, *Astrophys. J. Suppl. Ser.* **125** (1999) 439.
- [39] M. Rayet, M. El Eid, M. Arnould, in F. Käppeler *et al.*, Ed., *Proceedings of the 2. International Symposium on Nuclear Astrophysics held at Karlsruhe, July 6-10, 1992*, Bristol: Institut of Physics Publ., 1993, (p. 613).

-
- [40] C. Mahaux, H. A. Weidenmüller, *Annu. Rev. Nucl. Part. Sci.* **29** (1979) 1.
- [41] W. Hauser, H. Feshbach, *Phys. Rev.* **87** (1952) 366.
- [42] T. Rauscher, F.-K. Thielemann, *At. Data Nucl. Data Tables* **75** (2000) 1.
- [43] N. Bohr, *Nature* **137** (1936) 137.
- [44] T. Rauscher, *Int. J. Mod. Phys. E* **20** 1071.
- [45] A. Sauerwein, *Experimental studies of charged-particle induced reactions and their impact on the nucleosynthesis of p nuclei*, PhD Thesis, Universität zu Köln, 2012.
- [46] A. J. Koning, S. Hilaire, M. C. Duijvestijn, *AIP Conf. Proc.* **769** (2005) 1154.
- [47] J.-P. Jeukenne, A. Lejeune, C. Mahaux, *Phys. Rev. C* **16** (1977) 80.
- [48] A. Lejeune, *Phys. Rev. C* **21** (1980) 1107.
- [49] A. Koning, J. Delaroche, *Nucl. Phys.* **A713** (2003) 231.
- [50] L. McFadden, G. R. Satchler, *Nucl. Phys.* **84** (1966) 177.
- [51] S. Watanabe, *Nucl. Phys.* **8** (1958) 484.
- [52] D. Brink, *Nucl. Phys.* **4** (1957) 215.
- [53] P. Axel, *Phys. Rev.* **126** (1962) 671.
- [54] T. Rauscher, F.-K. Thielemann, K.-L. Kratz, *Phys. Rev. C* **56** (1997) 1613.
- [55] A. V. Ignatyuk, K. K. Istekov, G. N. Smirenkin, *Sov. J. Nucl. Phys.* **29** (1979) 450.
- [56] A. V. Ignatyuk, J. L. Weil, S. Raman, S. Kahane, *Phys. Rev. C* **47** (1993) 1504.
- [57] D. Mocalj, T. Rauscher, K. Langanke, G. Martínez-Pinedo, L. Pacearescu, A. Fäbller, F.-K. Thielemann, *Nucl. Phys.* **A758** (2005) 154.
- [58] P. Möller, J. R. Nix, W. D. Myers, W. J. Swiatecki, *At. Data Nucl. Data Tables* **59** (1995) 185.
- [59] J. Pearson, R. Nayak, S. Goriely, *Phys. Lett. B* **387** (1996) 455.
- [60] S. Goriely, M. Samyn, J. Pearson, *Nucl. Phys.* **A773** (2006) 279.
- [61] G. Audi, A. Wapstra, C. Thibault, *Nucl. Phys.* **A729** (2003) 337.

- [62] M. Avrigeanu, W. von Oertzen, A. J. M. Plompen, V. Avrigeanu, Nucl. Phys. **A723** (2003) 104.
- [63] A. Ornelas, D. Galaviz, Zs. Fülöp, Gy. Gyürky, G. G. Kiss, Z. Máté, P. Mohr, T. Rauscher, E. Somorjai, **K. Sonnabend**, A. Zilges, J. Phys. Conf. Ser. **337** (2012) 012030.
- [64] P. Demetriou, C. Grama, S. Goriely, Nucl. Phys. **A707** (2002) 253.
- [65] H. Utsunomiya, S. Goriely, T. Kondo, T. Kaihori, A. Makinaga, S. Goko, H. Akimune, T. Yamagata, H. Toyokawa, T. Matsumoto, H. Harano, S. Hohara, Y.-W. Lui, S. Hilaire, S. Péru, A. J. Koning, Phys. Rev. Lett. **100** (2008) 162502.
- [66] H. Utsunomiya, S. Goriely, H. Akimune, H. Harada, F. Kitatani, S. Goko, H. Toyokawa, K. Yamada, T. Kondo, O. Itoh, M. Kamata, T. Yamagata, Y.-W. Lui, S. Hilaire, A. J. Koning, Phys. Rev. C **81** (2010) 035801.
- [67] M. Krτίčka, F. Bečvář, J. Phys. G **35** (2008) 014025.
- [68] S. Goriely, E. Khan, Nucl. Phys. **A706** (2002) 217.
- [69] S. Goriely, E. Khan, M. Samyn, Nucl. Phys. **A739** (2004) 331.
- [70] J. Isaak, D. Savran, M. Krτίčka, M. W. Ahmed, J. Beller, E. Fiori, J. Glorius, J. H. Kelley, B. Löher, N. Pietralla, C. Romig, G. Rusev, M. Scheck, L. Schnorrenberger, J. Silva, **K. Sonnabend**, A. P. Tonchev, W. Tornow, H. R. Weller, M. Zweidinger, Phys. Lett. B **727** (2013) 361.
- [71] D. Savran, T. Aumann, A. Zilges, Prog. Part. Nucl. Phys. **70** (2013) 210.
- [72] B. Löher, V. Derya, T. Aumann, J. Beller, N. Cooper, M. Duchene, J. Endres, E. Fiori, J. Isaak, J. Kelley, M. Knörzner, N. Pietralla, C. Romig, D. Savran, M. Scheck, H. Scheit, J. Silva, A. P. Tonchev, W. Tornow, H. Weller, V. Werner, A. Zilges, Nucl. Instr. and Meth. Phys. Res. A **723** (2013) 136.
- [73] A. Gilbert, A. G. W. Cameron, Can. J. Phys. **43** (1965) 1446.
- [74] P. Demetriou, S. Goriely, Nucl. Phys. **A695** (2001) 95.
- [75] K. Langanke, Nucl. Phys. **A778** (2006) 233.
- [76] A. Wapstra, G. Audi, C. Thibault, Nucl. Phys. **A729** (2003) 129.
- [77] K. Vogt, T. Hartmann, A. Zilges, Phys. Lett. B **517** (2001) 255.
- [78] J. Dufflo, A. Zuker, Phys. Rev. C **52** (1995) R23.

-
- [79] Y. Aboussir, J. Pearson, A. Dutta, F. Tondeur, *At. Data Nucl. Data Tables* **61** (1995) 127.
- [80] J. Glorius, **K. Sonnabend**, J. Görres, D. Robertson, M. Knörzer, A. Kontos, T. Rauscher, R. Reifarth, A. Sauerwein, E. Stech, W. Tan, T. Thomas, M. Wiescher, *Phys. Rev. C* **89** (2014) 065808.
- [81] Gy. Gyürky, M. Vakulenko, Zs. Fülöp, Z. Halász, G. G. Kiss, E. Somorjai, T. Szücs, *Nucl. Phys.* **A922** (2014) 112.
- [82] L. Netterdon, P. Demetriou, J. Endres, U. Giesen, G. Kiss, A. Sauerwein, T. Szücs, K. Zell, A. Zilges, *Nucl. Phys.* **A916** (2013) 149.
- [83] A. Palumbo, W. P. Tan, J. Görres, M. Wiescher, N. Özkan, R. T. Güray, C. Yalcin, *Phys. Rev. C* **85** (2012) 028801.
- [84] I. Dillmann, L. Coquard, C. Domingo-Pardo, F. Käppeler, J. Marganec, E. Uberseder, U. Giesen, A. Heiske, G. Feinberg, D. Hentschel, S. Hilpp, H. Leiste, T. Rauscher, F.-K. Thielemann, *Phys. Rev. C* **84** (2011) 015802.
- [85] J. Marganec, I. Dillmann, C. Domingo Pardo, F. Käppeler, S. Walter, *Phys. Rev. C* **82** (2010) 035806.
- [86] R. T. Güray, N. Özkan, C. Yalçın, A. Palumbo, R. deBoer, J. Görres, P. J. Leblanc, S. O'Brien, E. Strandberg, W. P. Tan, M. Wiescher, Zs. Fülöp, E. Somorjai, H. Y. Lee, J. P. Greene, *Phys. Rev. C* **80** (2009) 035804.
- [87] J. Hasper, D. Galaviz, S. Müller, A. Sauerwein, D. Savran, L. Schnorrenberger, **K. Sonnabend**, A. Zilges, *Phys. Rev. C* **79** (2009) 055807.
- [88] J. Hasper, S. Müller, D. Savran, L. Schnorrenberger, **K. Sonnabend**, A. Zilges, *Phys. Rev. C* **77** (2008) 015803.
- [89] G. G. Kiss, T. Szücs, Zs. Török, Z. Korkulu, Gy. Gyürky, Z. Halász, Zs. Fülöp, E. Somorjai, T. Rauscher, *Phys. Rev. C* **86** (2012) 035801.
- [90] A. Wallner, M. Bichler, I. Dillmann, R. Golser, F. Käppeler, W. Kutschera, M. Paul, A. Priller, P. Steier, C. Vockenhuber, *Nucl. Instr. and Meth. Phys. Res. B* **259** (2007) 677 .
- [91] S. Agostinelli, J. Allison, K. Amako, J. Apostolakis, H. Araujo, P. Arce, M. Asai, D. Axen, S. Banerjee, G. Barrand, F. Behner, L. Bellagamba, J. Boudreau, *et al.*, *Nucl. Instr. and Meth. Phys. Res. A* **506** (2003) 250.
- [92] A. Spyrou, H.-W. Becker, A. Lagoyannis, S. Harissopulos, C. Rolfs, *Phys. Rev. C* **76** (2007) 015802.

- [93] A. Simon, S. Quinn, A. Spyrou, A. Battaglia, I. Beskin, A. Best, B. Bucher, M. Couder, P. DeYoung, X. Fang, J. Görres, A. Kontos, Q. Li, S. Liddick, A. Long, S. Lyons, K. Padmanabhan, J. Peace, A. Roberts, D. Robertson, K. Smith, M. Smith, E. Stech, B. Stefanek, W. Tan, X. Tang, M. Wiescher, Nucl. Instr. and Meth. Phys. Res. A **703** (2013) 16.
- [94] K. Wisshak, K. Guber, F. Käppeler, J. Krisch, H. Müller, G. Rupp, F. Voss, Nucl. Instr. Meth. A **292** (1990) 595.
- [95] R. Reifarth, T. A. Bredeweg, A. Alpizar-Vicente, J. C. Browne, E.-I. Esch, U. Greife, R. C. Haight, R. Hatarik, A. Kronenberg, J. M. O'Donnell, R. S. Rundberg, J. L. Ullmann, D. J. Vieira, J. B. Wilhelmy, J. M. Wouters, Nucl. Instr. Meth. A **531** (2004) 528.
- [96] C. Hutter, M. Babilon, W. Bayer, D. Galaviz, T. Hartmann, P. Mohr, S. Müller, W. Rochow, D. Savran, **K. Sonnabend**, K. Vogt, S. Volz, A. Zilges, Nucl. Instr. and Meth. Phys. Res. A **489** (2002) 247.
- [97] S. V. Harissopulos, AIP Conf. Proc. **704** (2004) 422.
- [98] L. Netterdon, V. Derya, J. Endres, C. Fransen, A. Hennig, J. Mayer, C. Müller-Gatermann, A. Sauerwein, P. Scholz, M. Spieker, A. Zilges, Nucl. Instr. and Meth. Phys. Res. A **754** (2014) 94 .
- [99] A. Sauerwein, J. Endres, L. Netterdon, A. Zilges, V. Foteinou, G. Provas, T. Konstantinopoulos, M. Axiotis, S. F. Ashley, S. Harissopulos, T. Rauscher, Phys. Rev. C **86** (2012) 035802.
- [100] P. Erbacher, *Untersuchung der Reaktion $^{90}\text{Zr}(p,\gamma)$ mit In-Beam-Gammaspektroskopie*, Master Thesis, Goethe Universität Frankfurt a.M., unpublished, 2014.
- [101] D. Savran, K. Lindenberg, J. Glorius, B. Löher, S. Müller, N. Pietralla, L. Schnorrenberger, V. Simon, **K. Sonnabend**, C. Wälzlein, M. Elvers, J. Endres, J. Hasper, A. Zilges, Nucl. Instr. and Meth. Phys. Res. A **613** (2010) 232.
- [102] L. Schnorrenberger, D. Savran, J. Glorius, K. Lindenberg, B. Löher, N. Pietralla, **K. Sonnabend**, Nucl. Instr. and Meth. Phys. Res. A **735** (2014) 19 .
- [103] R. Reifarth, C. Lederer, F. Käppeler, J. Phys. G **41** (2014) 053101.
- [104] S. Quinn, A. Spyrou, A. Simon, A. Battaglia, M. Bowers, B. Bucher, C. Casarella, M. Couder, P. DeYoung, A. Dombos, J. Greene, J. G Nucl. Instr. and Meth. Phys. Res. A **757** (2014)(0) 62 .
- [105] C. Ruiz, U. Greife, U. Hager, Eur. Phys. J. A **50** (2014) 99.

-
- [106] D. Schürmann, A. Di Leva, L. Gialanella, D. Rogalla, F. Strieder, N. De Cesare, A. D’Onofrio, G. Imbriani, R. Kunz, C. Lubritto, A. Ordine, V. Roca, C. Rolfs, M. Romano, F. Schümann, F. Terrasi, H.-P. Trautvetter, *Eur. Phys. J. A* **26** (2005) 301.
- [107] D. Hutcheon, S. Bishop, L. Buchmann, M. Chatterjee, A. Chen, J. D’Auria, S. Engel, D. Gigliotti, U. Greife, D. Hunter, A. Hussein, C. Jewett, N. Khan, M. Lamey, A. Laird, W. Liu, A. Olin, D. Ottewell, J. Rogers, G. Roy, H. Sprenger, C. Wrede, *Nucl. Instr. and Meth. Phys. Res. A* **498** (2003) 190.
- [108] J. Fallis, *et al.*, Proceedings of Science, PoS(NIC-XIII), to be published, 2014.
- [109] J. Glorius, *et al.*, Proceedings of Science, PoS(NIC-XIII), to be published, 2014.
- [110] T. Aumann, *Eur. Phys. J. A* **26** (2005) 441.
- [111] C. Langer, O. Lepyoshkina, Y. Aksyutina, T. Aumann, S. Beceiro Novo, J. Benlliure, K. Boretzky, M. Chartier, D. Cortina, U. Datta Pramanik, O. Ershova, H. Geissel, R. Gernhäuser, M. Heil, G. Ickert, H. T. Johansson, B. Jonson, A. Kelić-Heil, A. Klimkiewicz, J. V. Kratz, R. Krücken, R. Kulesa, K. Larsson, T. Le Bleis, R. Lemmon, K. Mahata, J. Marganec, T. Nilsson, V. Panin, R. Plag, W. Prokopowicz, R. Reifarth, V. Ricciardi, D. M. Rossi, S. Schwertel, H. Simon, K. Sümmerer, B. Streicher, J. Taylor, J. R. Vignote, F. Wamers, C. Wimmer, P. Z. Wu, *Phys. Rev. C* **89** (2014) 035806.
- [112] C. Langer, A. Algora, A. Couture, M. Csatlós, J. Gulyás, M. Heil, A. Krasznahorkay, J. O’Donnell, R. Plag, R. Reifarth, L. Stuhl, **K. Sonnabend**, T. Tornyi, F. Tovesson, *Nucl. Instr. and Meth. Phys. Res. A* **659** (2011) 411.
- [113] M. Pohl, *The $^{152}\text{Sm}(p,n)$ reaction and its astrophysical importance*, PhD Thesis, Goethe Universität Frankfurt a.M., 2014.
- [114] T. Rauscher, *Astrophys. J. Suppl. Ser.* **201** (2012) 26.
- [115] E. Somorjai, Zs. Fülöp, A. Z. Kiss, C. E. Rolfs, H. P. Trautvetter, U. Greife, M. Junker, S. Goriely, M. Arnould, M. Rayet, T. Rauscher, H. Oberhummer, *Astron. Astroph.* **333** (1998) 1112.
- [116] Zs. Fülöp, Gy. Gyürky, Z. Máté, E. Somorjai, L. Zolnai, D. Galaviz, M. Babilon, P. Mohr, A. Zilges, T. Rauscher, H. Oberhummer, G. Staudt, *Phys. Rev. C* **64** (2001) 065805.
- [117] D. Galaviz, Zs. Fülöp, Gy. Gyürky, Z. Máté, P. Mohr, T. Rauscher, E. Somorjai, A. Zilges, *Phys. Rev. C* **71** (2005) 065802.

- [118] G. G. Kiss, P. Mohr, Zs. Fülöp, D. Galaviz, Gy. Gyürky, Z. Elekes, E. Somorjai, A. Kretschmer, **K. Sonnabend**, A. Zilges, M. Avrigeanu, Phys. Rev. C **80** (2009) 045807.
- [119] G. G. Kiss, T. Rauscher, T. Sz Phys. Lett. B **695** (2011) 419 .
- [120] A. Sauerwein, H.-W. Becker, H. Dombrowski, M. Elvers, J. Endres, U. Giesen, J. Hasper, A. Hennig, L. Netterdon, T. Rauscher, D. Rogalla, K. O. Zell, A. Zilges, Phys. Rev. C **84** (2011) 045808.
- [121] C. Birattari, E. Gadioli, E. Gadioli Erba, A. Grassi Strini, G. Strini, G. Tagliaferri, Nucl. Phys. **A201** (1973) 579.
- [122] I. Spahn, S. Takács, Y. Shubin, F. Tárkányi, H. Coenen, S. Qaim, Appl. Rad. Isot. **63** (2005) 235.
- [123] E. Bauge, J. P. Delaroche, M. Girod, Phys. Rev. C **63** (2001) 024607.
- [124] G. G. Kiss, Gy. Gyürky, Z. Elekes, Zs. Fülöp, E. Somorjai, T. Rauscher, M. Wiescher, Phys. Rev. C **76** (2007) 055807.
- [125] A. Spyrou, S. J. Quinn, A. Simon, T. Rauscher, A. Battaglia, A. Best, B. Bucher, M. Couder, P. A. DeYoung, A. C. Dombos, X. Fang, J. Görres, A. Kontos, Q. Li, L. Y. Lin, A. Long, S. Lyons, B. S. Meyer, A. Roberts, D. Robertson, K. Smith, M. K. Smith, E. Stech, B. Stefanek, W. P. Tan, X. D. Tang, M. Wiescher, Phys. Rev. C **88** (2013) 045802.
- [126] N. A. Roughton, M. R. Fritts, R. J. Peterson, C. S. Zaidins, C. J. Hansen, At. Data Nucl. Data Tables **23** (1979) 177.
- [127] C. E. Laird, D. Flynn, R. L. Hershberger, F. Gabbard, Phys. Rev. C **35** (1987) 1265.
- [128] C. M. Baglin, Nuclear Data Sheets **114** (2013) 1293, online version (<http://www.nndc.bnl.gov>, July 23, 2014).
- [129] P. Erbacher, A. Endres, J. Glorius, L. Netterdon, **K. Sonnabend**, B. Thomas, A. Zilges, Eur. Phys. J. Web Conf. (2014), submitted.
- [130] S. Goriely, Phys. Lett. B **436** (1998) 10.
- [131] A. Endres, C. Arda, P. Erbacher, J. Glorius, K. Göbel, O. Hinrichs, E. Mevius, M. Reich, **K. Sonnabend**, B. Thomas, T. Thomas, Eur. Phys. J. Web Conf. (2014), submitted.
- [132] B. Thomas, *et al.*, Proceedings of Science, PoS(NIC-XIII), to be published, 2014.

-
- [133] O. Hinrichs, *Design und Aufbau der Hochenergie-Strahltransportführung an FRANZ*, PhD Thesis, Goethe Universität Frankfurt a.M., in progress.
- [134] D. Uriot, TraceWin, online description (<http://irfu.cea.fr/Sacm/logiciels/index3.php>, July 29, 2014).
- [135] M. Reich, *Auswahl von Backing-Materialien für hochleistungsbeständige Proben an FRANZ*, Bachelor Thesis, Goethe Universität Frankfurt a.M., unpublished, 2013.
- [136] Autodesk® Simulation Computational Fluid Dynamics, online material at <http://www.autodesk.com/products/simulation-cfd/overview>.
- [137] C. Arda, *Entwurf einer Targetkammer zum Einsatz in (p,γ) -Experimenten an FRANZ*, Bachelor Thesis, Goethe Universität Frankfurt a.M., unpublished, 2014.
- [138] M. Reich, *Design und Aufbau einer Targetkammer mit hochleistungsbeständigen Proben an FRANZ*, Master Thesis, Goethe Universität Frankfurt a.M., in progress.
- [139] T. Rauscher, N. Dauphas, I. Dillmann, C. Fröhlich, Zs. Fülöp, Gy. Gyürky, Rep. Prog. Phys. **76** (2013) 066201.
- [140] T. Rauscher, AIP Adv. **4** (2014) 041012.
- [141] B. L. Berman, S. C. Fultz, Rev. Mod. Phys. **47** (1975) 713.
- [142] G. M. Gurevich, L. E. Lazareva, V. M. Mazur, S. Y. Merkulov, G. V. Solodukhov, V. A. Tyutin, Nucl. Phys. **A351** (1981) 257.
- [143] K. Vogt, P. Mohr, M. Babilon, J. Enders, T. Hartmann, C. Hutter, T. Rauscher, S. Volz, A. Zilges, Phys. Rev. C **63** (2001) 055802.
- [144] **K. Sonnabend**, K. Vogt, D. Galaviz, S. Müller, A. Zilges, Phys. Rev. C **70** (2004) 035802.
- [145] **K. Sonnabend**, D. Savran, J. Beller, M. A. Büssing, A. Constantinescu, M. Elvers, J. Endres, M. Fritzsche, J. Glorius, J. Hasper, J. Isaak, B. Löher, S. Müller, N. Pietralla, C. Romig, A. Sauerwein, L. Schnorrenberger, C. Wälzlein, A. Zilges, M. Zweidinger, Nucl. Instr. and Meth. Phys. Res. A **640** (2011) 6.
- [146] **K. Sonnabend**, J. Hasper, S. Müller, N. Pietralla, D. Savran, L. Schnorrenberger, A. Zilges, AIP Conf. Proc. **1090** (2009) 481.
- [147] A. Sauerwein, **K. Sonnabend**, M. Fritzsche, J. Glorius, E. Kwan, N. Pietralla, C. Romig, G. Rusev, D. Savran, L. Schnorrenberger, A. P. Tonchev, W. Tornow, H. R. Weller, Phys. Rev. C **89** (2014) 035803.
- [148] H. Utsunomiya, P. Mohr, A. Zilges, M. Rayet, Nucl. Phys. **A777** (2006) 459.

- [149] K. Vogt, P. Mohr, M. Babilon, W. Bayer, D. Galaviz, T. Hartmann, C. Hutter, T. Rauscher, **K. Sonnabend**, S. Volz, A. Zilges, Nucl. Phys. **A707** (2002) 241.
- [150] I. Tews, *Entfaltung von (γ,n) -Wirkungsquerschnitten aus Experimenten mit Bremsstrahlungsphotonen*, Bachelor Thesis, Technische Universität Darmstadt, unpublished, 2010.
- [151] H. R. Weller, M. W. Ahmed, H. Gao, W. Tornow, Y. K. Wu, M. Gai, R. Miskimen, Prog. Part. Nucl. Phys. **62** (2009)(1) 257 .
- [152] P. Erbacher, *Photodesintegrationsquerschnitte von Ytterbium-Isotopen*, Bachelor Thesis, Goethe Universität Frankfurt a.M., unpublished, 2012.
- [153] B. Thomas, *Produktion radioaktiver Proben zum Einsatz an FRANZ*, PhD Thesis, Goethe Universität Frankfurt a.M., in progress.
- [154] K. Sonnabend, *et al.*, *Investigation of the s-process branch-point nucleus ^{86}Rb using the γ^3 setup*, accepted proposal by HI γ S PAC, unpublished, 2014.
- [155] S. Müller, *Bestimmung von Photo-Neutron-Wirkungsquerschnitten in Kernen der Seltenen Erden für den astrophysikalischen p-Prozess mit Bremsstrahlung am S-DALINAC*, PhD Thesis, Technische Universität Darmstadt, 2009.
- [156] S. Müller, A. Kretschmer, **K. Sonnabend**, A. Zilges, D. Galaviz, Phys. Rev. C **73** (2006) 025804.
- [157] **K. Sonnabend**, A. Mengoni, P. Mohr, T. Rauscher, K. Vogt, A. Zilges, AIP Conf. Proc. **704** (2004) 463.
- [158] G. Baur, C. A. Bertulani, H. Rebel, Nucl. Phys. **A458** (1986) 188.
- [159] C. Bertulani, G. Baur, Phys. Rep. **163** (1988) 299.
- [160] O. Ershova, *Coulomb Dissociation Reactions on Molybdenum Isotopes for Astrophysics Applications*, PhD Thesis, Goethe Universität Frankfurt a.M., 2009.
- [161] H. Geissel, P. Armbruster, K. Behr, A. Brünle, K. Burkard, M. Chen, H. Folger, B. Franczak, H. Keller, O. Klepper, B. Langenbeck, F. Nickel, E. Pfeng, M. Pfützner, E. Roeckl, K. Rykaczewski, I. Schall, D. Schardt, C. Scheidenberger, K.-H. Schmidt, A. Schröter, T. Schwab, K. Sümmerer, M. Weber, G. Münzenberg, T. Brohm, H.-G. Clerc, M. Fauerbach, J.-J. Gaimard, A. Grewe, E. Hanelt, B. Knödler, M. Steiner, B. Voss, J. Weckenmann, C. Ziegler, A. Magel, H. Wollnik, J. Dufour, Y. Fujita, D. Vieira, B. Sherrill, Nucl. Instr. and Meth. Phys. Res. B **70** (1992) 286.

-
- [162] G. Stengel, *Entwicklung großflächiger Szintillatorfaserdetektoren und aktiver Blendensysteme*, Diploma Thesis, Goethe Universität Frankfurt, unpublished, 1996.
- [163] I. Kraus, *Entwicklung eines CsI-Gammadetektors für Experimente mit radioaktiven Strahlen*, Diploma Thesis, Goethe Universität Frankfurt, unpublished, 1999.
- [164] T. Lange, *Erprobung und Eichung eines CsI(Na) Gamma-Detektor-Systems für Experimente mit radioaktiven Strahlen*, Diploma Thesis, Goethe Universität Frankfurt a.M., unpublished, 2001.
- [165] The ALADIN Collaboration, *The forward spectrometer ALADIN at the 4π detector*, GSI Nachrichten 02-89, 1989.
- [166] J. Cub, G. Stengel, A. Grünschloß, K. Boretzky, T. Aumann, W. Dostal, B. Eberlein, T. Elze, H. Emling, J. Holeczek, R. Holzmann, G. Ickert, J. Kratz, R. Kulesa, Y. Leifels, H. Simon, K. Stelzer, J. Stroth, A. Surowiec, E. Wajda, Nucl. Instr. and Meth. Phys. Res. A **402** (1998) 67.
- [167] T. Blaich, T. Elze, H. Emling, H. Freiesleben, K. Grimm, W. Henning, R. Holzmann, G. Ickert, J. Keller, H. Klingler, W. Kneissl, R. Knig, R. Kulesa, J. Kratz, D. Lambrecht, J. Lange, Y. Leifels, E. Lubkiewicz, M. Proft, W. Prokopowicz, C. Schütter, R. Schmidt, H. Spies, K. Stelzer, J. Stroth, W. Walús, E. Wajda, H. Wollersheim, M. Zinser, E. Zude, Nucl. Instr. and Meth. Phys. Res. A **314** (1992) 136.
- [168] **K. Sonnabend**, M. Babilon, J. Hasper, S. Müller, M. Zarza, A. Zilges, Eur. Phys. J. A **27** (2006) 149.
- [169] K. Göbel, *Measurement of the $^{94}\text{Mo}(\gamma, n)$ reaction by Coulomb dissociation and related post-processing nucleosynthesis simulations for the p -process*, PhD Thesis, Goethe Universität Frankfurt a.M., in progress.
- [170] D. Rossi, *Investigation of the Dipole Response of Nickel Isotopes in the Presence of a High-Frequency Electromagnetic Field*, PhD Thesis, Johannes Gutenberg-Universität Mainz, 2010.
- [171] H. Beil, R. Bergère, P. Carlos, A. Leprêtre, A. D. Miniac, A. Veysseyre, Nucl. Phys. **A227** (1974) 427.
- [172] A. Moalem, Y. Gaillard, A. M. Bemolle, M. Buenerd, J. Chauvin, G. Duhamel, D. Lebrun, P. Martin, G. Perrin, P. de Saintignon, Phys. Rev. C **20** (1979) 1593.
- [173] H. Beil, R. Bergère, A. Veysseyre, Nucl. Instr. and Meth. **67** (1969) 293.

- [174] B. L. Berman, R. E. Pywell, S. S. Dietrich, M. N. Thompson, K. G. McNeill, J. W. Jury, *Phys. Rev. C* **36** (1987) 1286.
- [175] M. Erhard, A. R. Junghans, C. Nair, R. Schwengner, R. Beyer, J. Klug, K. Kosev, A. Wagner, E. Grosse, *Phys. Rev. C* **81** (2010) 034319.
- [176] Y. M. Gledenov, P. E. Koehler, J. Andrzejewski, K. H. Guber, T. Rauscher, *Phys. Rev. C* **62** (2000) 042801(R).
- [177] C. H. Johnson, A. Galonsky, J. P. Ulrich, *Phys. Rev.* **109** (1958) 1243.
- [178] S. Harissopulos, S. Galanopoulos, P. Demetriou, A. Spyrou, G. Kriembardis, M. Kokkoris, A. Karydas, C. Zarkadas, R. Kunz, M. Fey, J. Hammer, G. Gyürky, Z. Fülöp, E. Somorjai, A. Dewald, K. Zell, P. von Brentano, R. Julin, S. Goriely, *Nucl. Phys.* **A719** (2003) 115c.
- [179] S. Harissopulos, A. Spyrou, A. Lagoyannis, M. Axiotis, P. Demetriou, J. W. Hammer, R. Kunz, H.-W. Becker, *Phys. Rev. C* **87** (2013) 025806.
- [180] S. J. Quinn, A. Spyrou, A. Simon, A. Battaglia, M. Couder, P. A. DeYoung, A. C. Dombos, X. Fang, J. Görres, A. Kontos, Q. Li, S. Lyons, B. S. Meyer, G. F. Peaslee, D. Robertson, K. Smith, M. K. Smith, E. Stech, W. P. Tan, X. D. Tang, M. Wiescher, *Phys. Rev. C* **88** (2013) 011603.
- [181] P. Tsagari, M. Kokkoris, E. Skreti, A. G. Karydas, S. Harissopulos, T. Paradellis, P. Demetriou, *Phys. Rev. C* **70** (2004) 015802.
- [182] S. Harissopulos, A. Spyrou, A. Lagoyannis, C. Zarkadas, H.-W. Becker, C. Rolfs, F. Strieder, J. Hammer, A. Dewald, K.-O. Zell, P. von Brentano, R. Julin, P. Demetriou, S. Goriely, *Nucl. Phys.* **A758** (2005) 505 .
- [183] S. Harissopulos, E. Skreti, P. Tsagari, G. Souliotis, P. Demetriou, T. Paradellis, J. Hammer, R. Kunz, C. Angulo, S. Goriely, T. Rauscher, *Phys. Rev. C* **64** (2001) 055804.
- [184] G. G. Kiss, T. Rauscher, Gy. Gyürky, A. Simon, Zs. Fülöp, E. Somorjai, *Phys. Rev. Lett.* **101** (2008) 191101.
- [185] Z. Halász, Gy. Gyürky, J. Farkas, Zs. Fülöp, T. Szücs, E. Somorjai, T. Rauscher, *Phys. Rev. C* **85** (2012) 025804.
- [186] Gy. Gyürky, G. G. Kiss, Z. Elekes, Zs. Fülöp, E. Somorjai, A. Palumbo, J. Görres, H. Y. Lee, W. Rapp, M. Wiescher, N. Özkan, R. T. Güray, G. Efe, T. Rauscher, *Phys. Rev. C* **74** (2006) 025805.

- [187] Gy. Gyürky, Z. Elekes, Zs. Fülöp, G. Kiss, E. Somorjai, A. Palumbo, M. Wiescher, *Phys. Rev. C* **71** (2005) 057302.
- [188] The NuGrid collaboration, <http://www.nugridstars.org>.
- [189] F. Herwig, S. Diehl, C. L. Fryer, R. Hirschi, A. Hungerford, G. Magkotsios, M. Pignatari, G. Rockefeller, F. X. Timmes, P. Young, M. E. Bennet, *Proceedings of Science*, 2008, (p. PoS(NIC-X)023).
- [190] M. Pignatari, F. Herwig, *Nucl. Phys. News Int.* **22** (2012) 18.
- [191] T. Rauscher, F.-K. Thielemann, *The Basel reaction library (REACLIB)*, <http://download.nucastro.org/astro/reaclib/>, 2009.
- [192] R. H. Cyburt, A. M. Amthor, R. Ferguson, Z. Meisel, K. Smith, S. Warren, A. Heger, R. D. Hoffman, T. Rauscher, A. Sakharuk, H. Schatz, F. K. Thielemann, M. Wiescher **189** (2010) 240, online version: <https://groups.nsl.msu.edu/jina/reaclib/db/index.php>.
- [193] D. Kasen, F. K. Röpke, S. E. Woosley, *Nature* **460** (2009) 869.
- [194] C. Travaglio, W. Hillebrandt, M. Reinecke, F.-K. Thielemann, *Astron. Astroph.* **425** (2004) 1029.

Veröffentlichungen

Die in dieser Arbeit zusammengetragenen Ergebnisse sind in zahlreichen Publikationen bereits auszugsweise veröffentlicht. Diese sind im Literaturverzeichnis der Arbeit aufgeführt. Zur besseren Auffindbarkeit wurde mein Name im Literaturverzeichnis in Fettdruck hervorgehoben.

Ein vollständiges Literaturverzeichnis ist dem Antrag auf Zulassung zur Habilitation im Rahmen des ausführlichen Lebenslaufes, der auch eine Übersicht der ausgeübten Lehr- und Vortragstätigkeit enthält, beigefügt.

Danksagung

Zahlreiche Menschen haben durch ihre Mitarbeit und Diskussionsbereitschaft im Laufe der vergangenen Jahre dazu beigetragen, dass diese Arbeit möglich geworden ist. Sie alle namentlich aufzuführen, würde den Rahmen dieser Danksagung überschreiten. Daher möchte ich an dieser Stelle einfach allen meinen herzlichen Dank aussprechen, die mich auf diese Weise begleitet haben.

Der Deutschen Forschungsgemeinschaft gilt mein Dank für die finanzielle Förderung von Teilen dieser Arbeit im Rahmen der Projekte SO907/2-1 und SFB634. Auch dem Deutschen Akademischen Auslandsdienst (DAAD) und der Exzellenzinitiative des Landes Hessens LOEWE im Rahmen des Helmholtz International Center for FAIR danke ich für die bereit gestellte Förderung.

Diese Arbeit ist meinen Eltern, Doris und Karlheinz, für ihre geduldige Unterstützung in den vergangenen Jahren gewidmet. Ohne ihre stetige und unkomplizierte Bereitschaft, mir die Vereinbarkeit meiner Familie und meines Berufs zu ermöglichen, wäre all das nicht möglich gewesen. Meiner Familie selbst, Jürgen, Lena und Yasmin, widme ich diese Arbeit für die Liebe, mit der sie mich getragen haben, und für den Sonnenschein, den sie auch an den trübsten Tagen in mein Leben bringen.

Lebenslauf

Persönliche Daten

Name: Kerstin Sonnabend geb. Deneffleh
Geburtsdatum: 02. Mai 1976
Geburtsort: Bensheim
Eltern: Karlheinz Deneffleh
Doris Deneffleh geb. Einberger
Familienstand: verheiratet mit Jürgen Sonnabend
Kinder: Lena und Yasmin Sonnabend
Bekenntnis: römisch-katholisch

Schulbildung

August 1982 – Juli 1986 Wingertsbergschule, Lorsch
August 1986 – Juni 1995 Goethe-Gymnasium, Bensheim
Juni 1995 Allgemeine Hochschulreife, Durchschnittsnote: 1.0

Hochschulbildung

April 1996 Technische Universität (TU) Darmstadt, Studienfächer
Physik & Mathematik für das Lehramt an Gymnasien
Wissenschaftliche Hausarbeit mit dem Thema:
*Entwicklung des Ablaufs und der Anleitung eines Versuchs
zur Positronen-Emissions-Tomographie*
Mai 2000 TU Darmstadt, Studienfach Informatik für das Lehramt
an Gymnasien
Oktober 2000 1. Staatsexamen in Physik & Mathematik für das Lehramt
an Gymnasien, Durchschnittsnote: 1.29 (mit Auszeichnung)
November 2000 Promotion in Physik an der TU Darmstadt, Note: sehr
gut bestanden, Thema der Dissertation:
*Untersuchung von „branching points“ im astrophysikalischen
s-Prozess mit reellen Photonen*
April 2004 1. Staatsexamen in Informatik für das Lehramt an Gym-
nasien, Note: sehr gut
April 2005

Arbeitsverhältnisse

Oktober 1997 – September 2000 Studentische Hilfskraft an der TU Darmstadt
Januar 2001 – Dezember 2010 Wissenschaftlicher Mitarbeiter an der TU Darmstadt
Juli 2009 – Dezember 2009 Visiting Assistant Professor an der University of Notre
Dame, Indiana, U.S.A.
Januar 2011 – November 2012 Wissenschaftlicher Mitarbeiter an der Goethe Universität
Frankfurt a.M. (GUF)
seit Dezember 2012 Leitung der Nachwuchsgruppe PARIS an der GUF,
gefördert durch das Emmy Noether-Programm der DFG

Erklärung

Hiermit erkläre ich gemäß §3, Nr. 2h und 2i der Habilitationsordnung der mathematisch-naturwissenschaftlichen Fachbereiche der Johann Wolfgang Goethe Universität Frankfurt a.M.,

dass die vorliegende Arbeit meinen ersten Versuch einer Habilitation darstellt und

dass sie von mir selbstständig verfasst worden ist. Überall dort, wo ich die Gedanken und Ideen anderer verwendet oder entlehnt, mich auf fremde Kenntnisse in Wort oder Schrift gestützt habe, habe ich dies kenntlich gemacht und die verwendeten Quellen angegeben.

Die Ergebnisse zur Untersuchung Optischer Teilchen-Kern-Potentiale in Abschnitt 5.1.1 beruhen auf der Dissertation von Dr. Jan Glorius, die ich betreut habe. Gleiches gilt für die noch in Arbeit befindlichen Dissertationen von Kathrin Göbel, Ole Hinrichs und Benedikt Thomas, sowie alle zitierten Bachelor- und Masterarbeiten.

Frankfurt, im November 2014

(Kerstin Sonnabend)

